STRUCTURAL AND OPTICAL STUDIES OF SOME RARE EARTH IONS (Eu^{3+}, Tb^{3+}, Sm^{3+}, Pr^{3+}) DOPED NANOPARTICLES FOR DEVICE APPLICATIONS

A THESIS SUBMITTED IN PARTIAL FULFILLMENT OF THE REQUIREMENTS FOR THE DEGREE OF DOCTOR OF PHILOSOPHY

LALRUATPUIA

MZU REGISTRATION NO.: 2080 of 2012

Ph.D. REGISTRATION NO.: MZU/Ph.D./ 1374 of 23.07.2019

DEPARTMENT OF PHYSICS,

SCHOOL OF PHYSICAL SCIENCES

JULY, 2024

STRUCTURAL AND OPTICAL STUDIES OF SOME RARE EARTH IONS (Eu^{3+}, Tb^{3+}, Sm^{3+}, Pr^{3+}) DOPED NANOPARTICLES FOR DEVICE APPLICATIONS

By

LALRUATPUIA

Department of Physics

Supervisor

Prof. S. RAI

Submitted

In partial fulfillment of the requirement of the

Degree of Doctor of Philosophy in Physics of Mizoram University, Aizawl.

MIZORAM UNIVERSITY
SCHOOL OF PHYSICAL SCIENCES
AIZAWL 796 004 MIZORAM
Phone: 8732853277(M)

Prof. Suman Rai E-mail: srai.rai677@gmail.com

Dean, School of Physical Sciences

Certificate

This is to certify that the thesis entitled "Structural and Optical Studies of Some Rare Earth Ions (Eu^{3+}, Tb^{3+}, Sm^{3+}, Pr^{3+}) Doped Nanoparticles for Device Applications" submitted by Mr. Lalruatpuia (Registration No. : MZU/Ph.D./ 1374 of 23.07.2019) for the degree of Doctor of Philosophy (Ph.D.) of the Mizoram University, embodies the record of original investigation carried out by him under my supervision. He has been duly registered and the thesis presented is worthy of being considered for the award of the Ph.D. degree. This work has not been submitted for any degree from any other university.

(Prof S. RAI)
Supervisor

DECLARATION

MIZORAM UNIVERSITY

JULY 2024

I **LALRUATPUIA**, hereby declare that the subject matter of this thesis is the record of work done by me, that the contents of this thesis did not form basis of the award of any previous degree to me or to do the best of my knowledge to anybody else, and that the thesis has not been submitted by me for any research degree in any other University/Institute.

This is being submitted to the Mizoram University for the **Degree of Doctor of Philosophy in Physics**

(LALRUATPUIA)

Candidate

Prof. ZAITHANZAUVA PACHUAU

(Head of Department)

Department of Physics

Mizoram University

Prof S. RAI

(Supervisor)

Department of Physics

Mizoram University

Acknowledgement

It has been a pleasure for me to work as a research scholar in the Department of Physics, Mizoram University over the past few years. First of all, I thank to the Almighty God for his guidance through all the long way, the one who let me finish my degree. I will keep on trusting you for my future.

I would like to give my deepest thanks to my supervisor Prof. S. Rai who made this work possible. His guidance, advice, commitment and support carried me throughout the duration of my research.

I also extend my sincere heartfelt to Dean, School of Physical Sciences and Head, Department of Physics for allowing me to work as a registered scholar in the department. In addition, I would like to express my gratitude to the entire faculty in the Department of Physics for their insightful advice and guidance on my research. I also want to thank the department's non-teaching staff for their unwavering assistance whenever I've needed it. For their unwavering support throughout this journey, I am also grateful to my fellow research scholars from the physics department and other departments, especially thanks to my fellow labmates KMS Dawngliana, Mrigankadeep Bharadwaj and Lalnunpuia Khiangte.

My sincere gratitude also goes to Dr. Andrew Lungtiawia Fanai, Asst. Professor, MMV, Banaras Hindu University and Dr. MD Uzair Khan, the former scholars of Prof. S. Rai for their guidance especially during the early days of my research and Dr. Khamsuanpauva, Senior Medical Physicist, Mizoram State Cancer Institute for providing γ-ray facility. I am very grateful to Department of Chemistry MZU, for recording the data for structural analysis of FTIR. I also thanks to the IIT BHU and CIF, IIT Guwahati for recording data of XRD and TEM analysis.

Special thanks to Ministry of Tribal Affairs, Govt. of India for their financial support through NFST fellowship with Award letter 202021-NFST-MIZ-0247.

In conclusion, thanks are due to my family members. It is their love, encouragement and support that have supported me throughout the achievement of this Ph.D. programme.

Dated 04th July 2024 (LALRUATPUIA)

CONTENTS

List of Figures

List of Tables

CHAPTER -1
INTRODUCTION

Rare earth doped nanomaterials have potential applications in optics, multi color light emitting diodes (LEDs), plasma display channels, display systems, non-destructive testing, and medical applications such as high-resolution X-ray imaging fields like mammography (Reddy *et al*., 2015). The large Stokes shift, sharp emission spectra, long lifetime, multiphoton and up-conversion excitation, low toxicity, and decreased photo-bleaching of rare-earth (RE) nanomaterials over semiconductor nanocrystals like quantum dots and organic phosphor molecules make them an alternative for biological labeling and medical diagnostics. However, significant changes in the particle's physical and optical properties occurs as the particle size decreases. Consequently, understanding the spectroscopic properties of these materials is necessary for enhancing their emitting properties for technological applications.

1.1 Rare-earth ions/ Lanthanide

Rare earth elements comprise of a set of seventeen chemical elements from lanthanum (Z=57) to lutetium (Z=71). Additionally, Scandium (Sc) and Yttrium (Y) are also included in discussions of rare earth elements due to their similar properties and applications. Despite their name, they are relatively abundant in the Earth's crust, but they are dispersed and often found mixed with other elements, making extraction challenging and costly. All rare earth elements form trivalent cations (3+) characterized by chemical configuration $[Xe].4f^N6s^2$. Where N represents the number of electrons on the 4f subshell. The outermost 5s, 5p, and 6s electrons partially shield the 4f electrons. Because of this shielding, RE ions have special spectroscopic characteristics that set them apart from transition metals. Since their energy levels are not greatly affected by their surroundings, they do not differ significantly amongst hosts, and understanding their energy makes it simple to distinguish between the various electronic states. The energy levels of RE ions have been thoroughly documented in a number of works (Carnall *et al*., 1968; Carnall *et al*., 1988; Peijzel, 2005). Dieke, 1968 produced one such work, the so-called Dieke diagram, which

shows the multiple energy levels of different RE ions and is widely used to determine the electronic states of RE ions.

As a result of their spectroscopic properties, RE elements find application in various technological and industrial sectors, including electronics, telecommunications, renewable energy, defense technologies, and more. They possess unique properties that make them indispensable for many modern devices and technologies. These properties include high magnetic strength, catalytic activity, luminescence, and exceptional conductivity. To mention a few, weak blue and bright green emissions from Tb^{3+} ions doped glasses and glass ceramics are used in multicolor light emitting diodes (LEDs), plasma display channels, display systems, etc. In non-destructive testing and medical applications such as high-resolution X-ray imaging fields like mammography (Reddy *et al.,* 2015), the doped glass fibers come in handy. They are also used to lower the radiative dose when patients are exposed to them (Reddy *et al.,* 2015). Europium (Eu^{3+}) ions are used as the source of commercial red luminous phosphor. Which are also typically utilized to create devices for telecommunications or displays. Strong emission from praseodymium (Pr^{3+}) provides laser transition in the blue, green, orange, and red regions (Fanai *et al.,* 2019). Doping with Pr^{3+} also results in a lattice distortion that improves the materials' electroluminescence, optoelectronic, and gas sensing performance (Santhanamn *et al*., 2023; Fang *et al*., 2023). Samarium (Sm^{3+}) emits an orange-red light, which is widely used to make for high-density memory, underwater communications, and color displays (Li *et al.,* 2018). Additionally, Sm^{3+} ion-doped materials are used in planner waveguides and compressed fiber lasers. (Sales *et al.,* 2019).

Another interesting property that lanthanide also exhibits is that when exposed to high intensity radiation or particles like UV, X-rays, and neutrons, it undergoes a number of interesting changes in its characteristics (Sharma *et al*., 2009; Zou *et al*., 2017). The combination of enhanced luminescent properties, stability, tunable emission spectra, high sensitivity, and versatility makes rare earth-doped calcium aluminate an excellent choice for long-lasting phosphors and dosimetry applications.

These characteristics ensure reliable and accurate radiation monitoring, which is essential for safety in various fields involving ionizing radiation.

γ- irradiation and x-rays are photons of high energy and are able to travel longer distances than β-irradiation. These radiations have the ability to extract electrons from the material's atoms and create electron-hole pairs and ion pairs that follow the path of charged particles. Irradiation of material by thermal neutron is known to cause several types of damages. The interaction maybe either elastic or inelastic. In elastic collision, some of the kinetic energy of the incident neutron is transferred to the lattice causing displacement of ions from their original lattice sites (Rai *et al.*, 2023). If the neutron is captured by a nucleus, a nuclear reaction resulting in the ejection of an α-particle can take place (Rai *et al.*, 2023). In this instance, atom displacement could result in lattice vacancies. Breakup of the covalent bonds in the crystal may also take place under neutron impact (Hellwege, Faust, 1948). The reduction of rare earth (RE) ions by a thermal neutron irradiation has been investigated by Rai *et al*. (Rai, Thakur,1993; Rai, 2012). Studied the trichlorides of Pr^{3+} & Ho^{3+} and obtained change in the oxidation state of the ion through the creation of electron-hole pairs in the microcrystallites present in the powder. The divalent ions and the center thus formed regain properties after storing at room temperature. The irradiation effect also causes changes in the optical characteristics of glasses by creating additional emission and absorption bands. It is reported that after gamma irradiation, there is a decrease in the intensities of the IR bands accompanied by losing sharpness (ElBatal *et al.*, 2012) for TM-doped (Ti-Cu) lithium diborate glasses and generated induced absorption in the UV and visible region due to collective sharing of the intrinsic defects in the host glass and extrinsic defects due to trace iron impurities (ElBatal *et al.*, 2010) for sodium phosphate glass containing cobalt. PL intensity decline to a reasonable intensity with a red shift was found in Nd doped phosphate glass (Rai *et al.*, 20101). These results indicate that irradiation produces different kinds of defects in the glass material along with the conversion of the valence state of Nd^{3+} to Nd^{2+} (ElBatal *et al.*, 2012), which was investigated by Rai et al. For sample containing Sm^{3+} doped strontium phosphate glasses, the PL peaks intensity decrease with increasing Sm^{3+} content after being

irradiated an 8 Mrad, dose as reported by Okasha *et al*. (2018) and Madhu *et al*. (2020) proving thermal stability and a decrease in the energy band gap for doped lead-boro-tellurite glass after irradiated with 30 kGy. Hari Babu *et al*. (2012) and ElBatal *et al*. (2005) observed the photoreduction of Sm^{3+} to Sm^{2+} ions, which is more stable at room temperature for doped oxyfluoroborate glasses, where intrinsic flaws are discovered because the glass contains impurities or dopants. Marzouk *et al.* (2018) studied the extension of the UV absorption due to suggested transformation of some Fe^{2+} ions to additional Fe^{3+} ions by capturing positive holes during the irradiation process, but Sm^{3+} absorption remains unchanged because of shielding effects of the outer 5s and 5p orbitals on the 4f electrons (Marzouk *et al.*, 2018) for Sm^{3+} doped LiAl fluorophosphate glasses. However, not much information is available on the effect of γ- irradiation on Sm^{3+} doped pure silicon dioxide (SiO_2) glass matrix, which information was also reported in this thesis. The valency reduction from Sm^{3+} to Sm^{2+} ions is observed after gamma irradiation; that result is in strong agreement with Rai *et al.* (Rai, Thakur, 1993; Rai, 2012) and Hari Babu *et al.* (2012).

Energy migration between RE ions is another significant characteristic of RE elements, which enhances their emission intensity, lifetimes, and quantum efficiencies. Interaction between luminescent ions that involve f-f transitions only with enhanced emission from one species (Van Uitert *et al.*, 1966). Because of its many technological applications, the energy transfer process has become increasingly important in the fields of optoelectronics and photonics. As a result, numerous energy transfer research studies involving lanthanide ions, such as those involving the tripositive ions Tb-Eu (Zheng *et al.*, 2020), Pr-Yb (Tanabe *et al.*, 2010), Dy-Tb (Ravita *et al.*, 2021), Sm-Eu (Brito *et al.*, 2020), Eu-Dy (Som *et al.*, 2016), Ho-Yb (Georgescu *et al.*, 2014), and Ce-Tb (Ca *et al.*, 2021) have been conducted for different hosts. The detail studied of energy transfer from Tb^{3+} to Eu^{3+} is highlighted in this report since the emission bands of Tb^{3+} have overlap with some excitation bands of Eu^{3+} and Tb^{3+} can act as a donor for the emission of Eu^{3+}. Energy transfer with multipolar interaction in nature with dipole-dipole, quadrupole-quadrupole interaction with dominant type of interaction was reported for Tb^{3+}, Eu^{3+} co-doped with zinc phosphate glass (Caldiño *et al.*, 2013) and zinc

aluminoborosilicate glass (Zheng *et al.*, 2020). Works of Pisarska *et al.* (2014), Said *et al.* (2019), and Chaofeng Zhu *et al.* (2013) showed the dominant mechanism for energy transfer of Tb^{3+} to Eu^{3+} co-doped lead borate, metaphosphate, and aluminosilicate glass was multipolar interaction in nature, respectively.

1.2 Glasses as a host for RE ions

RE-doped glasses have been the focus of numerous studies since Snitzer's ground breaking work in 1961. Their adaptability has led to a wide range of applications, particularly in solid state laser and optical amplifier devices. The long-range order and regularity in atomic arrangement present in crystals are absent from amorphous glasses (Zachariasen, 1932). Consequently, the environment that surrounds RE ions doped in glasses is more unpredictable and varied. Therefore, compared to crystal hosts, there are slight differences in the ions' energy levels, which lead to wider absorption and emission lines (Weber, 1979).

Over time, a wide variety of glasses have been investigated and utilized as RE ions' hosts (Weber, 1990; Cases *et al.*, 1991; Rakov *et al.*, 2002; Wang *et al.*, 2007). Various types of glasses have different structural and optical properties, which in turn affect the spectroscopic properties of RE ions, which make them useful for certain applications. One crucial aspect of glasses is their transparency, which varies among different types of glasses (Yamane *et al.*, 2000). Because of the wide band gap between the valence and conduction bands, oxides and fluoride glasses are typically transparent in the visible region, whereas chalcogenides with smaller band gaps are translucent in the visible region but transparent in the infrared region. Due to the chemical reactivity of the raw materials, the synthesis of heavy metal fluoride glasses, such as fluoro zirconates, requires extremely carefully controlled environments. Nevertheless, these glasses also have high transparency up to mid-infrared wavelengths. Other than silica, oxide glasses such as phosphates, germinates, borates, and tellurites are also employed in various opto-electronic devices utilizing their special qualities. However, they are often expensive to produce and exhibit inferior chemical durability.

Silica is thought to be a good host for RE ions because of its exceptional mechanical strength, UV transparency, and chemical and thermal stability

(Fanderlik, 1991; Sigel Jr, 1977). Because of its high optical transparency in the visible, near-infrared, and deep ultraviolet regions, silica glass is a highly advantageous host for RE ions. One disadvantage of silica is that its comparatively high phonon energy causes the luminescence of RE ions to occur with less efficiency, a phenomenon called multi-phonon relaxation (Reisfeld *et al.*, 1987). When the number of phonons needed to bridge the energy gap between an excited state and the next lower energy state decreases, the rate of non-radiative multi-phonon relaxation increases. An excited state's ion can lose energy to the host lattice's vibration in the form of multiple phonons (Fanai *et al.*, 2016). Thus, multi-phonon relaxation effectively quenches luminescence from energy states in silica glass that would have stronger emissions in hosts like fluorozirconates and tellurites with lower phonon energy. Another drawback of silica glass is the low solubility of RE ions which leads to concentration quenching (Minascalco, 2001). Almeida *et al.* (1998) state that because the RE ions have high coordination numbers, they must share the glass matrix's finite supply of non-network oxygen (NNO) atoms. When RE concentrations are low, ions can be dispersed uniformly and bound to NNO atoms in RE–Si–O bonds (Fanai *et al.*, 2016); however, when concentrations rise, RE–O–RE bonding forms clusters. These cluster formations may result in energy transfer between the RE ions, concentration quenching, and a decrease in luminescence. Because the interionic distance has a significant impact on the rate of energy transfer between RE ions, clusters of RE ions close to one another encourage energy migration among themselves, which leads to concentration quenching. Through phonon assisted energy transfer or cross-relaxation, an ion in the emitting level may lose energy to a nearby ion (Auzel, 2004). This would quench the luminescence that would otherwise occur in the absence of the energy transfer. The energy level structure of RE ions affects the cross-relaxation process, and some are more susceptible to it than others. RE-ion-activated silica-based glasses continue to be a desirable material for integrated optics. In the field of optical materials and photonics, one area of interest is figuring out how to increase the luminescence efficiency of RE ions in silicon. The potential to create optically confined structures has created new avenues for the creation of innovative optical components. This work aims to discuss the latest developments in RE-activated silicon-based photonic

systems and suitable fabrication protocols that enable optical and spectroscopic properties to be enhanced and tailored.

1.3 Co doping

As was indicated in the previous section, pure silica has a few drawbacks that limit its usefulness as effective luminescent material despite the fact that it has many advantages over other glasses. Many studies have been conducted over the years and it has been discovered that appropriate co-doping enhances the luminescence characteristics of RE-doped silica glass.

In the recent years, many semiconductor nanoparticles doped with rare earth ions have undergone ongoing research since it has been demonstrated that as particle size is decreased, significant changes in the particle's physical and optical properties occur. The study was continued by Hazarika *et al.*(2008); Bokatial *et al.*(2011); Zhang and Peng (2012); Fanai *et al.* (2016), and Khan *et al.* (2020). There have been numerous reports on the effect of Ag, CdS, TiO_2, Al_2O_3, and ZnO nanomaterials on the spectroscopic properties of RE doped glasses. Among the $A_{II}B_{IV}$ group semiconductors, the unique electrical and optical characteristics of ZnS nanoparticles, which result from size quantization, make it an appropriate candidate host for RE ions. ZnS is a nontoxic semiconductor, which is significant as long as it possesses a very wide band gap (Eg 3.6 eV), high fluorescence efficiency, robust stability, and exceptional optoelectronics properties (Park *et al*., 2018; Radevici *et al*., 2013). Among various nanomaterials, ZnS doped Tb^{3+} ions are preferred because of Tb^{3+} ions long wavelength when it is integrated into ZnS. Poornaprakasha *et al*. (2018) reported that Tb^{3+} doped quantum dots are potential prospects for luminous and photocatalysis applications since their photocatalytic activity for the degradation of dyes was higher than that of the undoped ZnS quantum dots. Furthermore, it was discovered that the doping concentration of terbium affected the paramagnetic property of the doped ZnS nanoparticles. Hien *et al*. (2020) reported that multi-phonon relaxation's contribution to nonradiative relaxation from the $^5D_4$ level of Tb^{3+} is that very small ions exhibit effective PL even in highly phonon energetic hosts such as borate and silicate glasses. Layne *et al.* (1977) and Zhu *et al.* (2010) also reported that strong emissions in the visible range are produced by the radiative

transitions from the $^5D_4$ to the ^7F_J states, and the $^5D_4$ -$^7F_5$ transition in particular creates a vivid green emission with numerous optoelectronic and display applications. The works of Ahemen *et al*. (2016) and Bindu *et al*. (2022) claimed that the on doping with ZnS, the emission lines of Eu^{3+} in the orange-red and blue-green regions were enhanced. A combination of these two transitions gave white light of different shades from cool white light to warm white light. ZnS doped with Pr can enhance the photocatalytic properties, and in some materials, doping with Pr results in a lattice distortion that improves the materials' electroluminescence, optoelectronic, and gas sensing performance was shown by Fang *et al*. (2023). In studies of ZnS: Sm^{3+} nanophosphor, Ashwin *et al*. (2020) revealed that the photoluminescence and chromaticity studied show that it can be highly useful for photonic applications.

1.4. Sol-gel synthesis

Traditionally, glasses are made using the melt-quench method, in which the constituent raw materials are melted and fused, then shaped to the desired shape and finally quenched to prevent crystallization (Cable, 1984). This method works well for a large range of glasses that have lower melting temperatures; however, temperatures above 2000°C are needed for silica to melt. By using a chemical reaction between liquid precursors, the sol-gel technique allows for the synthesis of silica glass at lower temperatures as compared with melt glasses. In addition to the benefits presented by low temperature, dopant and concentration can be very accurately controlled in the solution stage when working with the low concentrations of RE ions; this is important. Sol-gel glasses have the potential to hold much higher concentrations, beyond the threshold where melt glasses lose their structure. In this method, a colloidal solution, or sol, is formed by a reaction of typically metal alkoxides and water. Tetraethyl orthisilicate (TEOS) and tertramethyl orthisilicate (TMOS) are frequently used in the synthesis of silica glass. This chemical process starts with the formation of a ‘sol,’ or colloidal solution, which then progressively develops into a gel-like diphasic system with a liquid phase and a solid phase, with morphologies ranging from discrete particles to continuous polymer networks. When it comes to the colloid, the volume fraction of particles (or particle density) might be

so low that it would take a considerable amount of fluid to be initially removed in order to notice the gel-like characteristics. There are several methods available to achieve this. Pouring off the remaining liquid after allowing sedimentation to occur is the simplest method. Additionally, phase separation can be sped up with centrifugation. The residual liquid (solvent) phase must be removed by drying, which typically causes a large amount of shrinkage and densification. The rate at which the solvent can be removed is ultimately determined by the porosity distribution in the gel. One distinctive feature of sol-gel synthesized silica that cannot be achieved using conventional techniques is its high porosity. In comparison to melted glasses, the porous gels' density and refractive index are extremely low. Due to the precursors' liquid state, the sol-gel process also permits excellent homogeneity because it permits vigorous stirring and mixing of the constituents. Unwanted contaminants and heterogeneities in glasses can have a negative impact, lowering transparency and increasing scattering loss. The final component's microstructure will definitely be significantly impacted by modifications made to the structural template during this processing phase. Also, the sol-gel process allows the synthesis in a much wider range of shapes and sizes, including thin films and fibers. Our research focuses on understanding the structure of sol-gel glasses and overcoming the features that hinder fluorescence output.

REFERENCES

Virendra N. Rai, Surya N. Thakur (2023) Chapter 2 - Physics and instrumentation of photothermal and photoacoustic spectroscopy of solids Editor(s): Surya N. Thakur, Virendra N. Rai, Jagdish P. Singh. *Photoacoustic and Photo. Spectros.* 21-49. doi: https://doi.org/10.1016/B978-0-323-91732-2.00026-4

Hellwege K. H., Faust W. L. (1948) Naval Research Laboratory 4 95.

Reddy Parthasaradhi C., Naresh V., Ramaraghavulu R., Rudramadevi B.H., Ramakrishna Reddy K.T., Buddhudu S. (2015) Energy transfer-based emission analysis of ($Tb^{3+,}$ Sm^{3+}): Lithium zinc phosphate glasses. *Spectro. Acta Part A* **144**: 68-75. doi: https://doi.org/10.1016/j.saa.2015.02.090

Zhang Yunxia, Gautom Kumar Das, Xu Rong and Timothy Thatt Yang Tan (2009) Tb-doped iron oxide: bifunctional fluorescent and magnetic nanocrystals. *J. Mater. Chem.* **19**:3696–3703. doi: https://doi.org/10.1039/B817159A

Carnall W.T., Fields P.R., Rajnak K. (1968) Spectral Intensities of the Trivalent Lanthanides and Actinides in Solution. II. Pm^{3+}, Sm^{3+}, Eu^{3+}, Gd^{3+}, $Tb^{3+,}$ Dy^{3+}, and Ho^{3+}. *J. Chem. Phys.* **49**:4412-4428. doi: https://doi.org/10.1063/1.1669892

Carnall W.T., Goodman G.L., Rajnak K., Rana R.S. (1988) A systematic analysis of the spectra of the lanthanides doped into single crystal LaF3, Argonne National Laboratory, Argonne, IL.

Peijzel P.S., Meijerink A., Wegh R.T., Reid M.F., Burdick G.W. (2005) A complete 4fn energy level diagram for all trivalent lanthanide ions. *J. Solid State Chem.* **178**:448-453. doi: http://dx.doi.org/10.1016/j.jssc.2004.07.046

Dieke G.H. (1968) Spectroscopy & Energy Levels of Rare Earth Compounds, Inter Science, New York.

Zhang Liaolin , Peng Mingying, Dong Guoping , Qiu Jianrong (2012) An investigation of the optical properties of Tb^{3+}-doped phosphate glasses for green fiber laser. *Opt. Mater.* **34**: 1202-1207. doi: http://dx.doi.org/10.1016/j.optmat.2012.01.031

Reza Dousti M., Ghoshal S.K., Raja J.Amjad, Sahar M.R., Fakhra Nawaz, Arifin R. (2013) Structural and optical study of samarium doped lead zinc phosphate glasses. *Opt. Mater.* **300**: 204-209. doi: https://doi.org/10.4028/www.scientific.net/AMR.1107.403

Fanai A.L., Khan U., Rai S. (2019) Luminescence enhancement of Pr^{3+} doped sol-gel silica glass as a result of Al^{3+} co-doping. *J. Non-Crys. Solids* **503-504**: 89-93. doi: https://doi.org/10.1016/j.jnoncrysol.2018.09.027

Younes Hanifehpour, Behzad Soltani, Ali Reza Amani-Ghadim, Behnam Hedayati, Bamin Khomami, Sang Woo Joo (2006) Praseodymium-doped ZnS nanomaterials: Hydrothermal synthesis and characterization with enhanced visible light photocatalytic activity. *J. Ind. and Eng. Chem.* **34**: 41. doi: https://doi.org/10.1016/j.jiec.2015.10.032

Balakarthikeyan R., Santhanam A., Vinoth S., Ahmed A. Abdeltawab, Sayed Z. Mohammady, Mohd Ubaidullah, Shoyebmohamad F. Shaikh, Mohammad Shahzad Samdani, M. Aslam Manthrammel, Mohd Shkir (2023) Enhancing the optoelectronic properties of low-cost nebulizer spray pyrolysis (NSP) prepared ZnS thin film through praseodymium doping for photodetector

applications. *Mater. Sci. Eng. B* **289**: 116213. doi: https://doi.org/10.1016/j.mseb.2022.116213

Zhang Qixian, Shuyi Ma, Rong Zhang, Kaiming Zhu, Yue Tie, Shitu Pei (2019) Optimization NH_3 sensing performance manifested by gas sensor based on Pr-SnS_2/ZnS hierarchical nanoflowers. *J. Alloys. Compd.* **807**: 151650. doi: https://doi.org/10.1016/j.jallcom.2019.151650

Lee Y. H., Ju B. K., Song M. H., Hahn T. S., Oh M. H., Kim D. H. (1996) Effect of an interlayer on the emission characteristics of a white-light-emitting electroluminescent device with a Pr and Ce doubly doped ZnS phosphor layer. *J. Appl. Phys.* **79**: 8717- 8724. doi: https://doi.org/10.1063/1.362498

Qiannan Fang, Conghui Huang, Yuxia Zhang, Chengchun Zhao, Shuang Cai, Shanming Li, Yin Hang (2023) Effects of Pr^{3+} doping concentration on optical properties of LaF_3 crystal. *Opt. Laser Technol.* **159**: 109021. doi: https://doi.org/10.1016/j.optlastec.2022.109021

Li K., Deun R.V. (2018) Photoluminescence and energy transfer properties of a novel molybdate KBaY $(MoO_4)_3$: Ln^{3+} (Ln^{3+} = Tb^{3+}, Eu^{3+}, Sm^{3+}, Tb^{3+}/Eu^{3+}, Tb^{3+}/Sm^{3+}) as a multi-color emitting phosphor for UV w-LEDs. *Dalton Trans.* **47**;6995. doi: https://doi.org/10.1039/C8DT01011K

Hien N.T., Ca N.X., Kien N.T., Luyen N.T., Do P.V., Thanh L.D., Van H.T., Bharti S., Wang Y., Thuy N.T.M., Tan P.M. (2020) Structural, optical properties, energy transfer mechanism and quantum cutting of Tb^{3+} doped ZnS quantum dots. *J. Phys. and Chem. of Solid.* **147**:109638. doi:https://doi.org/10.1016/j.jpcs.2020.109638

Quang V.X., Do P.V., Ca N.X., Thanh L.D., Tuyen V.P., Tan P.M., Hoa V.X., Hien N.T. (2020) Role of modifier ion radius in luminescence enhancement from $^5D_4$ level of Tb^{3+} ion doped alkali-alumino-telluroborate glasses. *J. Lumin.* **221**:117039. doi:https://ui.adsabs.harvard.edu/link_gateway/2020JLum..221k7039Q/doi:10.1016/j.jlumin.2020.117039

Sales T.O., Amjad D.J., Jacinta C., Dousti MR. (2019) Concentration dependent luminescence and cross-relaxation energy transfers in Tb^{3+} doped fluoroborate glasses. *J. Lumin.* **205**:282-286. doi: http://dx.doi.org/10.1016/j.jlumin.2018.09.031

Sharma K., Singh S., Prajapat C.L., Bhattacharya S., Singh M.R., Yusuf S.M. and Kothiyal G.P. (2009) Preparation and study of magnetic properties of silico phosphate glass and glass-ceramics having iron and zinc oxide. *J. Magn. Magn. Mater.* **321(22)**: 3821-3828. doi: https://doi.org/10.1016/j.jmmm.2009.07.047

Zou X., He L., Tan D., Lei F., Jiang N., Zheng Q., Lin D., Xu C. and Liu Y. (2017) Anneal-induced transformation of phase structure, morphology and luminescence of $GdPO_4$:Sm^{3+} nanomaterials synthesized by a hydrothermal method. *Dalton Trans.* **46**: 2948-2956. doi: https://doi.org/10.1039/C6DT04583A

El Batal F. H., Hamdy Y. M. and Marzouk S. Y. (2008) Gamma ray interactions with V_2O_5-doped sodium phosphate glasses. *Matr. Chem. Phys.* **112(3)**: 991-1000. doi: https://doi.org/10.1016/j.matchemphys.2008.07.005

Fatma H. ElBatal, Mona A. Ouis, Reham M.M. Morsi, Samir Y. Marzouk (2010) Interaction of gamma rays with some sodium phosphate glasses containing cobalt. *J. Non-Cryst. Solids* **356(1)**: 46-55. doi: https://doi.org/10.1016/j.jnoncrysol.2009.09.030

Rai V.N., Raja Sekhar B.N., Kher S. and Deb S.K. (2010) Effect of gamma ray irradiation on optical properties of Nd doped phosphate glass. *J. Lumin.* **130(4)**:582-586. doi: https://doi.org/10.1016/j.jlumin.2009.10.034

Okasha Aly, Abdelghany A. M., Mohamed S. K., Marzouk S. Y., El-Batal H. A., Gaafar M. S. (2018) Gamma ray interactions with samarium doped strontium phosphate glasses. *J. Mater. Sci.: Mater. Elect.* **29**:20907. doi: https://doi.org/10.1007/s10854-018-0234-3

Zeng, X., Xu, X., Wang, X., Zhao, Z., Zhao, G., & Xu, J. (2008) Effects of gamma-irradiation and air annealing on Yb-doped $Y_3Al_5O_{12}$ single crystal. *Spectro. Acta Part A* **69(3)**:860-864. doi: https://doi.org/10.1016/j.saa.2007.05.042

Rai S., Thakur SN (1993) Thermal neutron irradiation study of trichlorides of Pr and Ho by photoacoustic techniques. *Ind. J. Pure Appl. Phys.* **31**:552-555.

Rai V.N., Raja Sekhar B.N., Jagtap B.N. (2012) Study of gamma induced defects in Nd doped Phosphate glass using Uv-Vis Spectrophotometer and photo-physics beamline on Indus-I. *Asian J. Spectrosc.*, special issue, 143-154.

Zachariasen W.H. (1932) The atomic arrangement in glass. *J. Am. Ceram. Soc.* **54**: 3841-3851.

Weber M.J. (1979) Solid State Lasers, (Ed.) Tang C.L. In: Methods of Experimental Physics: Volume 15- Quantum Electronics Part A, Academic press, New York, 167-207.

Weber M.J. (1990) Science and technology of laser glass. *J. Non-Cryst. Solids* **123(1-3)**: 208-222. doi: https://doi.org/10.1016/0022-3093(90)90786-L

Cases R, Chamarro M.A. (1991) Judd-Ofelt analysis and multiphonon relaxations of rare earth ions in fluorohafnate glasses. *J. Solid State Chem.* **90(2)**: 313-319. doi: https://doi.org/10.1016/0022-4596(91)90148-B

Rakov N., Maciel G.S., de Araujo C.B., Messaddeq Y. (2002) Energy transfer assisted frequency upconversion in Ho3+ doped fluorindate glass. *J. Appl. Phys.* **91(3)**: 1272-1276. doi: https://doi.org/10.1063/1.1430889

Wang X., Lin H., Yang D., Lin L., Pun E. (2007) Optical transitions and upconversion fluorescence in Ho3+/Yb3+ doped bismuth tellurite glasses. *J. Appl. Phys.* **101**: 113535-1-6. doi: https://doi.org/10.1063/1.2743737

Yamane M., Asahara Y. (2000) Glasses for Photonics, First ed., Cambridge University Press, UK.

Fanderlick I. (1991) Silica Glass and Its Applications, Elsevier, Amsterdam.

Sigel Jr. G.H. (1977) "Optical absorption of glasses," in Treatise on Materials Science and Technology, edited by M. Tomozawa and H. Doremus, Vol. 12, Academic Press, New York, pp. 5-89.

Reisfeld R., Jørgensen C.K. (1987) Excited State Phenomena in Vitreous Materials, Elsevier, Amsterdam.

Minascalco W.J. (2001) "Optical and Electronic Properties of Rare Earth Ions in Glasses," in Rare-Earth-Doped Fiber Lasers and Amplifiers, edited by M.J.F. Digonnet, 2nd edn., Marcel Dekerr Inc., New York, pp. 17-112.

Almeida R.M., Vasconcelos H.C., Goncalves M.C., Santos L.F. (1998) XPS and NEXAFS studies of rare-earth doped amorphous sol-gel films. *J. Non-Cryst. Solids* **232**: 65-71. doi: https://ui.adsabs.harvard.edu/link_gateway/1998JNCS..232...65A/doi:10.1016/S0022-3093(98)00545-6

Rai S., Fanai A.L. (2016) Optical properties of Ho3+ in sol-gel silica glass co-doped with Aluminium. *J. Non-Cryst. Solids* **449**:113118. doi: https://doi.org/10.1016/j.jnoncrysol.2016.07.023

Auzel F. (2004) Upconversion and Anti-Stokes Processes with f and d Ions in Solids. *Chem. Rev.***104(1)**: 139-173. doi: https://doi.org/10.1021/cr020357g

Rai S., Hazarika S. (2008) Fluorescence dynamics of Tb^{3+} and Tb^{3+}/Ho^{3+} doped phosphate glasses. *Opt. Mater.* **30**: 1343-1348. doi: https://doi.org/10.1016/j.optmat.2007.06.016

Rai S., Bokatial L. (2011) Effect of CdS nanoparticles on photoluminescence spectra of Tb^{3+} in sol–gel-derived silica glasses. *Bull. Mater. Sci.* **34**: 227–231.

Liaolin Zhang, Mingying Peng, Guoping Dong, Jianrong Qiu (2012) An investigation of the optical properties of Tb^{3+}-doped phosphate glasses for green fiber laser . *Opt. Mater.* **34**: 1202-1207.doi: http://dx.doi.org/10.1016/j.optmat.2012.01.031

Khan Uzair Md, Fanai A. L., Rai S. (2020) Spectroscopic properties of Sm^{3+} and CdS co-doped in sol-gel silica glass. *Ind. J. Pure Appl. Phy.* **58**:157-163.

Park J.Y., Lee C.G., Seo H.W., Jeong D.W., Kim M.Y., Kim W.B., Kim B.S. (2018) Structural and optical properties of ZnSe: Eu/ZnS quantum dots depending on interfacial residual europium. *Appl. Surf. Sci.* **429**:225-230. doi: https://doi.org/10.1016/j.apsusc.2017.09.018

Radevici I., Sushkevich K., Sirkeli V., Huhtinen H., Nedeoglo D., Paturi P. (2013) Luminescent properties of the ZnSe: Yb crystals in the visible spectral range. *J. Lumin.* **143**: 275-279.doi: https://doi.org/10.1016/j.jlumin.2013.05.010

Poornaprakasha B., Chalapathia U., Youngsuk Suha, Prabhakar Vattikutib S.V., Siva Pratap Reddyc M., Si-Hyun Parka (2018) Terbium-doped ZnS quantum dots: Structural, morphological, optical, photoluminescence, and photocatalytic properties. *Ceramic Inter.* **44**: 11724-11729. doi: https://doi.org/10.1016/j.ceramint.2018.03.250

Layne C.B., Lowdermilk W.H. and Weber M.J. (1977) Multiphonon relaxation of rare-earth ions in oxide glasses. *Phys. Rev. B* **16**:10-20. doi: https://doi.org/10.1103/PhysRevB.16.10

Zhu C., Liang X., Yang Y. and Chen G. (2010) Luminescence properties of Tb doped and Tm/Tb/Sm co-doped glasses for LED applications. *J. Lumin.* **130**: 74-77. https://doi.org/10.1016/j.jlumin.2009.07.023

Ahemen, De D.K., Dejene F.B., Viana B. (2016) White light tunable emissions from ZnS: Eu^{3+} nanophosphors over 330–465 nm excitation range for white LED applications. *Mater. Res. Express* **3**:045016. doi: 10.1088/2053-1591/3/4/045016

Bindu, K.R., Safeera, T.A. & Anila, E.I. (2022) Pure red luminescence and concentration-dependent tunable emission color from europium-doped zinc

sulfide nanoparticles. *J. Mater. Sci: Mater. Electron* **33**:17793–17801. doi: http://dx.doi.org/10.1007/s10854-022-08644-5

Ashwini K., Pandurangappa C., Avinash K., Srinivasan S., Stefanakos E. (2020) Synthesis, characterization and photoluminescence studies of samarium doped zinc sulfide nanophosphors. *J. Lumin.* **221**:117097. doi: https://doi.org/10.1016/j.jlumin.2020.117097

Cable M. (1984) Principles of Glass Melting, (Eds.) Uhlmann D.R., Kreidle N.J., In: Glass Science and Technology, Vol. 2, Academic Press, Orlando, 1-44.

Setsuhisa, Taku Kouda, Teiichi Hanada (2000) Energy transfer and 1.3 μm emission in Pr–Yb codoped tellurite glasses. *J. Non-Cryst. Solids* **274(1–3)**:55-61. doi: https://doi.org/10.1016/S0022-3093(00)00183-6

Ravita, A.S. Rao (2021) Effective energy transfer from Dy3+ to Tb3+ ions in thermally stable KZABS glasses for intense green emitting device applications. *J. Lumin.* **239**:118325. doi: https://doi.org/10.1016/j.jlumin.2021.118325

Suzanny Lima Brito, Thiago Augusto Lodi, Robson Ferrari Muniz, Alysson Steimacher, Franciana Pedrochi (2020) Energy transfer investigation of Sm3+/Eu3+ CaBAl glasses. *J. Lumin.* **219**:116947. doi: https://doi.org/10.1016/j.jlumin.2019.116947

Georgescu Serban, Angela Stefan, Ana-Maria Voiculescu, Octavian Toma, Cristina Matei, Ruxandra Birjega (2014) Peculiarities of the Ho3+→Yb3+ energy transfer in CaSc2O4: Ho:Yb. *J. Lumin.* **154**:142-147. doi: https://doi.org/10.1016/j.jlumin.2014.04.021

Zheng Xingxing, Maolin Yang, Guanhua Wang, Wenli Zhou, Jilin Zhang, Liping Yu, Ping Wang, Zhongxian Qiu, Chengzhi Li, Shixun Lian (2020) Luminescence tuning of Tb/Eu Co-doped zinc aluminoborosilicate glasses for white LED applications. *Ceramics Inter*. **46(17)**: 26608-26615. doi: https://doi.org/10.1016/j.ceramint.2020.07.129

Caldiño U., Álvarez E., Speghini A., Bettinelli M. (2013) New greenish-yellow and yellowish-green emitting glass phosphors: Tb3+/Eu3+ and Ce3+/Tb3+/Eu3+ in zinc phosphate glasses. *J. Lumin.* **135** :216-220. doi: https://doi.org/10.1016/j.jlumin.2012.10.013

Pisarska Joanna, Agnieszka Kos, Marta Sołtys, Lidia Żur, Wojciech A. Pisarski (2014) Energy transfer from Tb3+ to Eu3+ in lead borate glass. *J. Non-Cryst. Solids* **388**:1-5. doi: https://doi.org/10.1016/j.jnoncrysol.2014.01.019.

Said Hajer, Refka Oueslati Omrani, Laura Ruiz Arana, Dhouha El Bahri, Slim Boussen, Chaker Bouzidi, Huayna Terraschke, Ahmed Hichem Hamzaoui, Adel M'nif (2019) The effect of silica additive on the structural and luminescence properties of Eu3+/Tb3+ co-doped metaphosphate glasses. *J. Mol. Struc.* **1192**: 42-48. doi: https://doi.org/10.1016/j.molstruc.2019.04.087

Zhu Chaofeng, Stéphane Chaussedent, Shujiang Liu, Yanfei Zhang, André Monteil, Nathalie Gaumer, Yuanzheng Yue (2013) Composition dependence of luminescence of Eu and Eu/Tb doped silicate glasses for LED applications. *J. Alloys Compd.* **555**:232-236. doi: https://doi.org/10.1016/j.jallcom.2012.12.052

ElBatal F.H., Ibrahim S., Abdelghany A.M. (2012) Optical and FTIR spectra of NdF3-doped borophosphate glasses and effect of gamma irradiation. *J. Mole. Struc.* **1030**:107-112. doi: https://doi.org/10.1016/j.molstruc.2012.02.049

Van Uitert L.G., Dearborn E.F., Rubin J.J. (1966) Mechanisms of Energy Transfer Involving Trivalent Tb and Sm. *J. Chem. Phys.* **45**:1578–1584. doi: https://doi.org/10.1063/1.1727801

Som S., Mitra P., Kumar Vijay, Kumar Vinod, Terblans J. J., Swarta H. C., Sharma S. K. (2014) Energy transfer phenomena and colour tunability in $Y_2O_2S:Eu^{3+}/Dy^{3+}$ micro-fibers for white emission in solid state lighting application. *Dalton Trans.* **43**: 9860-9871. doi: https://doi.org/10.1039/C4DT00349G.

Ca N.X., Vinh N.D., Bharti S., Tan P.M., Hien N.T., Hoa V.X., Peng Y., Do P.V. (2021) Optical properties of Ce3+ and Tb3+ co-doped ZnS quantum dots. J. *Alloys Compd* **883**: 160764. doi: https://doi.org/10.1016/j.jallcom.2021.160764

CHAPTER-2
EXPERIMENTAL

As this research is basically experimental in nature, the experimental procedures and techniques are as important as the data analysis and are integral parts of the research. This chapter summarizes the experimental aspects of the study while providing details to enable the work to be replicated. Due to the limitation of availability of equipment, recordings of X-Ray Diffraction (XRD), Transmission Electron Microscopy (TEM), Fourier Transform Infrared Spectroscopy (FTIR) were done in other institutions by other technician, while sample preparation and optical spectroscopy were done in our very own laboratory in the Department of Physics, Mizoram University, Tanhril, Aizawl, Mizoram.

2.1 Preparation of Glass Samples

The sol-gel technique is utilized for the preparation of a glass sample in which a silica host is formed as a result of the hydrolysis of tetraethyl orthosilicate (TEOS). When TEOS reacts with water, the ethoxy group in the TEOS is replaced by hydroxyl group, yielding silanol and ethanol as by-products as follows:

$$Si\,(OC_2H_5)_4 + 2H_2O \rightarrow SiO_2 + 4\,C_2H_5OH$$

The necessary amount of the RE (Tb^{3+}/ Eu^{3+}/Sm^{3+}/Pr^{3+}) compound (oxides, fluorides, chlorides, or nitrates), depending on the desired concentration, is dissolved in deionized water and stirred for 15 minutes using a magnetic stirrer in order to create RE doped samples. After dissolving, CH_3OH and TEOS were added in a dropwise manner along with a small amount of HNO_3 to lower the pH value and enhance the hydrolysis rate. Utilizing a magnetic stirrer, the mixture of TEOS, H_2O, CH_3OH, and HNO_3 in the molar ratio 1:5.5:3.5:0.1, along with the dissolved dopants, is stirred for one hour to form a sol (Fig. 2.1). In most instances, 1.5 ml of TEOS is utilized per sample while preserving the specified molar ratio among the constituents.

For samples co doped with ZnS nanoparticles, the powder form of ZnS was first dissolved in the presence of HNO_3, methanol, and distilled water. Then, the required amount of ZnS is added along with RE compound. The mixture was then

agitated for two hours. Now, the mixture is stirred for two hours in order to generate sol. The sol is allowed to settle into a gel for a few days at room temperature before being moved to a plastic container with a tight-fitting lid. After creating a few evaporation pinholes and waiting three weeks, a solid glass sample is produced. The sample mix batches were then individually placed into a muffle furnace and heated to 1000^0 C for an hour (Fig. 2.2). A simplified flow chart for sample preparation process is shown in Figs. 2.3 and 2.4.

For incorporating the dye doped samples, a two-step experiment was carried out. In the first step, for preparing different concentrations of Rh6G amid RhB dyes dissolved in Ethanol, the material is weighted according to the following relation:

$$W = \frac{\mathrm{C}x\mathrm{V}x\mathrm{M}}{1000} \tag{2.1}$$

Where W is the weight of material in (gm), C molar concentration (mol/l), M is the molecular weight (gm/l) and V is the volume of solvent used to dissolve the materials.

After that, the prepared solutions were diluted using the formula below:

$$M_1V_1 = M_2V_2 \tag{2.2}$$

where V_1 is the volume before dilution, V_2 is the volume after dilution, M_1 is the primary concentration and M_2 is the new concentration.

In step number two, for making a solid sample, the same procedure for RE doped samples which mentioned above is followed.

Fig. 2.1: A magnetic stirrer used to stir a mixture in the proper ratio.

Fig. 2.2: Annealing is done in muffle furnace.

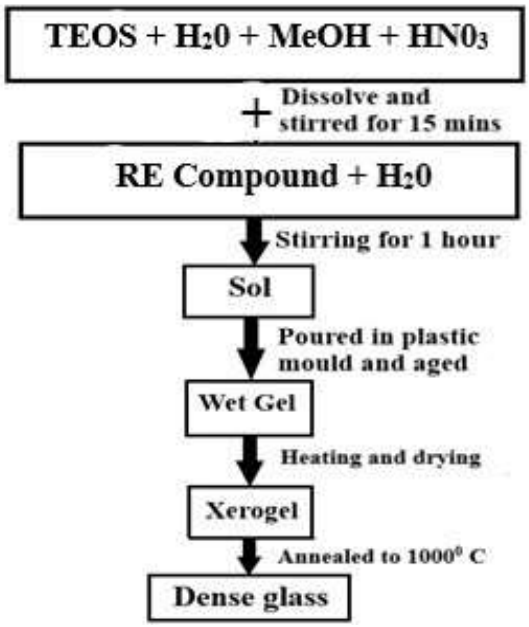

Fig. 2.3: Simplified flowchart of only RE doped sample preparation.

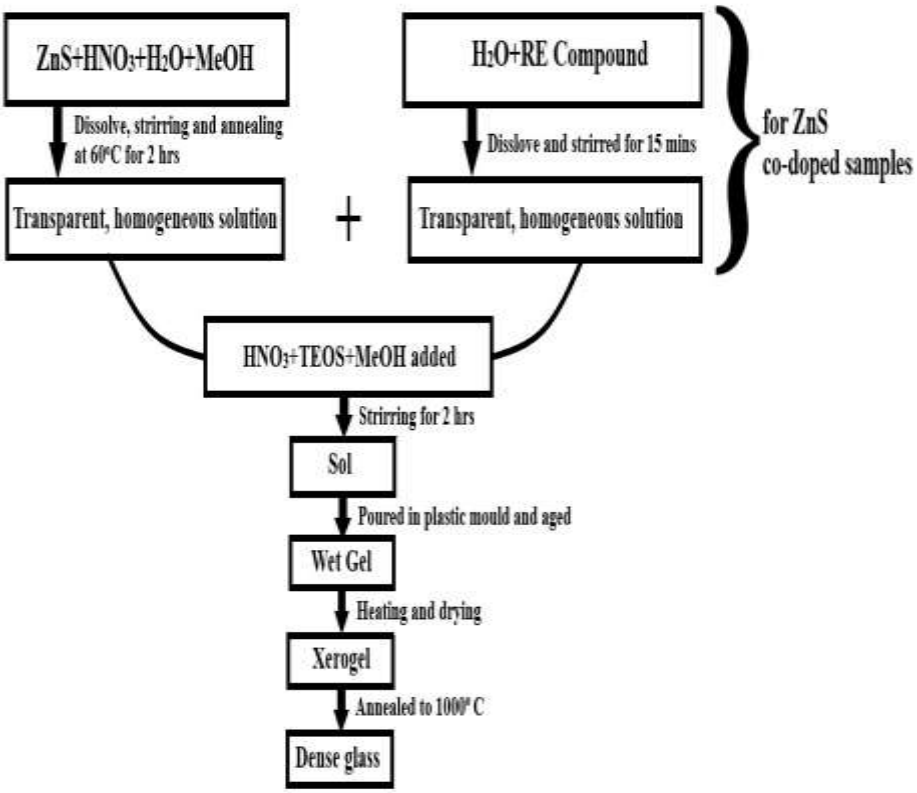

Fig. 2.4: Simplified flowchart of ZnS co-doped RE sample preparation.

2.2 Refractive index measurement

The refractive indices of the prepared glass samples must be known for optical studies, so a method for determining their refractive indices must be established. The method used for the measuring refractive index of the prepared samples was Abbe's refractometer (Fig. 2.5). Abbe's refractometer working principle is based on the principle of total internal reflection. The refractive index of the studied sample is determined by measuring the change in direction of the radiation as it passes through one medium to another.

$$\frac{n_1}{n_2} = \frac{v_1}{v_2} = \frac{\sin\theta_1}{\sin\theta_2} \tag{2.3}$$

where v_1 is the velocity of propagation in the less dense medium M_1 and v_2 is the velocity in the denser medium M_2; n_1 and n_2 is their corresponding refractive indices. θ_1 and θ_2 is the angle of incidence and angle of refraction respectively (Fig. 2.6).

When M_1 is in vacuum, $n_1 = c$, the speed of light, n_1 is unity. Hence, equation (2.3) becomes

$$n_2 = n_{vac} = \frac{c}{v_2} = \frac{\sin\theta_1}{\sin\theta_2} \tag{2.4}$$

where n_{vac} is the absolute refractive index. The precision of the device is half of its accuracy, which is approximately ±0.0002.

Fig. 2.5: Abbe's refractometer.

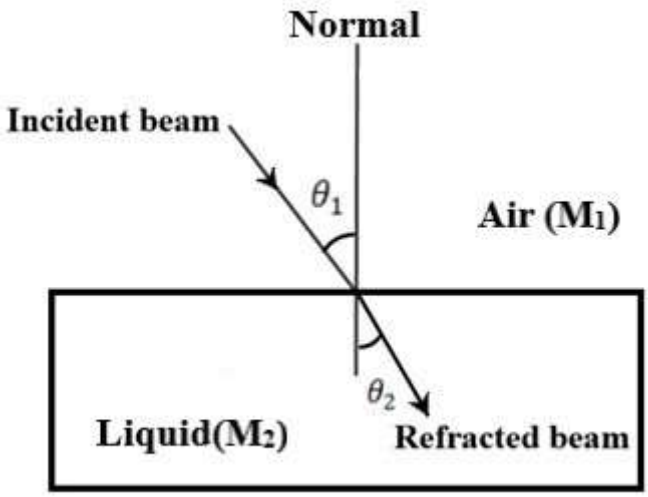

Fig. 2.6: Refraction of light.

2.3 Fourier Transform Infrared Spectroscopy (FTIR)

Fourier transform infrared spectroscopy is the most useful technique in the vibrational spectroscopic techniques. The working principle is based on the Michelson interferometer, which consists of a beam splitter, a fixed mirror, and a moveable mirror (Fig. 2.7). The light beam from a source strikes the beam splitters then parts of the light beam are transmitted to a fixed mirror and the other parts to a moveable mirror. Both the mirrors reflect the source beam through the beam splitter, and then through the sample and to the detector. The purpose of a moveable mirror is to create an optical path difference between the two split beams, which results in constructing destructive and constructive interference. Followed this process an interferogram and a plot of light intensity as a function of optical path difference are obtained. The information contained in the interferogram is then transformed into intensity vs wavenumber, which is expressed in cm^{-1}. IRAffinity-1S (SHIMADZU) from the Chemistry department, MZU were utilised for recording the FTIR spectra.

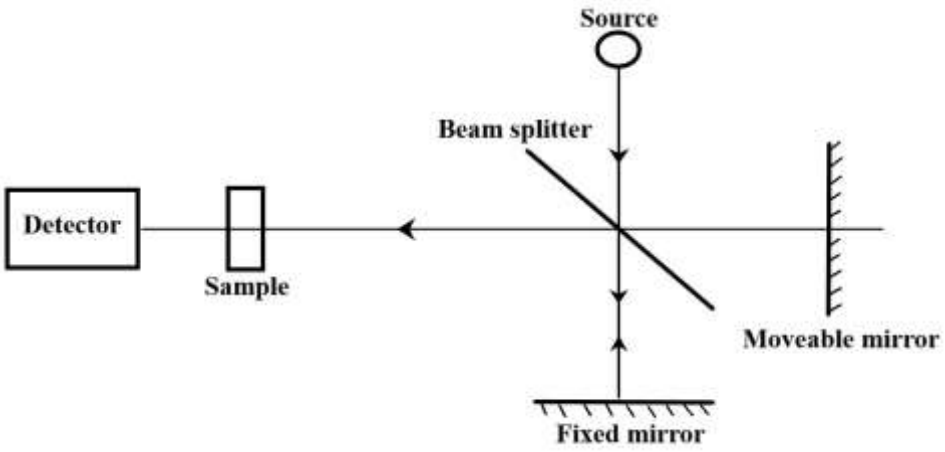

Fig 2.7: Component and operation schematic for an FTIR spectrometer

2.4 X-Ray Diffraction (XRD)

XRD analysis is one of the most common technique used for the determination of sample composition or crystalline structure. Its working principle is based on Bragg's law, which gives the relation the condition of constructive interference of the X-ray beams diffracted by the crystal lattice. If two parallel beams of light 1 and 2 are diffracted by the first and second crystal planes (Fig. 2.8) having 'd' spacing between them. Then, for constructive interference to occur, the path difference between the two diffracted beams must be a whole number multiple of the X-ray wavelength. If λ is the wavelength of the X-ray and θ is the angle between diffracted beams and the lattice plane, the condition for constructive interference is given by Bragg's law, which is given mathematically as

$$2d\sin\theta = n\lambda \tag{2.5}$$

Since the X-ray's wavelength is known in XRD analysis, the Bragg angles can be used to determine the lattice plane spacing. Crystals can be used to determine the composition of samples because they have distinctive XRD patterns. However, because of their irregular arrangement, amorphous materials lack the sharp peaks of crystals. For instance, the distinct peaks of crystalline SiO_2 (quartz) in silica glass combine to form a broad peak. The peaks of crystalline samples can also be broadened as the crystallite size decreases, and this broadening can be used to estimate the crystallite size using the Scherrer formula given by

$$D = \frac{0.94\lambda}{\beta cos\theta} \quad (2.6)$$

where, β is the line broadening at FWHM in radius, λ is the X-ray wavelength, θ is the Bragg's angle, half of 2θ.

The finely powdered samples were analyzed using Panalytical Empyrean X-ray diffractometer at the BHU and CIF, IIT Gwahati. With a wavelength of 0.15406 nm, CuKα radiation is the source of the X-rays.

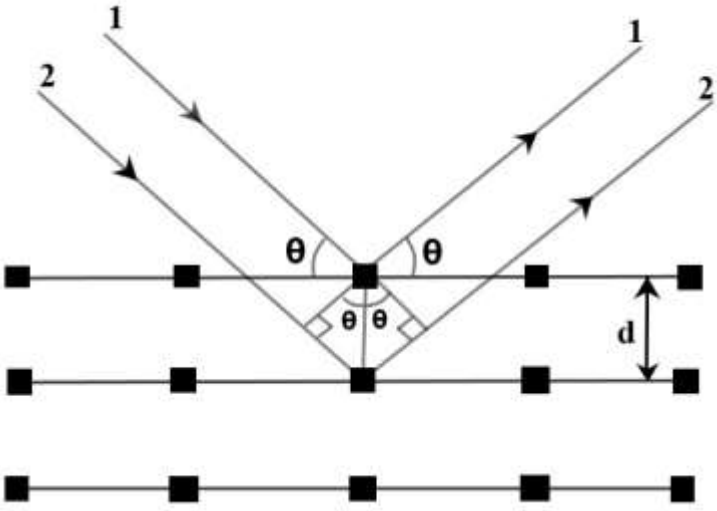

Fig. 2.8: Diffraction of radiation by crystal planes

2.5 Transmission electron microscopy (TEM)

TEM is used to create microstructure images of materials at a resolution significantly higher than that of optical microscopes. This is made possible by the electrons in an electron microscope having a wavelength that is significantly shorter than visible light (four orders of magnitude shorter). A TEM operates similarly to an optical microscope. In TEM, electron rays replace visible light beams, and electromagnetic lenses take the place of glass ones. Studied samples for TEM analysis need to be extremely thin, i.e., electronically transparent, in order to permit electron transmission. A schematic diagram of TEM is shown in Fig. 2.9.

The TEM images of the studied samples were taken by FEI Tecnai's HRTEM at IIT, BHU and CIF, IIT Gwahati.

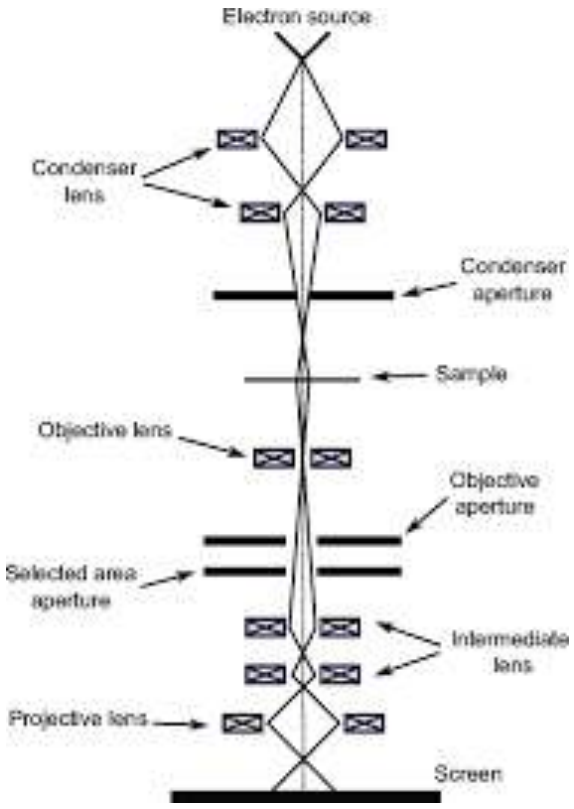

Fig. 2.9: Schematic diagram of TEM. (Source: Naresh Marturi. Vision and visual servoing for nanomanipulation and nanocharacterization in scanning electron microscope. Micro and nanotechnologies/Microelectronics. Universit´e de Franche-Comt´e, 2013)

2.6 Optical measurement

The iHR320 imaging spectrometer from Horiba Scientific, which is fitted with a CCD detector as shown in Fig. 2.10, and F-4700 Fluorescence Spectrometer from Hitachi, as shown in Fig. 2.13, were utilized for recording optical spectra of the studied samples.

iHR320 imaging spectrometer

A spectrometer has a distinct sample compartment that is highly adjustable to accommodate a variety of sample types. It does not contain an internal light source, so an appropriate external light source should be used for exciting the samples.

Fig. 2.10: iHR320 imaging spectrometer used for recording absorption and emission spectra.

For recording absorption spectra, an incandescent bulb is used as an external light source that has a broad continuous spectral range from visible to IR region. The absorption measurements are limited to the visible and near-IR regions because the UV emission of the light bulb is so weak that it is not suitable for recording UV absorption spectra. In order to measure the absorption spectrum, the sample is positioned in the sample compartment so that the light beam from the external light source falls on it and passes through to the monochromator (Fig. 2.10). The entrance slit of the monochromator is adjusted so as to maximize the amount of light entering the monochromator and reaching the detector. The incident light is then divided into its component wavelengths by the monochromator, and the CCD detector measures each wavelength's intensity within the necessary range. The same process is repeated, but this time the doped glass sample is replaced with an undoped reference sample. The reference sample is pure silica glass with no dopants added, but the preparation procedure is similar to that of RE doped samples. The readings for the studied sample and reference sample are then compared and analysed using the computer software to get the absorption spectrum.

Fig. 2.11: Block diagram showing arrangement for recording absorption spectrum.

For measuring the photoluminescence (PL) spectrum, the sample placed in the sample compartment is excited by an external light source at angle 90^{o} C so as to minimize the excitation light source entering the monochromator (Fig. 2.12). Filters maybe used for cutting down the light of unwanted wavelengths. The photoluminescence emission from the sample is then measured to determine the intensities of its various wavelength components as previously mentioned. The recorded spectra are restricted up to the 1100 nm wavelength range because the sensitivity of the CCD detector is limited beyond this wavelength range.

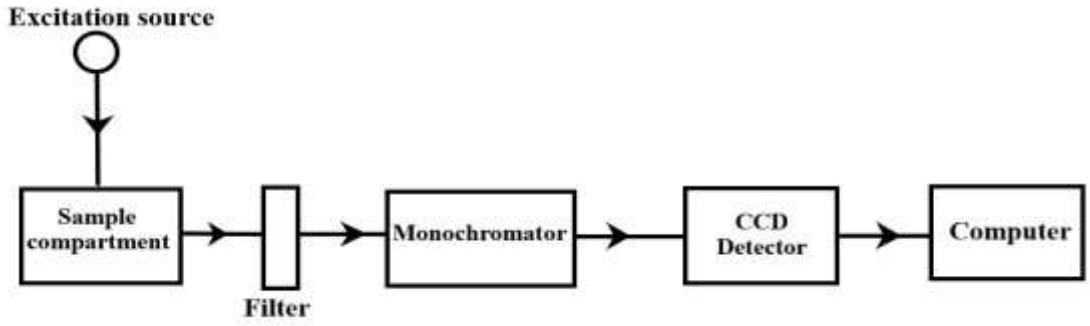

Fig. 2.12: Block diagram showing arrangement for recording PL spectrum.

F-4700 Fluorescence Spectrometer

A spectrometer is equipped with a phosphorescence measurement mode that allows for the detection of phosphorescence, which manifests as an afterglow after the excitation light extinction, by having the chopper rotate to irradiate the pulsed excitation light onto a sample (Fig. 2:14). A xenon light is used for exciting the sample.

Fig. 2.13: F-4700 fluorescence spectrometer used for recording excitation spectra.

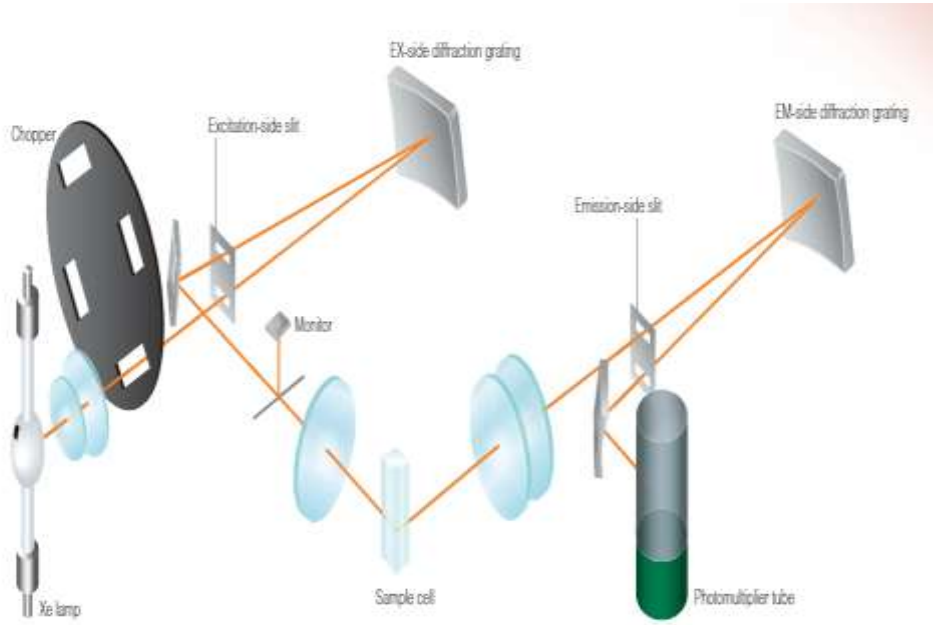

Fig. 2.14: Schematic diagram showing the optical system of F-4700 Fluorescence Spectrometer.

REFERENCES

Naresh Marturi (2013) Vision and visual servoing for nanomanipulation and nano characterization in scanning electron microscope. Micro and nanotechnologies/Microelectronics. Universit´e deFranche-Comt´e, English. <tel-01025318>.

CHAPTER-3
SPECTROSCOPIC STUDIES OF TB^{3+} AND EU^{3+} DOPED ZNS NANOPARTICLE

This chapter deals with the physical, structural, and spectroscopic studies of ZnS nanoparticles singly doped with Tb^{3+} and Eu^{3+} ions in a silica glass matrix.

3.1 Abstract

The ZnS nanoparticles doped with Tb^{3+} ions and ZnS doped silica glass-ceramic were synthesized by the sol-gel method. The density, refractive index, and various physical properties were calculated. X-ray diffraction (XRD) and selected area electron diffraction (SAED) studies confirm the formation of hexagonal polycrystalline structure. Transmission electron microscopy (TEM) analyses revealed that variation in size of the particles lies between 10 to 50 nm. FTIR were used to examine the structural characteristics of prepared glass samples at specific annealing temperatures. The band gap energy of the as-synthesized nanocomposite glass was 3.18 eV with a green light emission. The influence of ZnS nanoparticles on Tb^{3+} ions doped glass was studies by photoluminescence (PL) spectra. The PL emission intensity increased with the concentrations of ZnS. The CIE chromaticity revealed that the tunability of color changes from blue-green to yellowish green region as ZnS concentration increases.

The structural characterization and spectroscopic analyses of silica glass-ceramic doped ZnS nanoparticles with Eu^{3+} ions by the sol-gel method are also presented. Various physical properties including density and refractive index were computed. The formation of the blended structure and a hexagonal polycrystalline phase of ZnS is confirmed by studies using selected area electron diffraction (SAED) and X-ray diffraction (XRD). Analysis using Transmission Electron Microscopy (TEM) showed that the particles' sizes vary from 10 to 50 nm. The structural properties of prepared glass samples were examined using FTIR at various annealing temperatures. The band gap energy of as-synthesized doped ZnS glass-ceramic was 3.49 eV compared to bulk value (3.60 eV) with a pure green emission. Through photoluminescence (PL) spectra, the impact of ZnS nanoparticles on glass doped

with Eu^{3+} ions were investigated. The CIE color chromaticity and CCT reveal that the studied glass can be used for producing white light for commercial lighting purposes.

3.2 Experimental

Terbium (III) nitrate pentahydrate (99.9%), Europium (III) nitrate hexahydrate (99.9%), Zinc sulphide (99.9%), Tetraethyl orthosilicate (TEOS, 99.9%), methanol (99.9%), HNO_3, distilled water was purchased from Sigma- Aldrich. All solvents and chemicals were not further purified and were used directly. For sample preparation the mechanism highlighted in Chapter-2 is followed.

The refractive index of the studied glass sample was measured by an Abbe refractometer using 1-bromonaphthalene ($C_{10}H_7Br$) as an adhesive coating. By using the Archimedes principle, the density of the solid studied glass sample was determined with xylene (C_8H_{10}) as an immersion liquid. Diffuse reflectance spectra were created with a UV- Visible Spectrophotometer (Model: Evolution 220, Thermo Scientific, USA). The bandgap energy was calculated using the Kubelka-theory. The iHR320 imaging spectrometer from Horiba Scientific was used to study the PL spectra of the examined glass samples. An UV light source with a wavelength of 370nm and 25 W is used for exciting the sample. FTIR spectra were recorded by IRAffinity-1S (SHI-MADZU). Using a Cu-Kα radiation source-equipped X-ray diffractometer (Panalytical Empyrean), the crystal structure was examined. Additionally, the nano-composites' particulate nanostructure patterns were studied using FEI Tecnai's high-resolution transmission electron microscopy (HR-TEM) with a 300 kV acceleration voltage.

3.3 Results and Discussions

3.3.1 Terbium doped glass

3.3.1.1 Physical properties

The density of different concentrations of ZnS nanoparticles doped with a fixed amount of Tb^{3+} ion (0.5 mol %) in silica glass-ceramic was determined by using the Archimedes principle, where the sample was immersed in xylene. The

refractive index was measured by Abbe's refractometer. These two measured values are used for calculating another physical property such as Average molecular weight (M_T), Ion's concentration (N_i), Dielectric constant (ε_d), Optical dielectric constant (ε_d-1), Molar volume (V_m), Reflection Losses (R_L), Molar Refractivity (R_M), Energy gap (E_g), Polaron Radius (Rp), Interionic distance (R_i), Field strength (F_s), Molar polarizability (α_m) and Metallization Criterion (M_c) by using appropriate expressions (Devi *et al.,* 2019) and represented in Table 3.1. The electronic polarizability of the sample controls the non-linear dynamics of the materials. The material begins to exhibit electronic polarizability as it is subjected to strong light. Volt Lorentz-Lorentz theory (Haralampieva *et al.,* 2012) is utilized for deriving electronic polarizability (α_e) as follows:

$$\frac{(n^2-1)}{(n^2+1)} V_m = \frac{4}{3\pi} N\alpha_e \qquad (3.1)$$

where *n* is refractive index, V_m is molar volume and N is Avogadro's number.

Table 3.1: Various physical properties of different concentrations of ZnS nanoparticle doped with fixed amount of Tb^{3+} ions in silica glass-ceramic

Physical properties	**0.5 % Tb: *x* mol % ZnS**		
	***x* = 0 %**	***x* = 3%**	***x* = 5%**
Refractive index (n_i)	1.48	2.103	2.34
Density (ρ) (g/cm^3)	1.167	2.105	2.108
Thickness (Z_t)	0.212	0.213	0.214
Average molecular weight M_T (g)	61.94	63.07	63.82
Ion's concentration (N_i x 10^{20})	0.57	1.004	0.994
Dielectric constant (ε_d)	2.19	4.42	5.47
Optical dielectric constant (ε_d-1)	1.19	3.42	4.47
Molar volume (V_m) (cm^3/mol)	53.08	29.96	30.27
Reflection Losses (R_L)	0.019	0.284	0.36
Molar Refractivity (R_M)	19.80	18.90	20.91
Energy gap (E_g)	12.13	2.74	1.91
Polaron Radius (Rp x 10^{-8}) (cm^{-3})	1.55	1.87	1.86
Interionic distance (R_i x 10^{-7}) (cm^{-3})	2.6	2.15	2.19
Electronic polarizability (α_e x 10^{21})	1.12	2.11	2.37
Field strength (F_s x 10^{13})	88.2	61.31	61.8
Molar polarizability (α_m)	7.86	7.5	8.29
Metallization Criterion (M_c)	0.627	0.369	0.309

3.3.1.2 Structural properties

X-Ray Diffraction Study

Fig. 3.1 shows the study of XRD of ZnS (5 mol %) doped silica glass-ceramic annealed at 900°C. The diffraction peaks such as (100), (101), (110), (103), (200), (004), (202), (104), (203), (210), (211), (114), (105) and (212) revealed themselves in the ZnS sample, supporting the hexagonal phase of ZnS predicted by the JCPDS file data Nos. 00-80-0007 and also supported by the reported work (Zhao *et al.*, 2012; Ibupoto *et al.*, 2013). However, since the studied ZnS doped silica glass-ceramic was prepared by reaction between ZnS and SiO_2, there is formation of ZnO depicted by red color and the peak originated from SiO_2 itself is indicated by a star mark as shown in Fig. 3.1. These peaks are also well matched with JCPDS Card No. 01-076-0941 (for SiO_2) and 043-0002 (for ZnO). The Debye-Scherrer formula is used to determine the average crystallite size from the full-width at half-maximum (FWHM) of the sharpest diffraction peaks (Lima *et al.*, 2017).

$$D = \frac{0.94\lambda}{\beta cos\theta} \tag{3.2}$$

where β is the line broadening at FWHM in radius, λ is the X-ray wavelength, and θ is the Bragg's angle, half of 2θ. The particle size calculated was 23.85 nm.

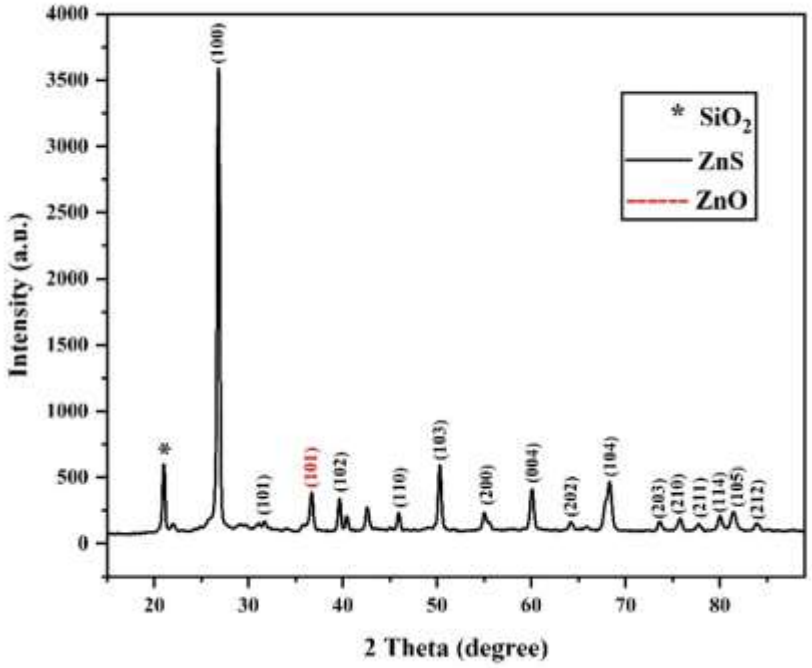

Fig. 3.1: X-ray diffraction (XRD) patterns of ZnS doped silica glass-ceramic annealed at 900° C

Transmission Electron Microscope (TEM)

The dimension, distribution, and structural morphologies of the nanoparticles can be revealed by the powerful technique known as TEM. Thus, by using TEM analysis, ZnS nanoparticle structure and shape were investigated. The TEM image of a big assembly of ZnS nanoparticles and the corresponding particle size distribution are shown in Figs. 3.2(a) and 3.2(b). After annealing at 900°C, it is possible to say that variation in size of the particles lies between 10 to 50 nm. In addition, the SAED image shows a set of ring structures, which reveals that the studied ZnS nanoparticles are polycrystalline in nature, which is also in accordance with diffraction from the different planes of ZnS nanoparticles. This result is persistent with the XRD analysis.

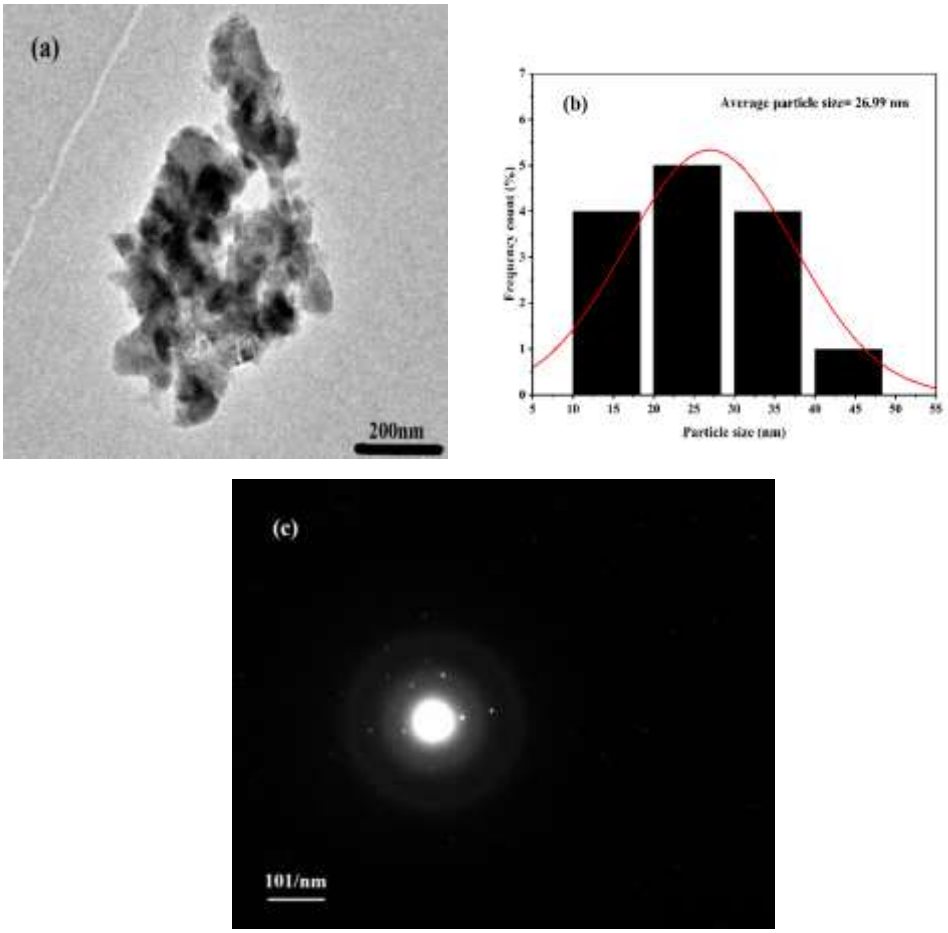

Fig. 3.2: (a) TEM image of ZnS nanoparticles doped silica glass-ceramic and (b) corresponding particle size distribution analysis (c) Selected Area Electron Diffraction image showing the diffraction pattern of ZnS nanoparticles doped silica glass- ceramic.

FTIR Spectra

Fig. 3.3 shows the FTIR spectra of 0.5% Tb^{3+} ions doped with 5 mol% of ZnS nanoparticles at different annealing temperatures. The spectra were recorded in the range of 400-4000 cm^{-1}. The samples in the gel stage contain a significant amount of water and other organics. An electric muffle furnace is used to gradually heat the acquired sample, which helps to create a strong glassy network by gradually removing various chemicals from the gel matrix. Dips at 1055 cm^{-1} and 1219 cm^{-1} are brought on by the stretching of the Si-O-Si, whereas dips at around 432 cm^{-1} and 771 cm^{-1} are brought on by the Zn-S vibration (i.e., the sulphide group). The peaks at roughly 1056.99 cm^{-1} are influenced by the doped Tb^{3+} ions in the glass matrix.

Absorbing CO_2 on the crystal's surface results in bands at 1519 cm^{-1}, which are C-O vibrational modes. The vibrations as a result of formation O-H stretching are related to bands at around 3741 cm^{-1} which are progressively disappearing indicating the removal of O-H vibrations with annealing.

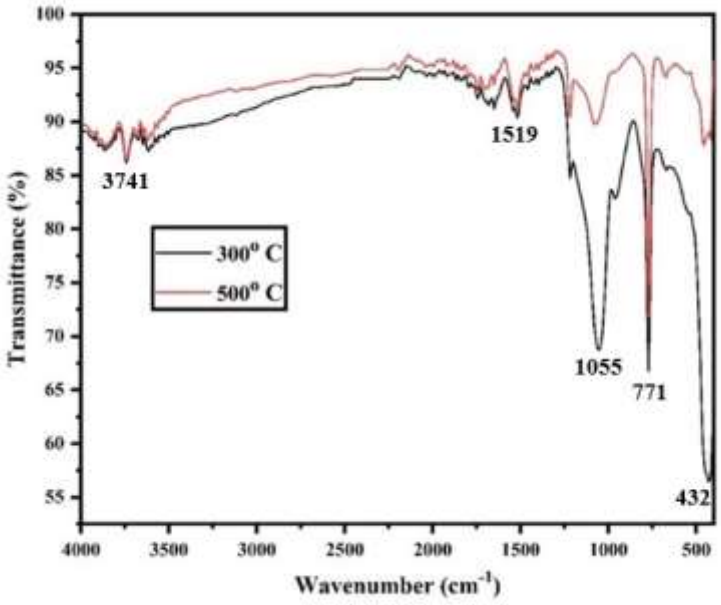

Fig. 3.3: FTIR spectra of Tb^{3+}(0.5%) ions doped ZnS (5 mol %) nanoparticles at different annealing temperature.

3.3.1.3 Optical properties of as-synthesized pure ZnS nanoparticle doped silica glass-ceramic

Absorption spectra

The UV-VIS spectra of as-synthesized pure ZnS nanoparticle doped silica glass-ceramic are shown in Fig. 3.4(a). It shows a strong absorption peak at around 248 nm which is slightly blue shifted from the bulk absorption at 340 nm, which is due to the quantum confinement effect of ZnS nanoparticles. ZnS effectively absorbs light with a wavelength range of 220-350 nm. The transition from the whole state in the valance band to the electronic state in the conduction band causes this absorption peak. It can be seen that there are no absorption spectra in the visible range (400 nm-

800 nm). The relation between the absorption coefficients (α) and incident photon energy (hv) is

$$(\alpha hv)^{1/p} = A(hv - Eg) \quad (3.3)$$

where A is a constant and E_g the bandgap of the material, h is Planck's constant, v is the frequency of radiation utilized to determine the direct energy band of synthesized materials from the high absorption region, and the exponent p depends on the type of the transition (Sang, *et al*., 2002). For direct and allowed transition p=1/2, indirect transition, p=2, and for direct forbidden, p=3/2 (Tauc, 1974; Tiwary *et al.*, 2009). For calculating the direct bandgap value $(\alpha h v)^2$ vrs. hv is plotted, and it is shown in the inset of Fig. 3.4(a). By extrapolating the straight portion of the graph on hv axis at α=0, the optical bandgaps of the room-temperature as-synthesized ZnS nanoparticles (Tiwary *et al.*, 2009) doped silica-glass ceramic have energy band gap values of 3.18 eV, it is found to increase by an amount of 0.42 eV when related to the absorption edge of the bulk ZnS (3.60 eV). When dealing with quantum confinement, the band gap energy increases with a decrease in the size of the particle and quantum confinement occurs as the particle size becomes the same or smaller than the Bohr radius. However, in the case of doped samples, the band gap decreases with the reduction of particle size. This phenomenon is termed the heavy doping effect. The change in the band gap energy is in line with the measured size of nanoparticles (Zhang *et al*., 2018). This size dependent variation in the band gap energy is due to quantum confinement effect (Tiwary *et al.*, 2009).

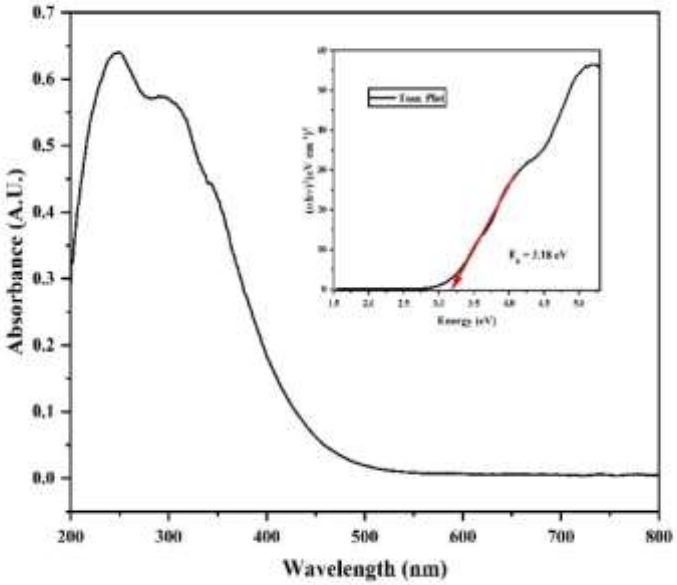

Fig. 3.4(a): UV-VIS absoprption spectra and Tauc plot of ZnS nanoparticle doped silica glass- ceramic.

PL spectra

The PL spectra of ZnS doped silica glass-ceramic annealed at 300° C excited by an UV light source with wavelength 370 nm and 25 W in the wavelength range 440 nm-800 nm is shown in Fig. 3.4(b). It is observed that green luminescence takes place from the peak at about 553 nm which can be attributed to the recombination between the sulphur vacancy (Tiwary *et al.*, 2009). Interstitial sulphur causes higher strain on the lattice because its ions are bigger than those of zinc. Due to this strain, electron levels coming from this site will have lower binding energies (Tiwary *et al.*, 2009). As a result, interstitial sulphur states should be situated towards the valence band edge.

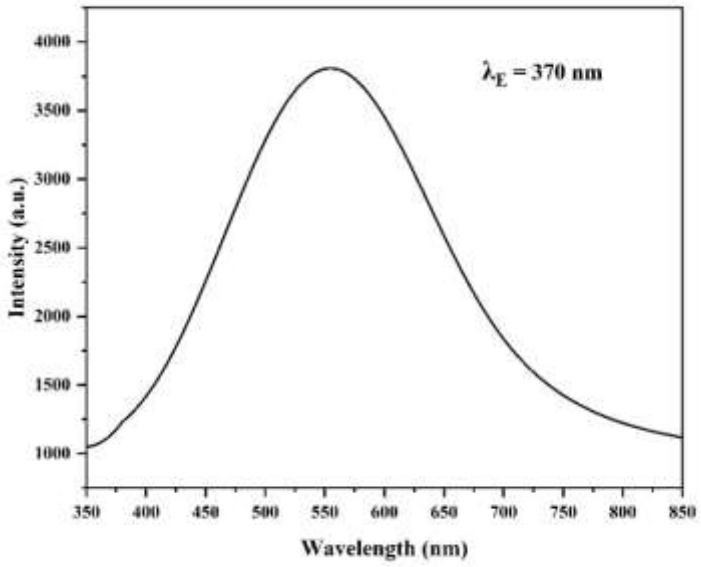

Fig. 3.4 (b) PL spectra of pure ZnS nanoparticle doped silica-glass ceramic annealed at 300° C.

3.3.1.4 Optical properties of different concentrations of ZnS nanoparticles doped Tb^{3+} ions

PL spectra

PL spectra of Tb^{3+} doped sol-gel silica glass with and without ZnS nanoparticles under λ_E= 370nm excitation are shown in Fig. 3.5. The characteristic peak of Tb^{3+} is observed with the dominated peak at 542 nm being ~ 7 times more intense for Tb^{3+} with ZnS nanoparticles in comparision to without ZnS nanoparticle. The possible explanation is that ZnS nanoparticles in the network of Si-Tb xerogel would increase the Si dangling and Oxygen vacancy in the network of Si. In this way, more electrons and holes can be easily excited, and radiant recombination were increased. The spectra reveals that there are four strong emission peaks at 489nm, 542nm, 585nm, 622nm corresponds to $^5D_4$-$^7F_6$, $^5D_4$-$^7F_5$, $^5D_4$-$^7F_4$, $^5D_4$-$^7F_3$ transitions, respectively. All assignments of transition bands are done with lanthanide spectra transition reported by Dieke (Dieke, 1968) and Carnal et al. (Carnall *et al.*, 1968). As we see in Fig. 3.5, the PL emission intensity increases as the host concentration increases. Tb^{3+} ions only sample show only relatively week PL intensity. Significant

improvement is observed when co-doped with ZnS, and intensity increases with increasing Tb^{3+}/ ZnS ratio (Fanai *et al.*, 2019). Doped nanoparticles are known to display rising emission efficiencies as well as the broadening of $^5D_4$ emission peaks also observed in the presence of ZnS. However, increasing concentration may lead to cluster formation and cracking of sample that would quench the fluorescence on account of that only up to 5 mol % of ZnS was utilized. No PL emission quenching was observed even when the ZnS concentration reached 5 mol%. It is observed that the $^5D_4$-$^7F_6$,$^5D_4$-$^7F_4$, $^5D_4$-$^7F_3$ emission peaks are slightly increased as the Tb^{3+}/ ZnS ratio increases, while the dominant green emission intensity $^5D_4$-$^7F_5$ peaks at 542nm sharply increases as the Tb^{3+}/ ZnS ratio increases, which can be easily observable with the naked eye. Also, $^5D_4$-$^7F_6$,$^5D_4$-$^7F_4$, $^5D_4$-$^7F_3$ peaks are slightly red shifted in the presence of ZnS.

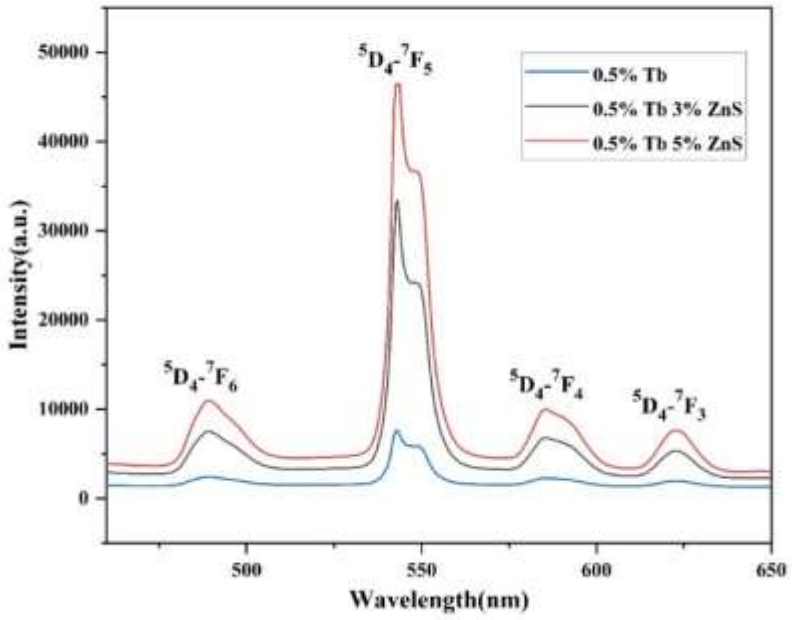

Fig. 3.5: PL Spectra of different concentrations of ZnS nanoparticles doped Tb^{3+} ions (0.5%) in silica glass matrix.

Effect of Annealing Temperature on PL spectra

The PL spectra of Tb^{3+} ions (0.5 %) doped with 5 mol % of ZnS nanoparticles in silica glass annealing at different temperatures (300, 600, 800, and 900^0 C) is

shown in Fig. 3.6(a) and Fig. 3.6(b) shows that the broad emission peak $^5D_4$-$^7F_5$ intensity vs annealing temperature shows an exponential increase with an annealing after 600^{o}C onwards. Due to the fact that sol-gel is a wet chemical process, there are a lot of hydroxyl groups present, which is why little intensity was seen after annealing at 300-600^{o}C. As seen from the figure, increasing annealing temperature removes the hydroxyl groups, resulting in dramatic PL intensity enhancement. The removal of the hydroxyl group causes a decrease in the weight of the sample with annealing. Annealing to 900^0 C also causes densification of the sample and the sealing of the pores that prevent the sample from being reabsorbed by ambient moisture and maintain the luminescence even after a long time (Fanai *et al.*, 2019).

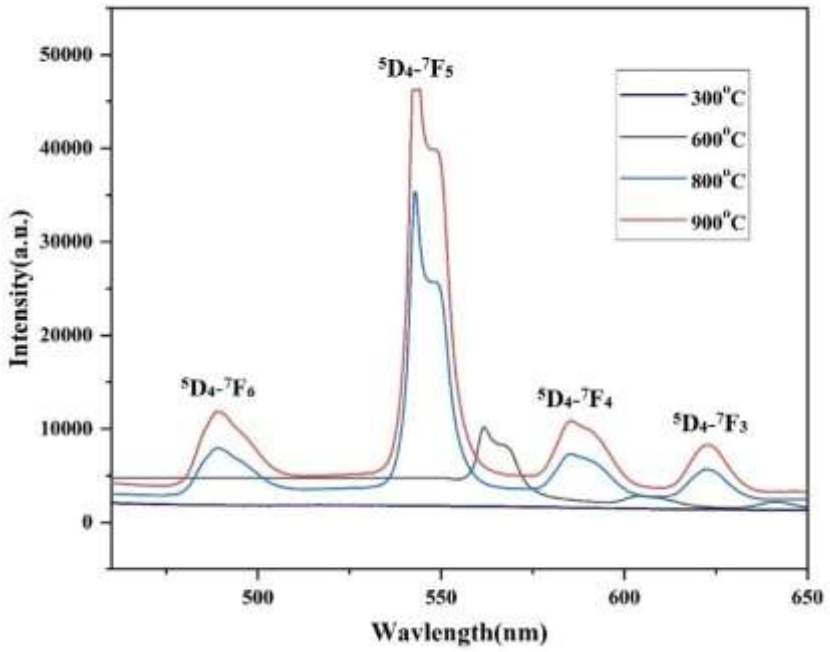

Fig. 3.6(a): PL Spectra of ZnS (5 mol %) nanoparticles doped Tb^{3+} ions (0.5%) in silica glass matrix at various annealing temperature.

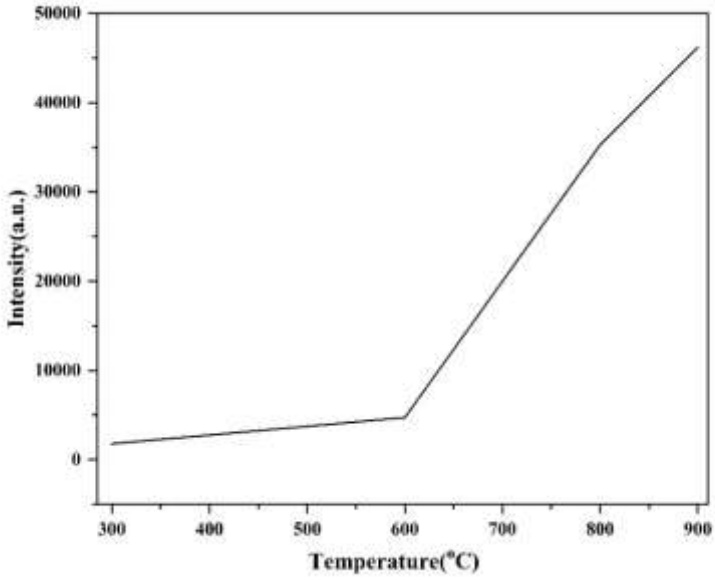

Fig. 3.6(b): PL intensity of $^5D_4$-$^7F_5$ transition Vs different annealing temperature

CIE Chromaticity

To ascertain the true nature of the material's color emissions, it is required to examine the color coordinates illustrated on a conventional chromaticity diagram**.** The CIE 1931 (Commission International d'Eclairage) diagram is a device used to measure the emission wavelength's tunability and the variation in the emission band's intensity. It is a global way of representing all conceivable colours by mixing three main colours. Fig. 3.7 shows the CIE Chromaticity diagrams of ZnS: Tb^{3+} that varying with the ZnS concentrations. The CIE Chromaticity coordinates of Tb^{3+} were derived based on their corresponding PL spectra at 370 nm excitation. The photoluminescence emission of different concentrations of Tb^{3+} ions doped with a fixed concentration of ZnS nanoparticles were illustrated using CIE 1931 chromaticity. The following equations are used to derive the chromaticity coordinates from the tri-stimulus values (Wang *et al.*, 2010).

$$x = \frac{X}{X+Y+Z} \tag{3.4}$$

$$y = \frac{Y}{X+Y+Z} \tag{3.5}$$

$$z = \frac{Z}{X+Y+Z} = 1 - x - y \qquad (3.6)$$

Table 3.2 shows the color coordinates for the samples that were under study. The color tunability changes from blue-green to yellowish green region as ZnS concentration increases.

Table 3.2: CIE chromaticity coordinates of Tb^{3+} ions doped different concentrations of ZnS nanoparticles in silica glass.

Colour Coordinates	**ZnS concentrations**		
	0%	**3.0%**	**5.0%**
X	0.3119	0.3050	0.3051
Y	0.3505	0.3984	0. 4032

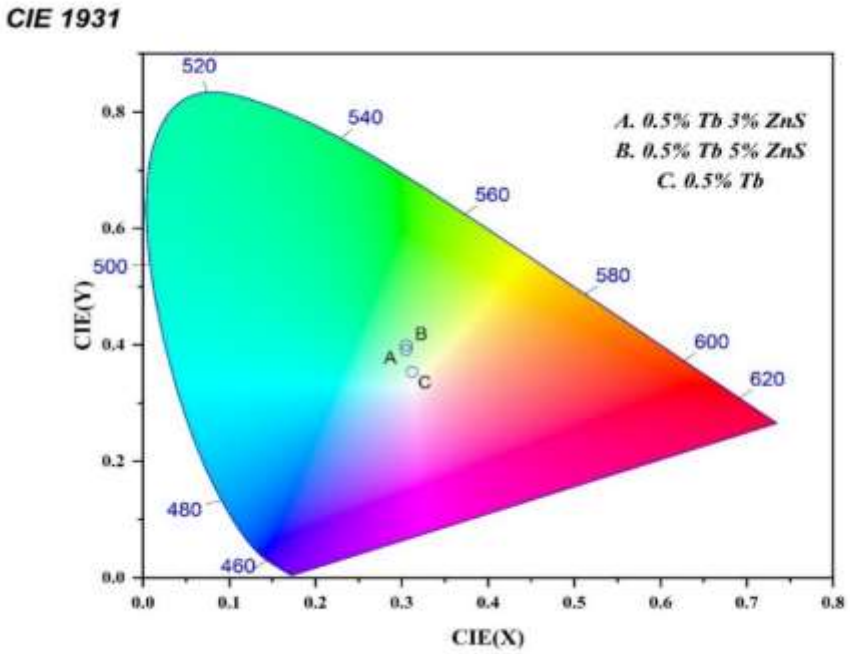

Fig. 3.7: CIE Chromaticity of concentration of ZnS (A=3.0%, B=5.0%, C=0%) doped with a fixed Tb^{3+} ions (0.5%) in silica glass.

3.3.2 Europium doped glass

3.3.2.1 Physical properties

Certain physical parameters of all these ZnS and Eu^{3+}-doped ZnS NPs in sol-gel silicate glass-ceramic have been calculated from the observed glass densities and refractive indices. These values were represented in Table 3.3. We use the method from our earlier work to estimate these values. Fig. 3.8 showed the density and molar volume of different concentrations of Eu^{3+} ion with a fixed concentration of ZnS NPs. The value of molar volume is maximum of 4.0 mol% and minimum for 0.75 mol%. For this specific glass composition, the maximum molar volume for 4.0 mol% indicates an increase in bond length and the interatomic spacing. An increase in the force constant and a shorter bond length of the bonds inside the network can account for the lower value of the molar volume for 4.0 mol%. The density of the glass samples increases as ZnS NPs are added to the silica glass because of the substitution of a higher molecular weight of ZnS (Mw. = 97.07 g/mol) into SiO_2 (Mw. = 60.08 g/mol). This shows that when ZnS substituted the place of SiO_2, the glass sample network became compressed. Changes in the field strength and polaron radius of different concentrations of Eu^{3+} ion doped ZnS nanoparticle are shown in Fig. 3.9. It was found that as the concentration of Eu^{3+} ions increase, the polaron radius falls proportionately. This decline could be brought on by an increase in the concentration of Eu^{3+} ions (N_i), which results in strong fields.

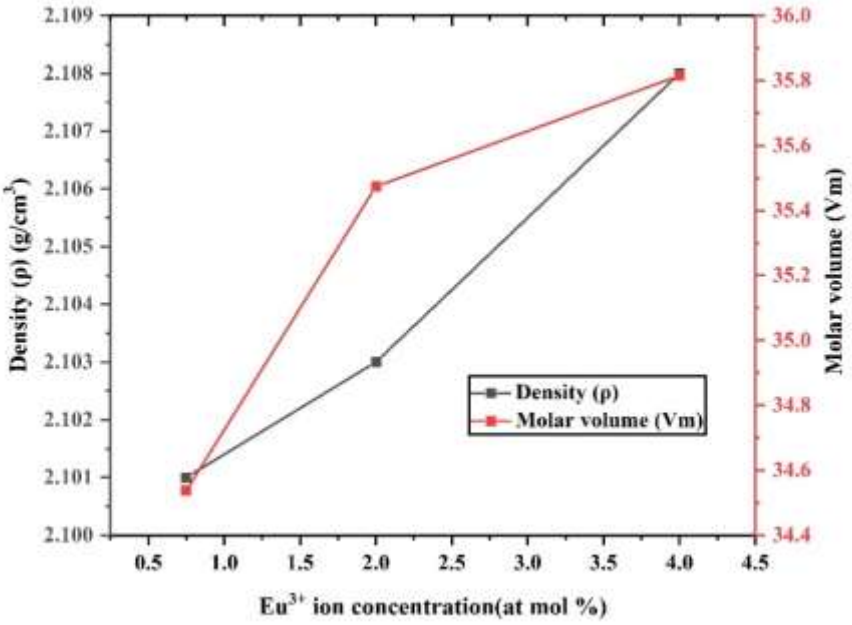

Fig. 3.8: Variation of density and molar volume as Eu^{3+} ion concentration changes.

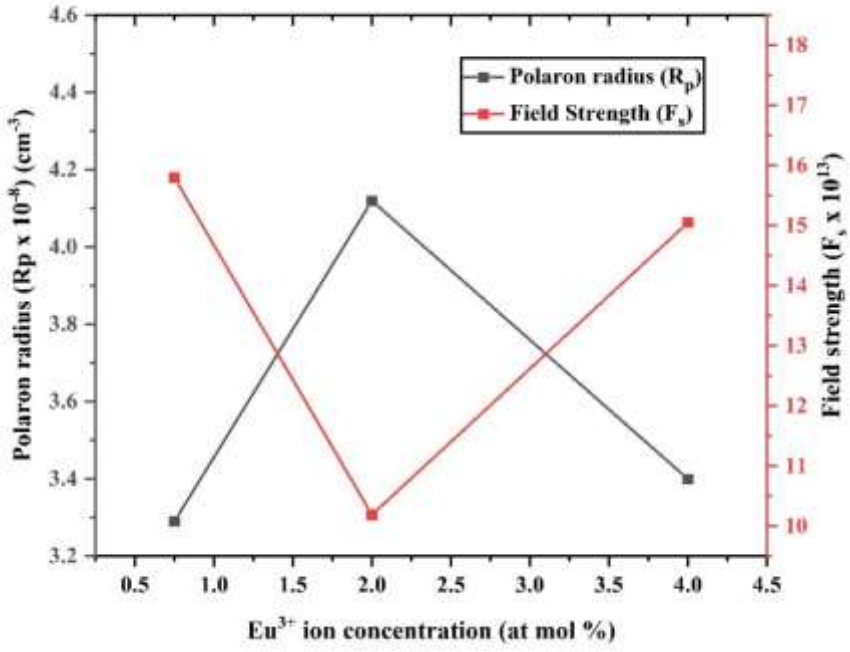

Fig. 3.9: Variation of polaron radius and field strength as Eu^{3+} ion concentration changes.

Table 3.3: Various physical properties of different concentrations of Eu^{3+} ions doped with a fixed amount of ZnS nanoparticle.

Physical properties	**1 mol% ZnS: *x* mol% Eu**		
	***x* = 0.75 %**	***x* = 2.0 %**	***x* = 4.0 %**
Refractive index (n_i)	2.342	2.347	2.352
Density (ρ) (g/cm^3)	2.101	2.103	2.108
Thickness (Z_t)	0.171	0.173	0.174
Average molecular weight M_T (g)	72.563	74.601	75.501
Ion's concentration ($N_i \times 10^{20}$)	1.85	3.395	6.72
Dielectric constant (ε_d)	5.484	5.508	5.53
Optical dielectric constant (ε_d-1)	4.484	4.508	4.53
Molar volume (V_m) (cm^3/mol)	34.537	35.474	35.816
Reflection Losses (R_L)	0.160	0.161	0.162
Molar Refractivity (R_M)	20.69	21.284	24.47
Energy gap (E_g)	3.216	3.22	2.009
Polaron Radius ($R_p \times 10^{-8}$) (cm^{-3})	3.29	4.12	3.4
Interionic distance ($R_i \times 10^{-7}$) (cm^{-3})	1.75	1.434	1.14
Electronic polarizability ($\alpha_e \times 10^{21}$)	2.37	2.382	2.38
Field strength ($F_s \times 10^{13}$)	15.8	10.19	15.05
Molar polarizability (α_m)	8.21	10.642	9.71
Metallization Criterion (M_c)	0.40	0.401	0.317

3.3.2.2 Structural properties

XRD study

Fig. 3.10 shows the XRD analysis of ZnS doped silica glass-ceramic annealed at 500° C. The diffraction peaks that appeared in the ZnS sample are in accordance with the blende crystal structure, which is matched with JCPDS Card No. 00-80-0020 and the hexagonal polycrystalline phase is also matched with JCPDS Card No. 00-80-0007. However, the star mark indicates that the peaks belong to SiO_2 and the red colour indicates the formation of ZnO since the studied sample was primarily prepared by the reaction between ZnS and SiO_2 in the presence of HNO_3 and methanol. These peaks match up nicely with JCPDS Cards Nos. 043-0002 (for ZnO) and 01-076-0941 (for SiO_2). The average crystallite size is calculated by using eqn (3.2). The crystallite size calculated was 22.86 nm.

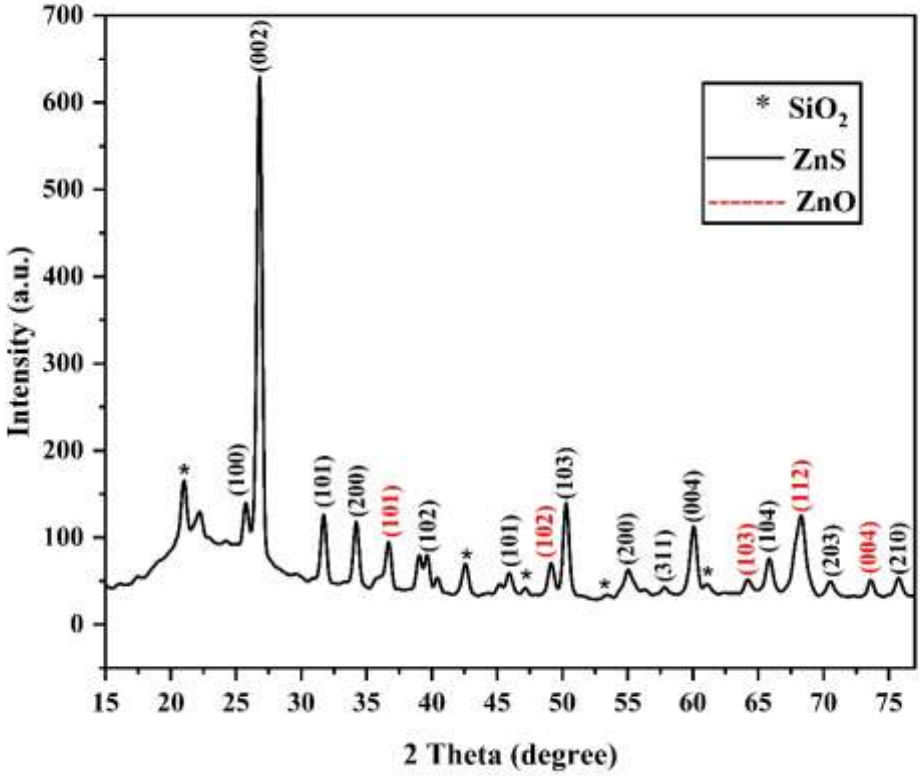

Fig. 3.10: XRD patterns of ZnS doped silica glass-ceramic annealed at 500° C.

TEM Analysis

The TEM technique can reveal the size, distribution, and structural morphologies of the nanoparticles. Therefore, ZnS nanoparticle doped silica glass ceramic structure and shape were examined using TEM analysis. The TEM image of a big assembly of ZnS nanoparticle doped silica glass ceramic and corresponding particle size distribution analysis are shown in Figs. 3.11(a) and 3.11(b) respectively. It is feasible to state that the range of particle sizes after 500°C annealing is between 10 and 50 nm. According to diffraction from the various planes of ZnS nanoparticle doped silica glass-ceramic, the SAED image displays a set of ring structure spots that indicate the present glass ceramic samples of ZnS nanoparticles are polycrystalline in nature. This result is persistent with the XRD analysis.

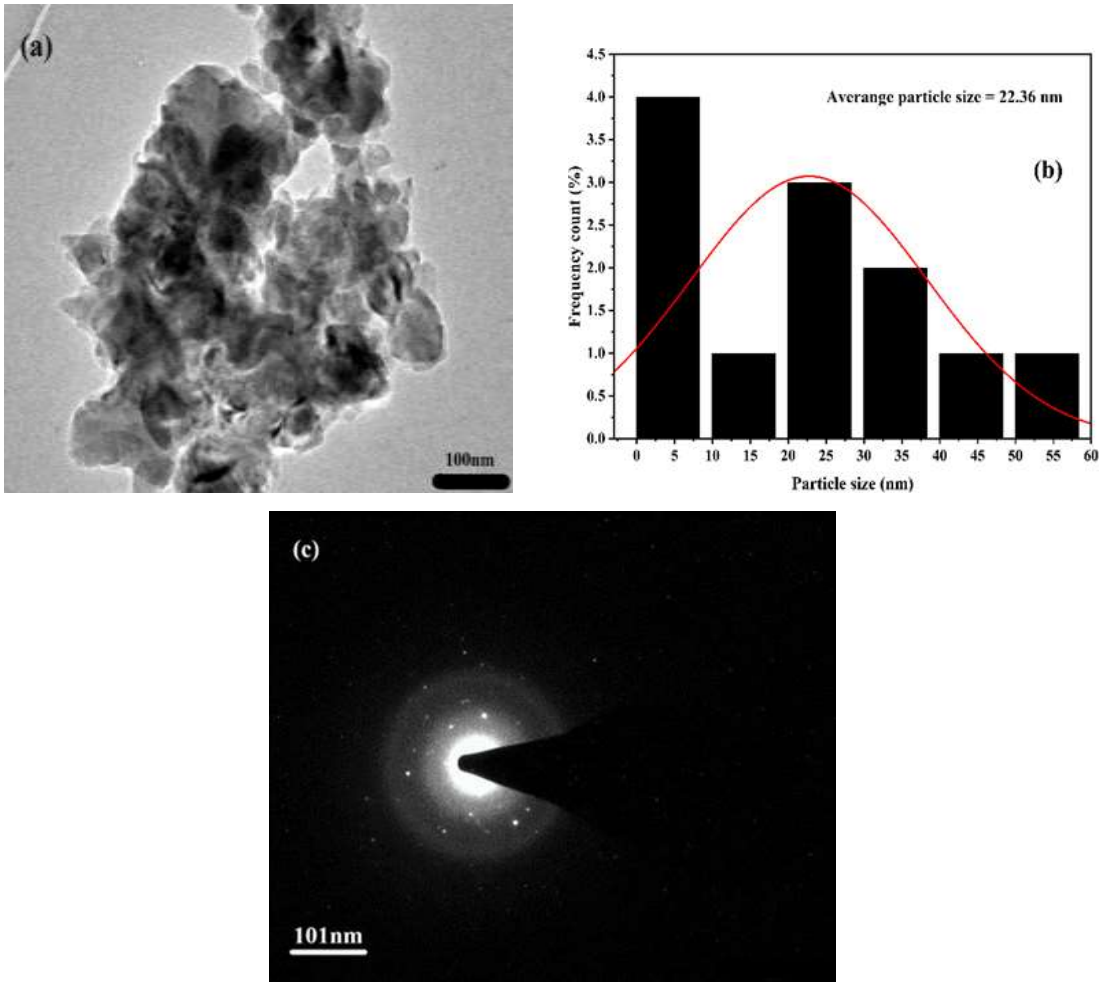

Fig. 3.11: (a) TEM image of doped silica glass-ceramic ZnS nanoparticle and (b) corresponding analysis of the particle size distribution (c) Selected Area Electron Diffraction image displaying the doped silica glass-ceramic ZnS nanoparticle diffraction pattern.

FTIR Spectra

Fig. 3.12 shows the FTIR spectra of Eu^{3+} ions (2 mol%) doped with a fixed amount of ZnS nanoparticle (1 mol %) at various annealing temperatures. The spectra were recorded in the range 500−4000 cm^{-1}. Table 3.4 displays the different peak positions and vibrations that were assigned. There is a lot of water and other organics in the samples in the gel stage. The obtained sample is slowly heated in an electric muffle furnace, which results in the gradual reduction of various chemicals from the gel matrix and helps build a solid glassy network (Dawngliana *et al.*, 2023).

Dips at 802 cm^{-1} are caused by the Zn-S vibration (i.e., the sulfide group), while dips at 1049 cm^{-1} and 1512 cm^{-1} are caused by the stretching of the Si-O-Si. The glass matrix's doped Eu^{3+} ions are a factor in the peaks at about 1049.28 cm^{-1}. Bands at 1651 cm^{-1}, which are C-O vibrational modes, are caused by absorbed CO_2 on the crystal's surface. The hydroxyl group's stretching by OH is what causes the band to be between 2908 cm^{-1} and 3600 cm^{-1}. This band's progressive disappearance during annealing demonstrates how -OH was eliminated through evaporation.

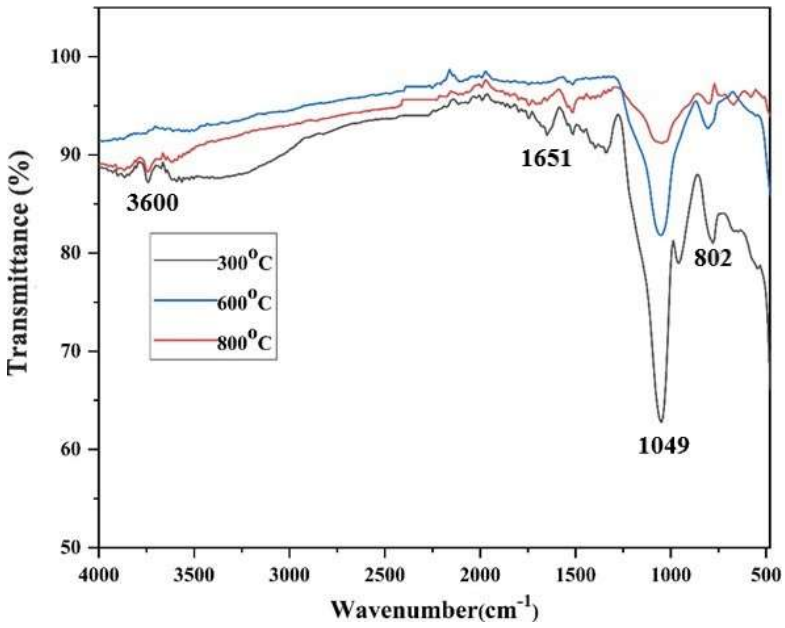

Fig. 3.12: FTIR spectra of Eu^{3+} ions (2.0 mol%) doped ZnS nanoparticle at various annealing temperatures.

Table 3.4: Assignment of FTIR spectra of Eu^{3+} ions doped ZnS nanoparticle peaks in silicaglass matrix

Wavenumber (cm^{-1})	**Assignment**	**Intensity**	**Intensity changed during annealing**
802-956	Zn-S vibration	minor	Intense peak arises up to 600^{o} C, minor peak arises at 800^{o} C
1049-1512	Si-O-Si stretching	intense peak	Gradually decreases at higher temperature
1651	C-O vibrational modes	minor	Disappear at T> 600^{o} C
2908-3600	O-H Stretching	broad	Completely remove at T> 600^{o} C

3.3.2.3 Optical properties as-synthesized of silica glass doped ZnS nanoparticle

Absorption spectra

The UV-Visible absorption spectra of as-synthesized silica glass doped ZnS nanoparticles are depicted in Fig. 3.13(a). The quantum confinement effect of the ZnS nanoparticle is responsible for the strong absorption peak that is seen at about 310 nm, which is slightly blue shifted from the bulk absorption at 340 nm (Sang *et al.*, 2002). Light with a wavelength range of 220-350 nm is efficiently absorbed by ZnS. This absorption peak results from the change from the entire state in the valance band to the electronic state in the conduction band. It can be seen that there are no absorption spectra in the visible range (400 nm−750 nm) (Tauc, 1974). The relation between the absorption coefficients (α) and incident photon energy ($h\nu$) is given by eqn (3.3)

For calculating the direct bandgap value $(\alpha h\nu)^2$ vrs. $h\nu$ is plotted and it is shown in the inset of Fig. 3.13(a) (Chang *et al.*, 2017). By extrapolating the straight portion of the graph on $h\nu$ axis at α=0, the optical bandgaps of the room-temperature as-synthesized ZnS nanoparticle (Tauc, 1974) doped silica-glass ceramic have energy band gap values of 3.49 eV; it is found to decrease by an amount of 0.11 eV when related to the absorption edge of the bulk ZnS (3.60 eV). When it comes to quantum confinement, the band gap energy rises as the particle's size decreases, and quantum

confinement happens when the particle's size equals or falls below the Bohr radius. On the other hand, when the particle size is reduced in doped samples, the band gap shrinks. It is known as the "heavy doping effect" phenomenon. The change in the band gap energy is in line with the measured size of the nanoparticle (Zhang *et al.*, 2018). The quantum confinement effect is responsible for this size-dependent variation in the band gap energy.

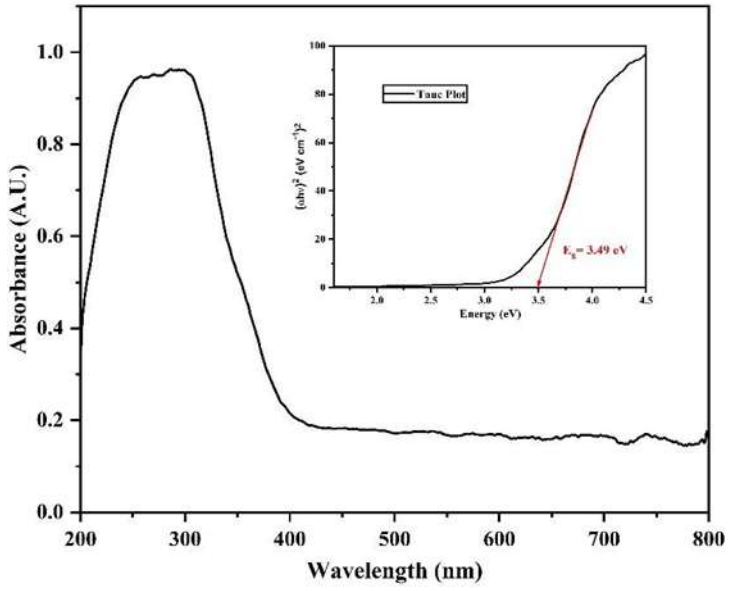

Fig. 3.13(a): UV-VIS absorption spectra and Tauc plot of ZnS nanoparticle doped silica glass- ceramic.

PL spectra

The PL spectra of ZnS nanoparticle-doped silica glass-ceramic excited by a 25 W UV light source at 370 nm in the 450–800 nm wavelength range annealed at 500° C are shown in Fig. 3.13(b). Green luminescence is observed starting at the peak at approximately 543 nm, which is explained by the recombination between the sulfur vacancies (Chang *et al.*, 2017). Because interstitial sulfur ions are larger than zinc ions, interstitial sulfur induces greater strain on the lattice. This strain will result in lower binding energies for electron levels leaving this site (Zhang *et al.*, 2018).

Interstitial sulfur states should therefore be located in the direction of the valence band edge.

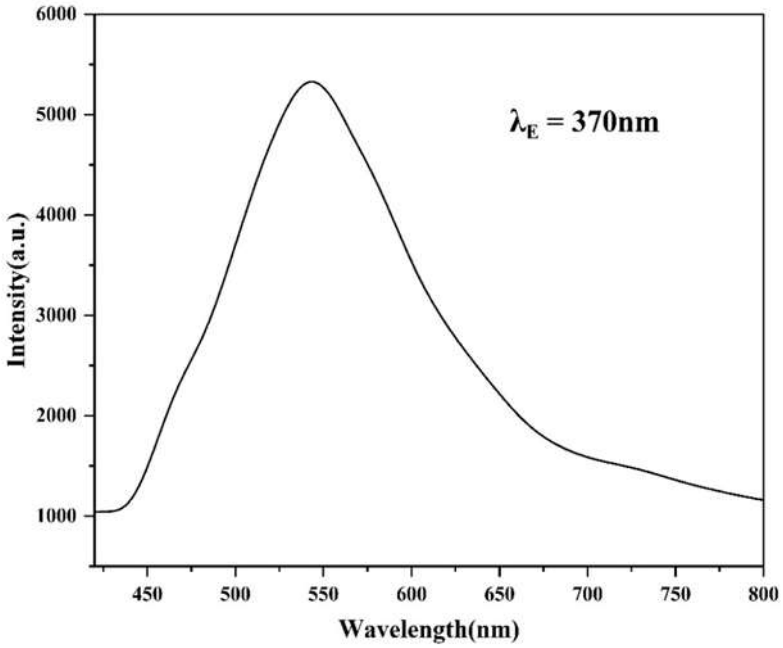

Fig. 3.13(b): PL spectra of silica glass doped with pure ZnS nanoparticles annealed at 500° C.

3.3.2.4 Optical properties of Eu^{3+} ions doped ZnS nanoparticle in silica glass-ceramic.

PL spectra

The PL spectra of different concentrations of Eu^{3+} ions doped with a fixed amount of ZnS (1 mol %) nanoparticle in silica glass-ceramic prepared by sol-gel technique are shown in Fig. 3.14(a), and the corresponding energy level diagram is also depicted in Fig. 3.14(b). The sample is excited by using an UV light source that has a wavelength of 370 nm and a power of 25 W from the ground state $^7F_0$ (j= 0−4) to the excited state $^5D_0$. The PL spectra have five emission bands that correspond to $^5D_0 \rightarrow {}^7F_0$, $^5D_0 \rightarrow {}^7F_1$, $^5D_0 \rightarrow {}^7F_2$, $^5D_0 \rightarrow {}^7F_3$, and $^5D_0 \rightarrow {}^7F_4$ correspondingly at 578 nm, 593 nm, 614 nm, 653 nm and 703 nm. The other four luminescent bands were comparatively lower, with the luminous band's peak at 614 nm being the most

prominent. Comparison of luminous emission $^5D_0 \rightarrow {}^7F_2$ of our reported work with previous results from our laboratory was also highlighted in Table 3.5. All assignments of transition bands are done with lanthanide spectra transition reported by Dieke (Dieke, 1968) and Carnal et al. (Carnall *et al.*, 1968). According to Fig. 3.13(a), the PL intensity rises as dopant concentration does, which can be assigned to the effect of doping. It is well known that doped nanoparticles exhibit increasing emission efficiencies because the majority of their dopant centres are towards the surface rather than the inside. The emission at around 578 nm and 593 nm is associated to $^5D_0 \rightarrow {}^7F_0$ and $^5D_0 \rightarrow {}^7F_1$ transitions which may be assigned to magnetic-dipole allowed transition that obeys the selection rule $\Delta J = 1$, which is independent of the local symmetry (Carnall *et al.*, 1968). It is also seen the $^5D_0 \rightarrow {}^7F_0$ transition was not observed in low concentrations of Eu^{3+} ions. $^5D_0 \rightarrow {}^7F_0$ transition can be used to determine the environment in which the Eu^{3+} ions are bonded (Dawngliana *et al.*, 2023).

The emission bands correspond to $^5D_0 \rightarrow {}^7F_2$ (614 nm), $^5D_0 \rightarrow {}^7F_3$ (653 nm) and $^5D_0 \rightarrow {}^7F_4$ (703 nm), a transition enabled by an electric dipole, and its intensity is hypersensitive to the variation of the bonding environment of the Eu^{3+} ions (Carnall *et al.*, 1968; Yang *et al.*, 2010). The main causes of electric dipole transitions are the lack of a centre of symmetry and the mixing of $4f^5$ orbitals with the opposite parity orbital (Jubera *et al.*, 2003). These transitions appear due to a charge imbalance between Zn^{2+} and Eu^{3+} ions. Significant intensity progression was observed when Eu^{3+} ions doped with ZnS nanoparticles; the emission intensity is maximum for 2 mol% of Eu^{3+} ions while intensity decreases when concentration is 4 mol%. It suggests cluster formation at greater Eu^{3+} ions concentrations, which results in fluorescence quenching. It is also stated that the ratio between that integrated emission intensity of $^5D_0 \rightarrow {}^7F_1$ and $^5D_0 \rightarrow {}^7F_2$ transitions known as the asymmetric ratio $(R/O)^{12}$, can be used as a local crystal field probe to measure the nature of the local Eu^{3+} surroundings (Madkour *et al.*, 2012). Consequently, this ratio represents the extent of distortion from the Eu^{3+} ion local environment's inversion symmetry. The calculated asymmetric values for 0.75 mol%, 2 mol%, and 4 mol% of Eu^{3+} ions are 1.87, 2.23, and 2.14, respectively. This value is extremely small and has no noticeable impact on the direction of the Eu^{3+} R/O. This provides compelling

evidence that the Eu^{3+} ions primarily occupy the lattice site without inversion symmetry (Madkour *et al.*, 2012).

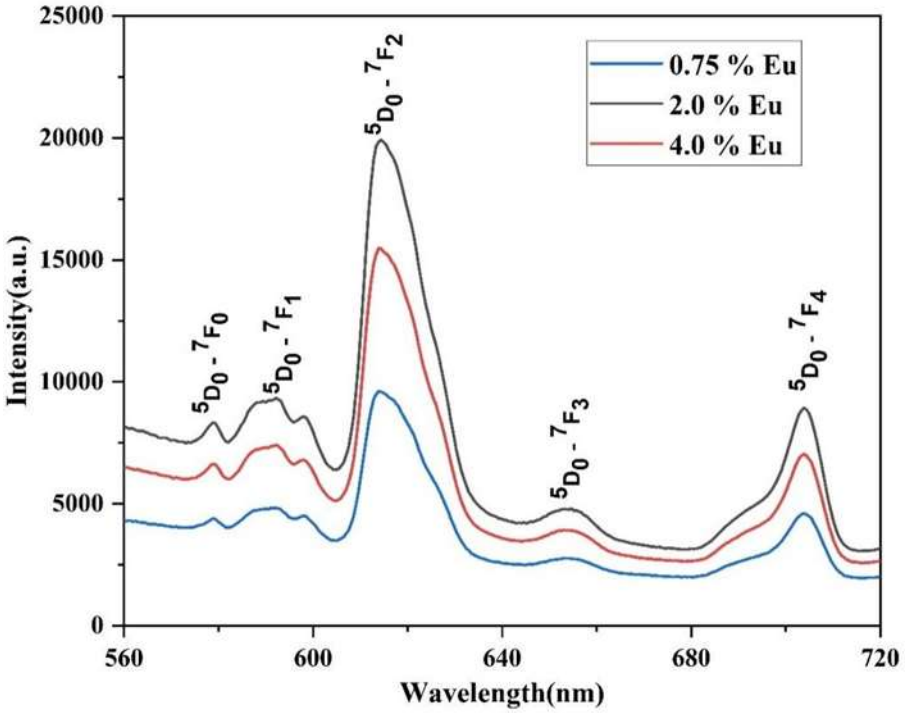

Fig. 3.14(a): PL Spectra of different concentrations of Eu^{3+} ions doped with a fixed concentration of ZnS nanoparticle in silica glass-ceramic.

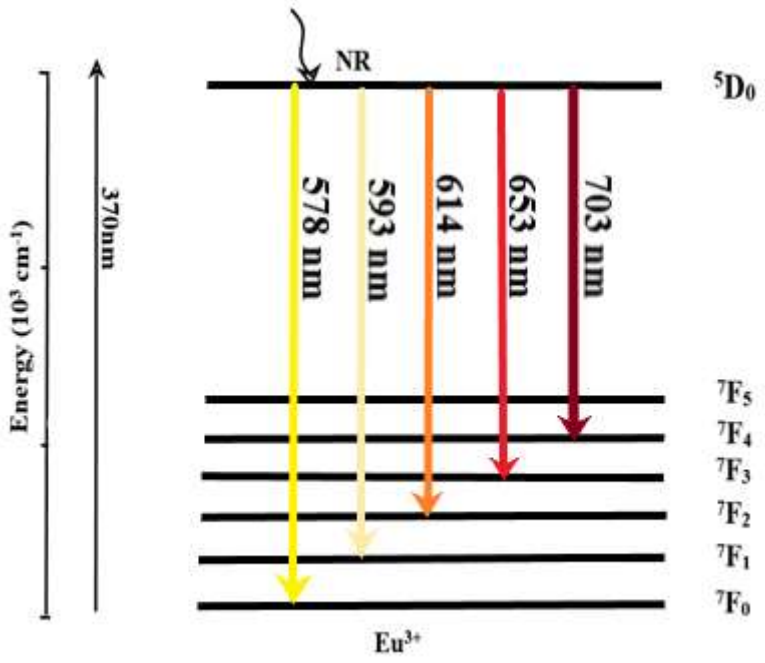

Fig. 3.14(b): Corresponding energy level diagram

Table 3.5: PL intensity comparison of Eu^{3+} ions doped in other nanoparticles.

Nanoparticle	**λ_{ex} (nm)**	**λ_{em} (nm)**	**Intensity (a.u.)**	**Energy state transitions**
Present work (ZnS)	370	614	19912	$^5D_0 \rightarrow {}^7F_2$
Al [16]	370	614	17500	$^5D_0 \rightarrow {}^7F_2$
CdS [18]	350	614	16000	$^5D_0 \rightarrow {}^7F_2$

Impact of Annealing Temperature on PL Spectra

The PL spectra of Eu^{3+} ions (2.0%) doped with fixed ZnS nanoparticles in silica glass ceramic annealing at different temperatures (100, 300, 500 and 900º C) are shown in Fig. 3.15(a) and Fig. 3.15(b) shows that the broad emission peak $^5D_0 \rightarrow {}^7F_2$ intensity vs annealing temperature, there is an exponential increase with an annealing. As sol-gel is a wet chemical process, a large amount of hydroxyl groups is present that which is little intensity was observed after being annealed at 100-300º C. The figure illustrates how a higher annealing temperature eliminates the hydroxyl groups, dramatically enhancing PL intensity. Removal of the hydroxyl group also decreases the weight of the sample, thereby causing densification of the samples and

closing the pores present, which preserve them from atmospheric moisture reabsorption (Fanai *et al.*, 2019).

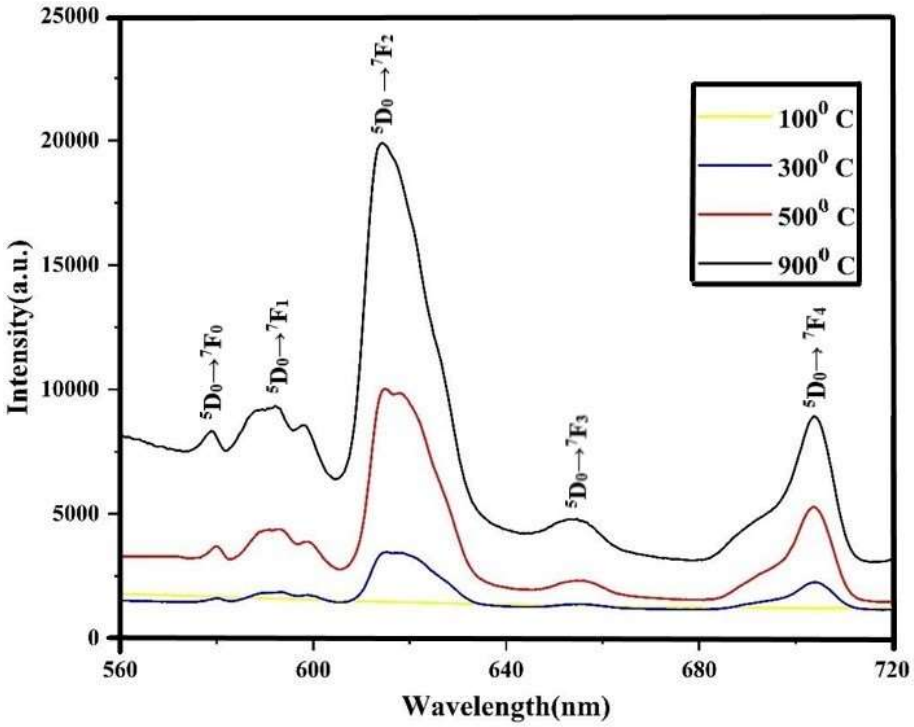

Fig. 3.15(a): PL Spectra of Eu^{3+} ions doped ZnS nanoparticle in silica glass at various annealing temperature.

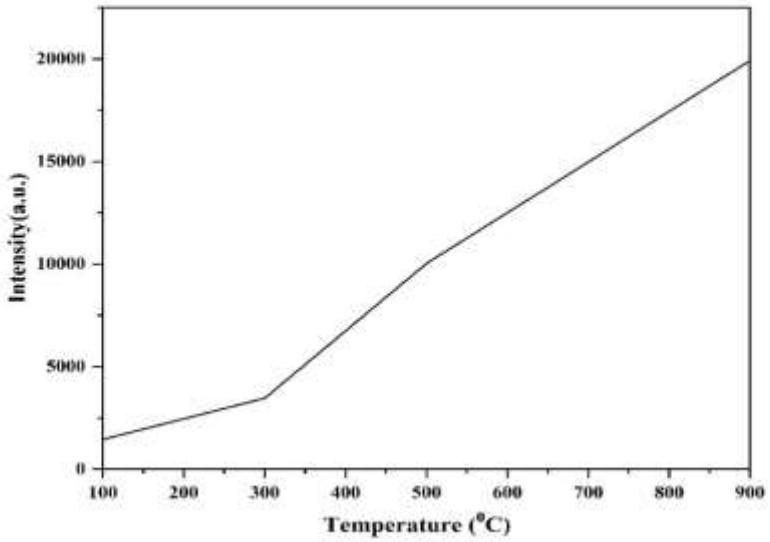

Fig. 3.15(b): Annealing temperature Vs PL intensity of $^5D_0 \rightarrow {}^7F_2$ transition.

Color tunability and photometric analysis

Examining the color coordinates shown on a conventional chromaticity diagram is necessary to determine the actual nature of the material's color emissions. A tool used to measure the tunability of the emission wavelength and the intensity variation in the emission band is the CIE 1931 (Commission International d'Eclairage) diagram. It is a universal method of representing every color by combining three primary colours. Fig. 3.14 shows the CIE Chromaticity diagrams of ZnS: Eu^{3+} ions that vary with the Eu^{3+} ions concentrations. The CIE Chromaticity coordinates of Eu^{3+} ions were derived based on their corresponding PL spectra at 370 nm excitation. The photoluminescence emission of different concentrations of Eu^{3+} ions doped with a fixed concentration of ZnS nanoparticles was illustrated using CIE 1931 chromaticity. The following equations (3.4), (3.5), and (3.6) are used to derive the chromaticity coordinates from the tri-stimulus values (Wang *et al.*, 2010).

The CIE coordinates (x, y) and CCT values for the studied samples were presented in Table 3.6 which falls within the white region, and the changing concentration does not cause significant changes in the color coordinates. In this studied glass, white light with minimal blue component is achieved with UV excitation in the 370 nm wavelength.

It is possible to compute the phosphors' correlated colour temperature (CCT) to see if they are suitable for use as a practical white light source. The colour appearance of the light output by a light source is specified by its CCT (in Kelvin), which compares the colour of the light to that of a reference light source at a particular temperature. The CCT value, a measurement of the overall warmth or coolness of the look, is useful when designing illuminating devices (Yoon *et al.*, 2018). Using the McCamy empirical formula, the relevant CCT values can be determined from the CIE chromaticity coordinates (McCamy, 1992).

$$\mathrm{CCT} = -437\mathrm{n}^3 + 3601\mathrm{n}^2 - 6861\mathrm{n} + 5514.31 \qquad (3.7)$$

Where $n = (x - x_c)\,(y - y_c)$ is the inverse slop line, and $x_c = 0.3320$ and $y_c = 0.1858$ is the epicentre of the chromaticity coordinates. The CCT values of x = 0.2897, 0.2915, and 0.2887 are calculated to be 13031, 12138, and 13539 respectively. Generally, CCT values less than 5000 K imply warm white light used for home appliances, while those above 5000 K suggest cool white light utilized for

commercial lighting purposes (Ambast *et al.*, 2014). The result indicates that the studied ZnS: Eu silica glass is quite suitable for a cool white light source.

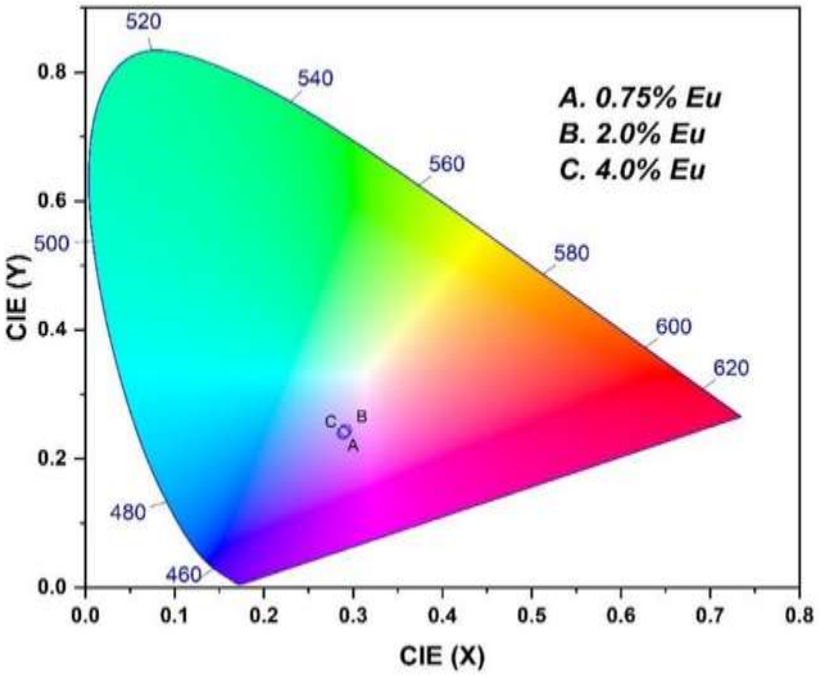

Fig. 3.16: CIE Chromaticity of Eu^{3+} ions doped fixed concentration of ZnS nanoparticle in silica glass.

Table 3.6: CIE chromaticity coordinates of different concentrations of Eu^{3+} ions doped ZnSnanoparticle and CCT in silica glass.

ZnS: *x* Eu^{3+}	**X**	**Y**	**CCT**
0.75 mol %	0.2897	0.2413	13031
2.0 mol %	0.2915	0.2443	12138
4.0 mol %	0.2887	0.2399	13539

3.4 Conclusions

Terbium doped glass

Different concentrations of ZnS nanoparticles doped with a fixed concentration of Tb^{3+} ions and ZnS doped silica-ceramic have been successfully synthesized utilizing the sol-gel method. X-ray diffraction (XRD) and selected area electron diffraction (SAED) studies confirm the formation of hexagonal polycrystalline structure. Transmission electron microscopy (TEM) analyses

revealed that variation in size of the particles lies between 10 and 50 nm. FTIR spectra reveals the removal of O-H vibrations at higher temperatures, which helps in creating the strong glassy network glass matrix. The band gap energy of the as-synthesized nanocomposite glass was 3.18 eV with a green light emission. The PL spectra reveal that there are four strong emission peaks at 489nm, 542nm, 585nm, 622nm which corresponds to $^5D_4$-$^7F_6$, $^5D_4$-$^7F_5$, $^5D_4$-$^7F_4$, $^5D_4$-$^7F_3$ transitions, respectively. The PL increases as the concentration of dopant increases. The broad peak $^5D_4$-$^7F_5$ emission exponentially increased after 600^{o}C onwards. The CIE chromaticity evident that the tunability of color from blue-green to yellowish green region as ZnS concentration increases. Thus, the presented results may be very useful for the use of green laser sources.

Europium doped glass

ZnS nanoparticle doped and ZnS: Eu^{3+} ions co-doped with different concentrations of Eu^{3+} ions in silica glass-ceramic have been synthesized successfully using a sol-gel technique. The formation of the blende structure and a hexagonal polycrystalline phase of ZnS is confirmed by studies using SAED and XRD. Analysis using TEM showed that the particles' sizes vary from 10 to 50 nm. FTIR spectra have confirmed the elimination of the OH-group and disappearance of ZnS characteristics at higher temperatures. Diffuse reflectance spectra were calculated by using UV–Visible Spectrophotometer. And also calculated the band gap energy of the as-synthesized sample by using the Kubelka-theory, it is approximately 3.49 eV with a pure green emission. Photoluminescence spectra reveal that there are five strong emission peaks at 578 nm, 593 nm, 614 nm, 653 nm, and 703 nm which corresponds to $^5D_0 \rightarrow ^7F_0$, $^5D_0 \rightarrow ^7F_1$, $^5D_0 \rightarrow ^7F_2$, $^5D_0 \rightarrow ^7F_3$ and $^5D_0 \rightarrow ^7F_4$ respectively. The CIE colour chromaticity and CCT reveal that the studied glass can be used for producing cool white light for commercial lighting purposes.

REFERENCES

Annapurna Devi Ch.B., Swapna K., Mahamuda S.K., Venkateswarla M., Prasad M.V.V.K.S., Siva Rama Krishna Reddy K., Nisha Deopa, Rao A.S. (2019) Spectroscopic studies and lasing potentialities of Sm^{3+} ions doped single alkali and mixed alkali fluoro tungsten tellurite glasses. *Opt. Laser Technol.* **111**:176-183. doi: https://doi.org/10.1016/j.optlastec.2018.09.051

Yasi J., Fusong J., Fuxi G. (1982) Optical and other physical properties of Al $(PO_3)_3$-containing fluorophosphate glasses. *J. Phys.* **43**:315-318. doi: 10.1051/jphyscol:1982958

Haralampieva A., Lozanova I.S., Dimitrov V. (2012) Optical properties and structure of Bao-V_2O_5 and Fe_2O_3-Bao-V_2O_5 glasses. *J. Chem. Technol. Metallurgy* **47**:392-397.

Zhao, J.G.; Zhang, H.H. (2012) Hydrothermal synthesis and characterization of ZnS hierarchical microspheres. *Superlatt. Microstruct.* **51**:663–667. http://dx.doi.org/10.1016/j.spmi.2012.02.004

Zafar Hussain Ibupoto, Kimleang Khun, Xianjie Liu, Magnus Willander (2013) Hydrothermal Synthesis of Nanoclusters of ZnS Comprised on Nanowires. *Nanomaterials* **3:**564-571. https://doi.org/10.3390%2Fnano3030564

Lima S. A. M., Davolos M. R. (2007) Low-voltage electroluminescence of europium in zinc oxide thin films. *Appl. Phys. Lett.* **900**:23503. doi: http://dx.doi.org/10.1063/1.2431566

Tiwary C.S., Kumbhakar P., Mitra A.K., Chattopadhyay K (2009) Synthesis of wurtzite-phase ZnS nanocrystal and its optical properties. *J. Lumin.* **129**:1366-1370. doi: https://doi.org/10.1016/j.jlumin.2009.07.004

Dawngliana KMS, Fanai A.L., Rai S. (2023) Structural and Spectroscopic Properties of Eu^{3+} ions in Alumino-Silicate Glass. *Ind. J. Pure Appl. Phy.* **61**:182-189. doi: https://doi.org/10.56042/ijpap.v61i3.71028

Wenbin Sang, Yongbiao Qian, Jiahua Min, Dongmei Li, Lingling Wang, Weimin Shi, Liu Yinfeng (2002) Microstructural and Optical properties of ZnS: Cu nanocrystals prepared by an ion complex transformation method. *Solid State Comm.* **121**: 475-478. doi: https://doi.org/10.1016/S0038-1098(01)00518-X

J. Tauc (1974) Amorphous and Liquid Semiconductors, Plenum, New York, USA.

Tiwary C.S., Kumbhakar P., Mitra A.K., Chattophadhyay K. (2009) Synthesis of wurtzite-phase of ZnS nanocrystal and its optical properties. *J. Lumin.* **129**: 1366-1370. doi: https://doi.org/10.1016/j.jlumin.2009.07.004

Yan Zhang, Jiayue Xu, BoBo Yang, Qinzhi Cui, Tian Tian (2018) Luminescence properties and energy migration mechanism of Eu^{3+} activated $Bi_4Si_3O_{12}$ as a potential phosphor for white LEDs. *Mater. Res. Express* **5** 026202: doi: 10.1088/2053- 1591/aaab8a

Dieke G.H. (1968) Spectroscopy & Energy Levels of Rare Earth Compounds, Inter Science, New York.

Carnall W.T., Fields P.R., Rajnak K. (1968) Spectral Intensities of the Trivalent Lanthanides and Actinides in Solution. II. Pm^{3+}, Sm^{3+}, Eu^{3+}, Gd^{3+}, $Tb^{3+,}$ Dy^{3+}, and Ho^{3+}. *J. Chem. Phys.* **49**:4412-4428. doi: https://doi.org/10.1063/1.1669892

Fanai A.L., Khan U., Rai S. (2019) Luminescence enhancement of Pr^{3+} doped sol-gel silica glass as a result of Al^{3+} co-doping. *J. Non-Cryst. Solids* **503–504**:89-93. doi: https://doi.org/10.1016/j.jnoncrysol.2018.09.027

Jubera V, Chaminade J.P, Garcia A, Guillen F, Fouassier C (2003) Luminescent properties of Eu^{3+}-activated lithium rare earth borates and oxyborates. *J. Lumin.* **101**: 1- 10. doi: https://doi.org/10.1016/S0022-2313(02)00335-6

Liping Wang, Xudong Xu, Xin Yuan (2010) Preparation and photoluminescent properties of doped nanoparticles of ZnS by solid-state reaction. *J. Lumin.* **130**: 137–140. doi: https://doi.org/10.1016/j.jlumin.2009.07.036

Yoon S.J., Pi J.W., Park K (2018) Structural and photoluminescence properties of solution combustion-processed novel ZrO_2 doped with Eu^{3+} and Al^{3+}. *Dyes and Pigments* **150**: 231-240. doi: https://doi.org/10.1016/j.dyepig.2017.12.012

McCamy C S (1992) Correlated color temperature as an explicit function of chromaticity coordinates. *Color Res. Appl.* **17**:142. doi: https://doi.org/10.1002/col.5080170211

Ambast A K, Goutam J, Som S, Sharma S K (2014) $Ca_{1-x-y}D_{yx}K_y WO_4$: A novel near UV converting phosphor for white light emitting diode. *Spectrochim Acta A* **122**:93-99. doi: https://doi.org/10.1016/j.saa.2013.11.032

Metwally Madkour, Yasser Abdelmonem, Umair Yaqub Qazi, Rahat Javaid and S. Vadivel (2021) Efficient Cr (VI) photoreduction under natural solar irradiation using a novel step-scheme $ZnS/SnIn_4S_8$ nanoheterostructured photocatalysts. *RSC Adv.* **11**: 29433. doi: 10.1039/d1ra04649

CHAPTER-4

SPECTROSCOPIC STUDIES OF SM^{3+}, PR^{3+} DOPED ZNS NANOPARTICLES AND RADIATION INDUCED DEFECTS IN SM^{3+} DOPED SILICATE GLASS

This chapter focuses on the physical, structural, and spectroscopic studies of ZnS nanoparticles doped with Sm^{3+} and Pr^{3+} in a silica glass matrix and the effect of γ- ray irradiation on the optical properties of Sm^{3+} doped silica glass.

4.1. Abstract

This research intends to study the structural and spectroscopic properties of Sm^{3+} doped with ZnS nanoparticles in silica glass. The research adopted the sol-gel technique for preparing the sample. The physical property of the studied glass sample is examined by different characterization techniques such as Abbe refractometer, X-ray Diffraction (XRD) and Transmission Electron Microscopy (TEM) and Photoluminescence (PL) spectroscopy. XRD studies confirmed the formation of glassy amorphous nature and TEM studies confirmed that the studied nanoparticles are polycrystalline in nature, with a particle size lying between 10 and 50 nm after annealing at 300 °C. The PL spectra have three emission bands that correspond to $^4G_{5/2}\rightarrow{}^6H_{5/2}$, $^4G_{5/2}\rightarrow{}^6H_{7/2}$ and $^4G_{5/2}\rightarrow{}^6H_{9/2}$ correspondingly at 565 nm, 603 nm and 650 nm with the most prominent bands in the orange-red region. Consequently, the doped glass can be utilized for producing a nearly pure white hue when triggered at 370 nm.

Spectroscopic properties of different concentrations of Pr^{3+} doped ZnS nanoparticles in silica glass matrix have been prepared by the sol-gel method. The physical properties were calculated. The structural properties were characterized by using Fourier Transform Infrared (FTIR), X-ray diffraction (XRD) and Transmission electron microscopy (TEM) spectroscopy, respectively. FTIR spectra were carried out and the formations of NBO and the elimination of OH groups are confirmed. XRD spectra confirmed the formation of glassy amorphous nature. TEM spectra revealed that the particle size lies between 10 and 50 nm after annealing at 300 °C and SAED image confirmed that the studied glass is polycrystalline in nature. From

the visible region's absorption spectrum, the Judd-Ofelt parameters Ω_2, Ω_4, and Ω_6 were determined, and these parameters followed the trend $\Omega_6 > \Omega_4 > \Omega_2$. For the fluorescence level of Pr^{3+} in these glasses, different radiative properties such as radiative transition probability (A_R), branching ratio, transition probability, and radiative lifetime have been evaluated from this theory. Photoluminescence emission was carried out in the VIS-NIR region with stark splitting of $^3H_4$ levels. According to the CIE chromaticity, this glass can produce green light and be helpful for laser applications in the visible spectrum. It may be used as optical amplifier devices, as indicated by the values of the Figure of Merit (FOM).

Sm^{3+} doped silica glass prepared by the sol-gel technique was investigated with before irradiation and gamma irradiation in order to understand the effect on the glass composition. We also investigated the optical properties of Sm^{3+} ions in sol-gel SiO_2 glass. Photoluminescence (PL) spectra reveal that valency of Sm^{3+} was reduced to Sm^{2+}, Sm^{3+} character was regained after 148 hours (1 week) of irradiation and Sm^{2+} existence was highest after 72 hours of gamma irradiation when the sample is kept in a dark room at room temperature. Changing the valency of Sm^{3+} to Sm^{2+} was time dependent. This investigation shows the co-existence of Sm^{3+} and Sm^{2+} which needed higher energy to trigger it out; it is also evidence that the 10 Gy of gamma was an efficient dose for trigging out the Sm^{2+} nature. FTIR spectra reveals that no significant changes were observed in the composition of the glass matrix after gamma irradiation.

4.2 Experimental

The following materials were purchased from Sigma-Aldrich: distilled water, tetraethyl orthosilicate (TEOS, 99.9%), methanol (99.9%), praseodymium (III) nitrate hexahydrate (99.9%), samarium (III) nitrate hexahydrate, zinc sulphide (99.9%) and HNO_3. Without additional purification, all chemicals and solvents were utilized directly. Sample preparation followed the mechanism highlighted in Chapter-2.

The glass sample under study was coated with 1-bromonaphthalene ($C_{10}H_7Br$) as an adhesive coating, and its refractive index was determined using an Abbe refractometer. Using xylene (C_8H_{10}) as an immersion liquid, the density of the

solid glass sample under study was calculated using the Archimedes principle. PL spectra of the glass samples were recorded using an iHR320 imaging spectrometer using Syner JYTM software from Horiba Scientific by using the excitation wavelength of a diode laser, λ_{ex} = 450 nm. FTIR spectra were recorded by IRAffinity-1S (SHI-MADZU). The crystal structure was analyzed using X-ray Diffractometer (Panalytical Empyrean) equipped with a Cu-Kα radiation source. Additionally, using FEI Tecnai high-resolution transmission electron microscopy (HR-TEM) with a 300 kV acceleration voltage, the particulate nanostructure patterns of the nano-composites were investigated. The sample was irradiated at room temperature using the Equinox80 located at the Mizoram State Cancer Institute, Aizawl, Mizoram. ^{60}Co isotope is the radiation source. The sample was irradiated at 80 cm distance from the isotope at 10 Gray (Gy). The ionisation or energy deposited by ^{60}Co gamma ray is measured by Gy which is the energy in Joule (J) deposited in a mass of 1 kg of matter. The 80 cm is the distance at which the Gy measurement is performed. The Gy measured at the time of the experiment was 2.52 Gy/min, and it took 3.96 minutes to achieve 10 Gy.

4.3. Results and Discussions

4.3.1 Samarium doped glass

4.3.1.1 Physical properties

The two measured values of density and retractive indices of the studied sample are used for calculating another physical property such as Average molecular weight (M_T), Ion's concentration (N_i), Dielectric constant (ε_d), Optical dielectric constant (ε_d-1), Molar volume (V_m), Reflection Losses (R_L), Molar Refractivity (R_M), Energy gap (E_g), Polaron Radius (R_p), Interionic distance (R_i), Field strength (F_s), Molar polarizability (α_m) and Metallization Criterion (M_c) by using appropriate expressions (Annapurna Devi *et al*., 2019) and represented in Table 4.1. The non-linear dynamics of the materials are determined by the sample's electronic polarizability (Dawngliana *et al.*, 2022). Exposure to intense light causes the material to exhibit electronic polarizability. Volt Lorentz-Lorentz theory (Fusong *et al.*, 2012) is utilized for deriving electronic polarizability (α_e) as follows:

$$\frac{(n^2-1)}{(n^2+1)} V_m = \frac{4}{3\pi} N\alpha_e \qquad (4.1)$$

where *n* is refractive index, V_m is molar volume, and N is Avogadro's number.

Table 4.1: Various physical properties of Sm^{3+} ions doped with a fixed amount of ZnS nanoparticle.

Physical properties	**Sm (2.0 %)**
Refractive index (ni)	2.353
Density (ρ) (g/cm^3)	2.203
Thickness (Zt)	0.171
Average molecular weight M_T (g)	68.14
Ion's concentration ($N_i \times 10^{20}$)	3.89
Dielectric constant (ε_d)	5.54
Optical dielectric constant (ε_d-1)	4.54
Molar volume (V_m) (cm^3/mol)	30.93
Reflection Losses (R_L)	0.163
Molar Refractivity (R_M)	21.47
Energy gap (E_g)	1.86
Polaron Radius ($R_p \times 10^{-8}$) (cm^{-3})	2.23
Interionic distance ($R_i \times 10^{-7}$) (cm^{-3})	0.856
Electronic polarizability ($\alpha_e \times 10^{21}$)	2.38
Field strength ($F_s \times 10^{13}$)	34.4
Molar polarizability (α_m)	8.52
Metallization Criterion (M_c)	0.306

4.3.1.2 Structural properties

XRD Study

Fig. 4.1 shows the XRD spectra of Sm^{3+} doped ZnS nanoparticles in silica glass matrix annealed at 300 °C. It is observed that the distinct broad hollow peak is formed rather than intense crystalline peaks, which established the glassy amorphous nature of the glass sample. The intense peak at $2\theta = 23^0$ is attributed to the amorphous nature of silica glass (Dawngliana *et al.*, 2022). ZnS nanoparticle show trigonal structure even at room temperature (Tiwary *et al.*, 2009) while doped samples only show amorphous nature even when the annealing temperature is 300^0 C. For the doped sample from 500^oC onwards, crystalline peaks can be seen, which were reported in our previous result.

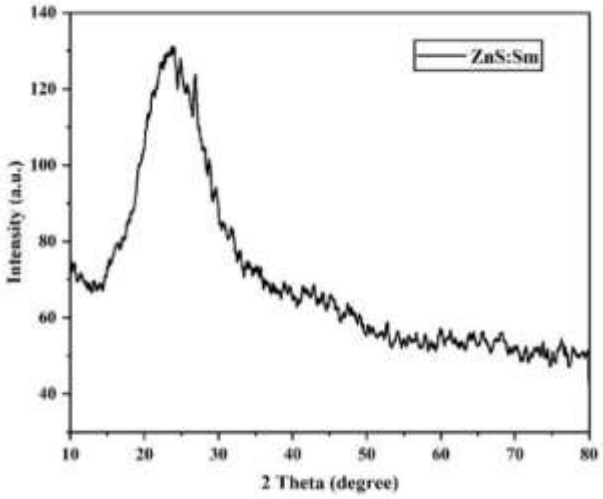

Fig 4.1: XRD spectra of Sm doped ZnS nanoparticle annealed at 300^0 C.

TEM Study

The TEM micrographs of the studied doped sample were recorded to study the presence of Sm as well as the confirmation of ZnS in doped SiO_2 matrix, as shown in Fig 4.2 (a-b). It is feasible to state that the range of particle sizes after annealing at 300°C is between 10 and 50 nm as studied through ImageJ software. The investigated ZnS nanoparticles are polycrystalline in nature, as shown by the SAED image, which displays a set of ring structures as depicted in Fig. 4.2(b).

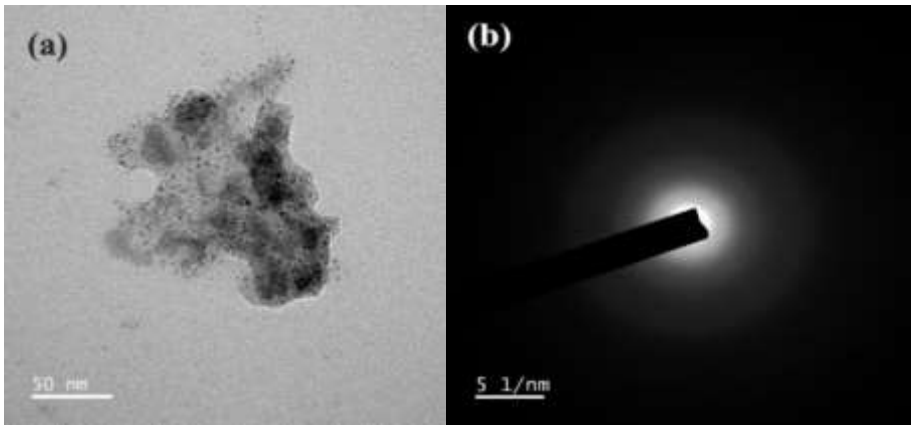

Fig 4.2: (a) TEM image of Sm^{3+} doped ZnS nanoparticle in silica glass matrix (b) Selected Area Electron Diffraction image.

4.3.1.3 Optical properties

PL Spectra

The PL spectra of Sm^{3+} ions doped with a fixed amount of ZnS (1 mol %) nanoparticle in silica glass matrix prepared by the sol-gel technique annealed at 900 °C are shown in Fig. 4.3. The PL spectra have three emission bands that correspond to $^4G_{5/2} \rightarrow {}^6H_{5/2}$, $^4G_{5/2} \rightarrow {}^6H_{7/2}$ and $^4G_{5/2} \rightarrow {}^6H_{9/2}$ correspondingly at 565 nm, 603 nm and 650 nm. The luminous band's peak at 650 nm being the most prominent. The most prominent emission peaks were observed in the green and orange-red regions. All assignments of a transition bands are done with lanthanide spectra transition reported by Dieke (Dieke, 1968) and Carnal et al (Carnall *et al.*, 1968). The peak at 565 nm results from transition between a magnetic field ($\Delta J = 0$ and ± 1) and an electric field ($\Delta J = \pm 2$). The peak observed at 603 nm satisfies the selection rule for magnetic dipole transition; it is ascribed to the transitions between partially electric and partially magnetic dipoles, with the electric dipole transition being more prevalent. While the peak at 650 nm results from an electric dipole transition.

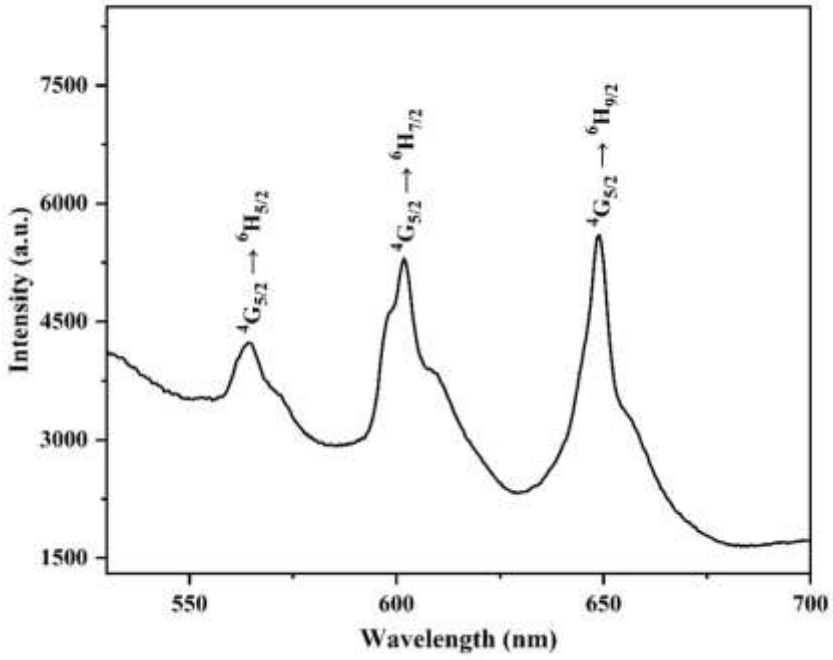

Fig 4.3: PL Spectra of Sm^{3+} ions doped with a fixed concentration of ZnS nanoparticle in silica glass matrix.

CIE Chromaticity

Examining the color coordinates shown on a traditional chromaticity diagram is necessary to determine the actual nature of the material's color emissions. A tool for measuring the tunability of the emission wavelength and the intensity variation in the emission band is the CIE 1931 (Commission International d'Eclairage) diagram. It is a universal method of representing every color by combining three primary colours. Fig. 4.4 shows the CIE Chromaticity diagrams of ZnS doped Sm^{3+} ions in the silica glass matrix. This diagram demonstrated that the studied samples emit a nearly pure white hue when triggered at 370 nm. The following equations are used to derive the chromaticity coordinates from the tri-stimulus values (Tiwary *et al.*, 2009).

$$x = \frac{X}{X+Y+Z} \tag{4.2}$$

$$y = \frac{Y}{X+Y+Z} \tag{4.3}$$

$$z = \frac{Z}{X+Y+Z} = 1 - x - y \tag{4.4}$$

It is also possible to compute the phosphors' correlated colour temperature (CCT) to see if they are suitable for use as a practical white light source. The colour appearance of the light output by a light source is specified by its CCT (in Kelvin), which compares the colour of the light to that of a reference light source at a particular temperature. The CCT value, a measurement of the overall warmth or coolness of the look, is useful when designing illuminating devices (Yoon, 2018). Using the McCamy empirical formula, the relevant CCT values can be determined from the CIE chromaticity coordinates (McCamy, 1992)

$$CCT = -437n^3 + 3601n^2 - 6861n + 5514.31 \tag{4.5}$$

Where, $n = (x - x_c)(y - y_c)$ is the inverse slop line and $x_c = 0.3320$ and $y_c = 0.1858$ is the epicentre of the chromaticity coordinates. The colour coordinates for the studied glass sample were x= 0.297 and y= 0.333 which falls within the white light region, and the corresponding CCT value was 7358 K. Generally, CCT values less than 5000 K imply warm white light used for home appliances, while those above 5000 K suggest cool white light utilized for commercial lighting purposes (Ambast *et al.*, 2014). The result indicates that the studied glass sample is quite suitable for making a nearly pure white hue light source for commercial lighting purposes.

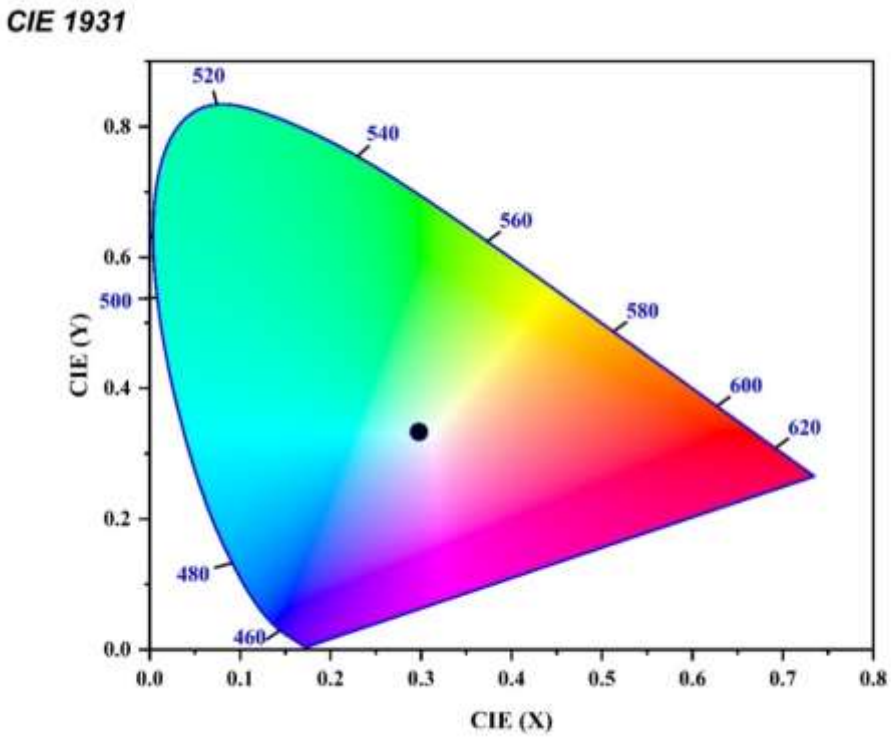

Fig 4.4: CIE Chromaticity of Sm^{3+} ions doped fixed concentration of ZnS nanoparticle in silica glass matrix.

4.3.2 Praseodymium doped glass

4.3.2.1 Physical properties

The density of different concentrations of Pr^{3+} doped with a fixed amount of ZnS nanoparticle was measured by the Archimedes principle, where the studied glass sample was immersed in xylene (Dawngliana *et al.*, 2022). Glass density is an intrinsic property that sheds light on the material's short-range structure and is strongly correlated with its composition (Mohan *et al.*, 2018). Abbe's refractometer was utilized for measuring the refractive index. By using these two measured values, another physical property such as Average molecular weight (M_T), Ion's concentration (N_i), Dielectric constant (ε_d), Optical dielectric constant (ε_d-1), Molar volume (V_m), Reflection Losses (R_L), Molar Refractivity (R_M), Energy gap (E_g), Polaron Radius (Rp), Interionic distance (R_i), Field strength (F_s), Molar polarizability (α_m) and Metallization Criterion (M_c) were calculated by using appropriate

expression (Annapurna Devi *et al.*, 2019) and represented in Table 4.2. The value of molar volume is maximum for 5.0 mol% and minimum for 1.0 mol%. For this specific glass composition, the maximum molar volume of 5.0 mol% indicates an increase in bond length and the interatomic spacing. An increase in the force constant and a shorter bond length of the bonds inside the network can account for the lower value of the molar volume for 1.0 mol%. The electronic polarizability (α_e) which controls the non-linear dynamic of the materials, was derived by using Volt Lorentz-Lorentz theory (Yasi *et al.*, 2012) as follows eqn. (4.1).

Table 4.2: Various physical properties of different concentrations of Pr^{3+} doped ZnS nanoparticle in silica glass matrix.

Physical properties	**1 mol% ZnS: *x* mol% Pr**		
	***x* = 1 %**	***x* = 3%**	***x* = 5%**
Refractive index (n_i)	2.09	2.11	2.41
Density (ρ) (g/cm^3)	2.09	2.12	2.20
Thickness (Z_t)	0.181	0.183	0.185
Average molecular weight M_T (g)	64.2	71.7	79.2
Ion's concentration ($N_i \times 10^{20}$)	1.96	5.33	8.38
Dielectric constant (ε_d)	4.37	4.46	5.81
Optical dielectric constant (ε_d-1)	3.37	3.46	4.81
Molar volume (V_m) (cm^3/mol)	30.67	33.88	35.92
Reflection Losses (R_L)	0.124	0.128	0.171
Molar Refractivity (R_M)	19.25	21.47	25.37
Energy gap (E_g)	2.77	2.68	1.72
Polaron Radius ($Rp \times 10^{-8}$) (cm^{-3})	0.17	0.46	0.73
Interionic distance ($R_i \times 10^{-7}$) (cm^{-3})	1.69	0.62	0.40
Electronic polarizability ($\alpha_e \times 10^{21}$)	3.04	3.16	5.33
Field strength ($F_s \times 10^{13}$)	181	183	185
Molar polarizability (α_m)	7.64	8.52	10.07
Metallization Criterion (M_c)	0.37	0.36	0.29

4.3.2.2 Structural characterization

FTIR spectral analysis

The FTIR spectra of ZnS: Pr (3 mol %) annealed at various temperatures in the range 400-4000 cm^{-1} were carried out to examine the composition and quality of the sample as shown in Fig. 4.5. The samples include a lot of water and other organics during the gel stage. The chemicals progressively escape from the matrix after heating the sample in a muffle furnace, forming a hard glassy network. Bands

noticed at 445 cm^{-1} and 794 cm^{-1} are due to Zn-S vibration (Devi *et al.*, 2019) (i.e., corresponding to sulfide group); bands at 1049 cm^{-1}, 1509 cm^{-1}, 1651 cm^{-1} are due to Si-O-Si stretching. Bands at 1751 cm^{-1} correspond to C-O vibrational modes that arise from absorbed CO_2 on the surface of the crystal. The bands around 3618 - 3749 cm^{-1} are due to the OH stretching of the hydroxyl group. This band gradually disappears as the temperature rises, indicating that –OH has been removed through evaporation.

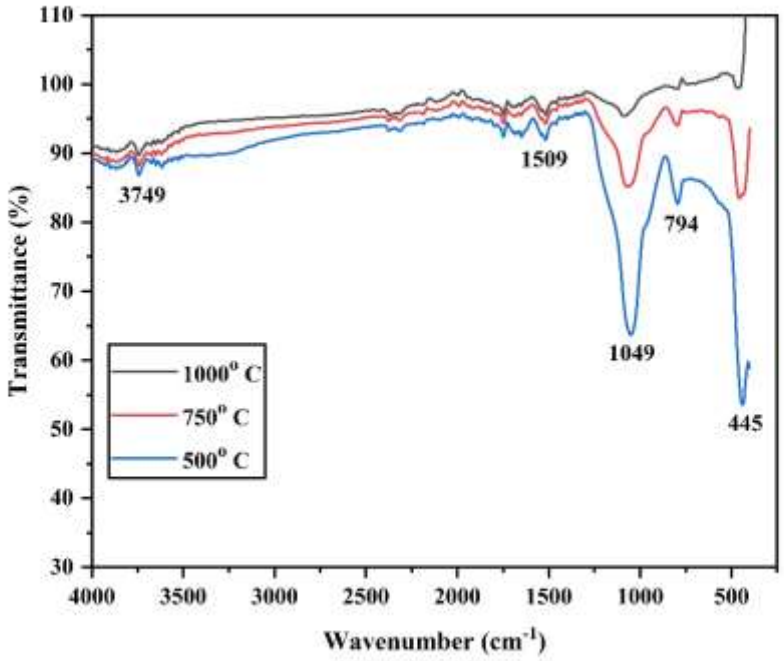

Fig. 4.5: The FTIR spectra.

XRD Study

Fig. 4.6 shows the XRD spectra of different concentrations of Pr doped ZnS nanoparticles in silica glass matrix annealed at 300^0 C. It is observed that the distinct broad hollow peak is formed rather than intense crystalline peaks, which established the glassy amorphous nature of the glass samples (Dawngliana *et al.*, 2022). The intense peak at $2\theta = 23^0$ is credited to silica glass's amorphous nature. However, the XRD peaks are much sharper, and the material is crystallized with ZnS hexagonal

phase (Tiwary *et al.*, 2009) when the sample was annealed at a temperature greater than 500^0 C which was confirmed in our previous report.

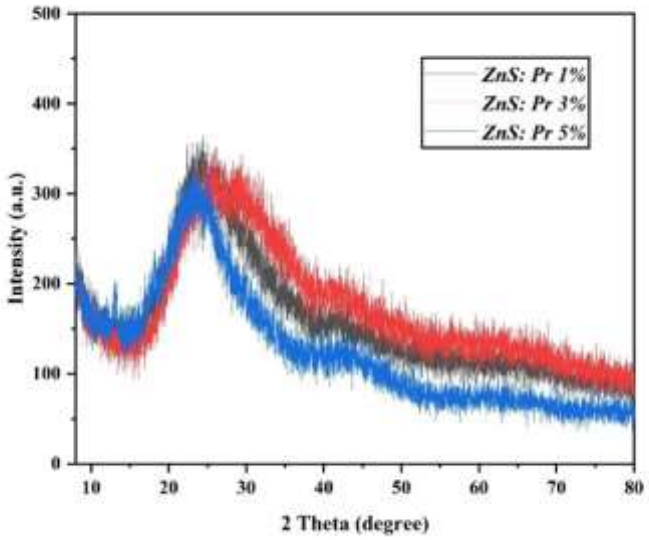

Fig. 4.6: XRD spectra of glasses.

TEM Study

As can be seen in the TEM micrograph of the examined doped sample, ZnS in the doped SiO_2 matrix was confirmed, and Pr^{3+} was found as depicted in Fig. 4.7 (a-c). The SAED image demonstrates a set of rings, indicating that the ZnS nanoparticles under study are polycrystalline, as shown in Fig. 4.7(b). The HRTEM image reveals an interplanar spacing of 0.106 nm in the ZnS doped Pr^{3+} glass matrix, as in Fig. 4.7(c).

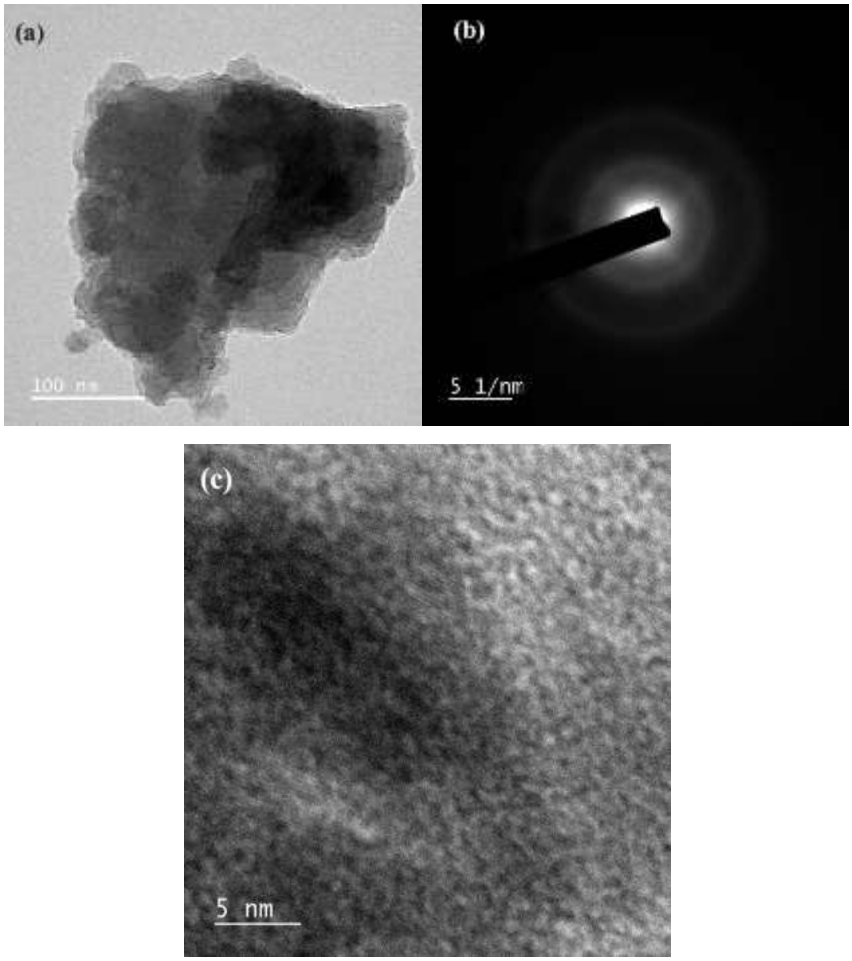

Fig. 4.7: (a) TEM image (b) SAED (c) HRTEM

4.3.2.3 Optical properties

Absorption spectra

Optical absorption properties of rare earth ions in the glass matrix generally depend on the neighboring environment of the rare earth ion and the interaction of the rare earth ion with ligand (Zhang *et al.*, 2012). The absorption spectrum of Pr^{3+} (3 mol %) doped ZnS nanoparticle sol-gel at room temperature is illustrated in Fig. 4.8. The spectra show four absorption peaks at 445 nm, 460 nm, 482 nm and 592 nm correspond to the transitions from the ground state $^3H_4$ to the excited states (Biswas *et al.*, 2022) $^3P_2$, $^3P_1$, $^3P_0$, and $^1D_2$ respectively. The samples appear pale green because of these transitions, which lie in the yellow-orange and violet-blue regions without eminent green absorption. For the Pr^{3+} ($4f^2$) ion, except the U^{4+} ($5f^2$) ions (Sobczyk *et al.*, 2010), the $^3H_4 \rightarrow {}^1D_2$ transition is found to be hypersensitive, whose

intensity varies significantly with environment due to a strong mixing of states $4f^2$ and $4f^15d^1$ (Wang *et al.*, 2015). Of all these, $^3H_4 \rightarrow {}^1D_2$ transitions are hypersensitive in nature as they depend on neighboring ligands and are governed by the selection rules $|\Delta S|=0$, $|\Delta L| \leq 2$, and $|\Delta J| \leq 2$ (Carnall *et al.*, 1965).

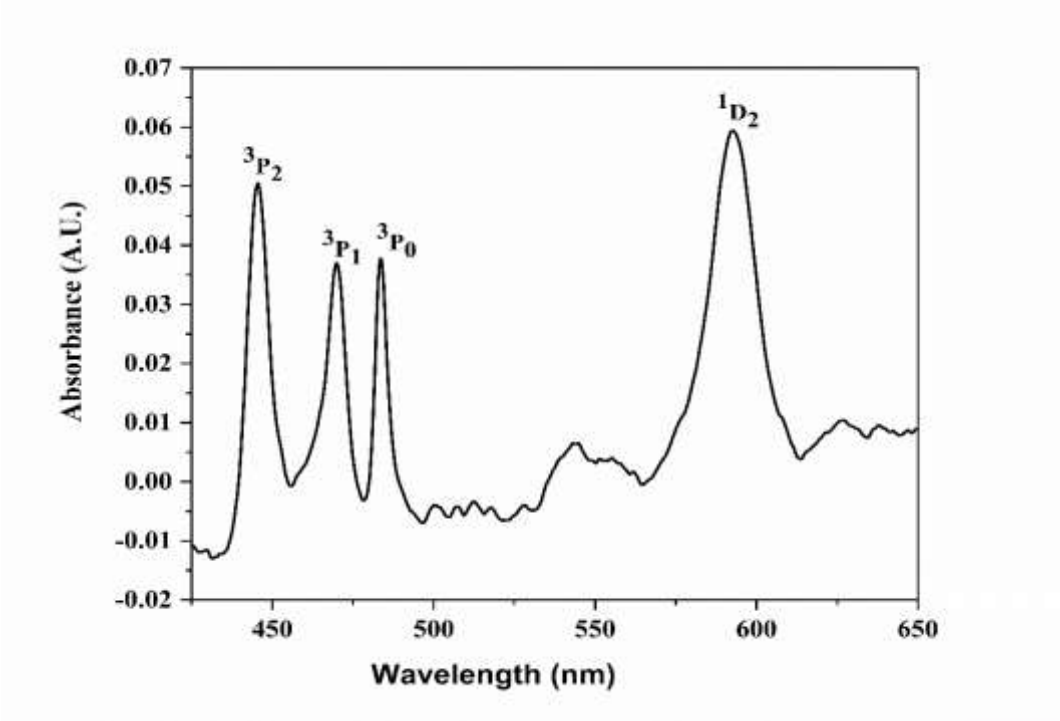

Fig. 4.8: Absorption spectra.

PL Spectra

Fig. 4.9 represents the PL spectra of different concentrations of Pr^{3+} doped with a fixed amount of ZnS nanoparticle (1.0 mol%) annealed to 1000 ^oC in the silica glass matrix. Several emission peaks were observed in the visible region due to radiative transitions from $^3P_0$, $^3P_1$ and $^1D_2$ states. The bands in the ranges 484-520nm are due to $^3P_0 \rightarrow {}^3H_4$ transitions; the prominent peak at 484 nm is due to $^3P_0 \rightarrow {}^3H_4$ transition. There are several emission peaks, which are due to the stark splitting of $^3H_4$ levels. The relatively weak bands at 530 nm, 615 nm, 647 nm and 734 nm are due to $^3P_1 \rightarrow {}^3H_5$, $^1D_2 \rightarrow {}^3H_4$, $^3P_0 \rightarrow {}^3F_2$, $^3P_0 \rightarrow {}^3F_4$ transitions, respectively. The emission intensities increase as the dopant concentration increases attaining a maximum value from 1% to 3% while gradually decreasing as the dopant concentration increases due to cross relaxation, causes concentration quenching. At 3 mol%, the emission intensities attain a maximum value. The PL spectra with Stark splitting are observed

for different concentration of Pr^{3+} co-doped ZnS nanoparticles in sol-gel silicate glasses annealed at 1000 °C which is consistent with the fact of modification of host with ZnS concentration (Dawngliana *et al.*, 2022). The schematic energy level diagram for different concentrations of Pr^{3+} doped with a fixed amount of ZnS is depicted in Fig. 4.10.

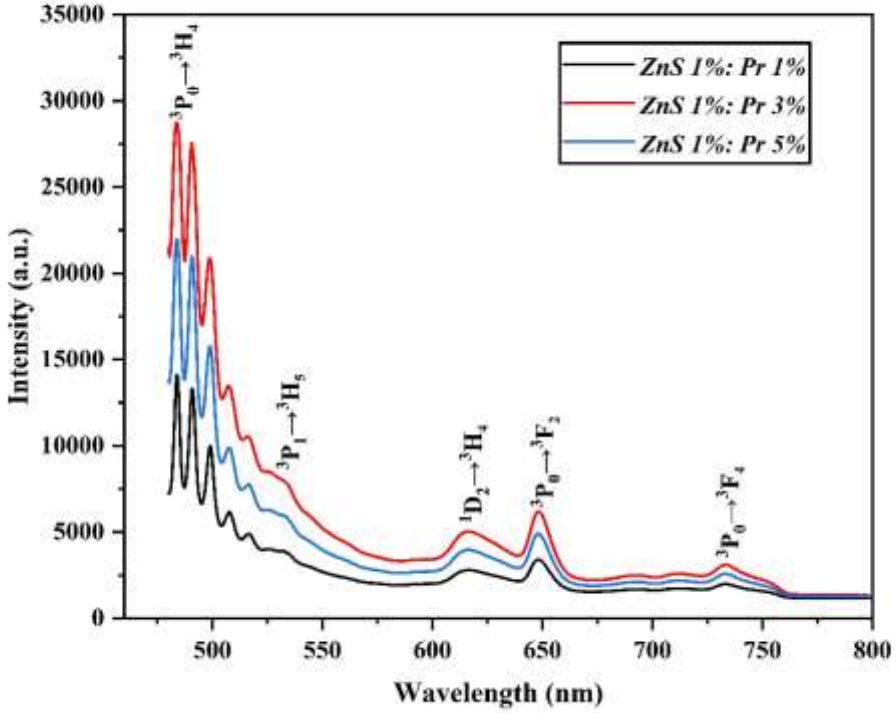

Fig. 4.9: PL Spectra.

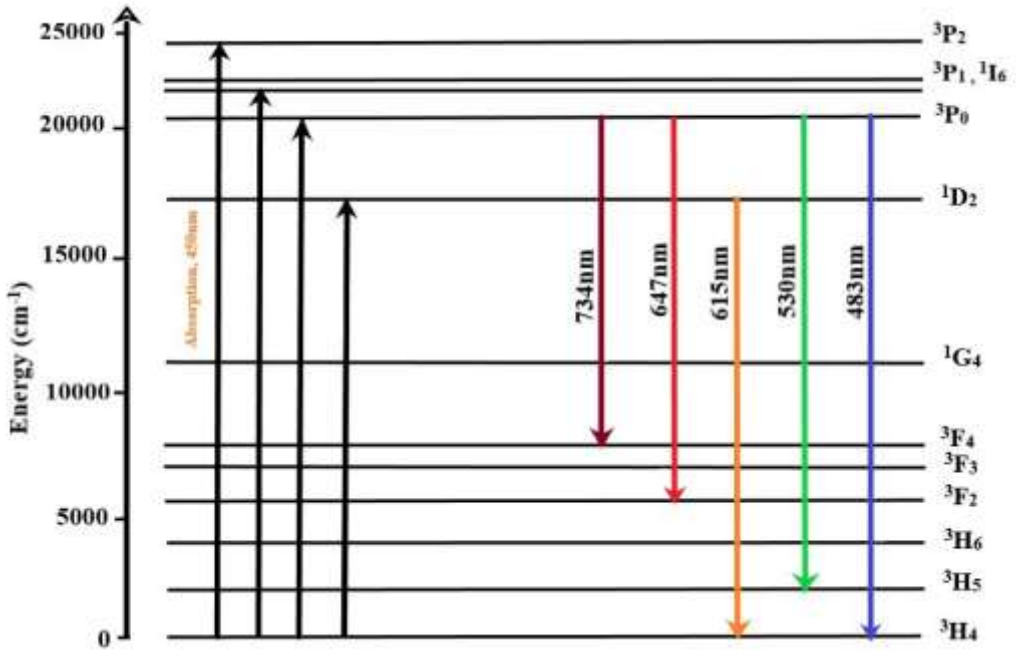

Fig. 4.10: Schematic energy level diagram.

Judd-Ofelt parameters

Even if the energy levels of the 4f states of RE ions don't vary much from host to host, the transition probabilities are nevertheless highly dependent on the ion's immediate environment. The oscillator strength of forced electric dipole transitions is frequently used to express the spectral intensities for the observed absorption peaks. Using the relation, the oscillator strengths of the transition are computed from Fig. 4.7.

$$f_{exp} = 4.319 \times 10^{-9} \int \varepsilon(\bar{\nu})\, d\bar{\nu} \qquad (4.7)$$

where $\varepsilon(\bar{\nu})$ is the molar absorptivity at energy $\bar{\nu}$ cm^{-1}

The theoretical oscillator strength is given by the Judd-Ofelt theory.

$$f_{cal}^{ed} = \frac{8\pi^2 mc\bar{\nu}\,(n^2+2)^2}{3h\,(2J+1)9n} \sum_{\lambda=2,4,6} \Omega_\lambda \left| < l^N SLJ \| U^\lambda \| l^N S'L'J' > \right|^2 \qquad (4.8)$$

where J is the total angular momentum of the initial state, n is the refractive index, h is Planck's constant, c is the speed of light, and m is the mass of the electron, $\|U^\lambda\|$ are the reduced matrix elements estimated in the intermediate coupling approximation for transition $|l^N SLJ > \rightarrow |l^N S'L'J'>$ at energy $\bar{\nu}$ expressed

in cm^{-1} and Ω_λ are the Judd- Ofelt intensity parameters (Hehlen *et al.*, 2013). The values $\|U^\lambda\|$ derived by Carnal et al. are used in the calculations.

By using the relations (4.7) and (4.8), JO intensity parameters were calculated and the experimental and calculated strengths of the oscillator [7] were indicated in Table 1. After obtaining the JO parameters, the line strength of any 4f transition $|l^N SLJ> \rightarrow |l^N S'L'J'>$ can be determined by using the relation

$$S = \sum_{\lambda=2,4,6} \Omega_\lambda \ |< l^N SLJ\|U^\lambda\| \ l^N S'L'J' >|^2 \quad (4.9)$$

The local structure and binding near the RE ions were also disclosed by the JO parameters. The JO parameters obtained are compared with glasses doped with another different host presented in Table 4.4. These parameters followed the trend $\Omega_6 > \Omega_4 > \Omega_2$ consisted of other reports for other doped materials. While Ω_4 and Ω_6 values depend on bulk properties, Ω_6 is known to decrease with an increase in host matrix rigidity (Yang *et al.*, 2007). A high Ω_6 value indicates an increase in ionicity between the ligand and rare-earth atoms, leading to a significant Stark splitting of the energy levels of Pr^{3+} ions. This, in turn, produces a wider emission band and more inhomogeneous broadening. The spectroscopic quality factor Ω_4 / Ω_6 determines the stimulated emission characteristics for laser active medium; the smaller this parameter, the more intense the laser transition $^3H_4 \rightarrow {}^1D_2$ (Henrie *et al.*, 1976); parameter Ω_2 is structure-sensitive and related to the symmetry and covalency of the RE ion site (Bokatial *et al.*, 2010). The ion site is more centro-symmetric and its chemical bond with the ligand is more ionic when the value of Ω_2 is smaller, both of which contribute to the covalent character (Amjad *et al.*, 2015).

Table 4.3: Strengths of oscillators and JO intensity parameters

Transition	**Wavelength**	**Energy (cm^{-1})**	**f_{exp} (10^{-6})**	**f_{cal} (10^{-6})**	**Ω_λ (10^{-20} $cm^{2)}$**	
$^3H_4\rightarrow$	592	16832	2.35	2.78	Ω_2= 0.46	
$^1D_2$	482	20667	5.13	5.24	Ω_4= 0.85	Ω_4/Ω_6= 0.45
$^3P_0$	460	21251	3.28	3.37	Ω_6= 1.90	
$^3P_1$	445	22442	2.49	0.41		
$^3P_2$						

Table 4.4: Comparison of Pr^{3+}'s JO parameters in different glasses.

Glasses doped with	**Ω_2**	**Ω_4**	**Ω_6**	**Trend**	**Ω_4/Ω_6**
ZnS	0.46	0.85	1.90	$\Omega_6 > \Omega_4 > \Omega_2$	0.45
Al	5.40	3.88	7.41	$\Omega_6 > \Omega_4 > \Omega_2$	0.52
Phosphate	1.43	4.22	4.87	$\Omega_6 > \Omega_4 > \Omega_2$	0.87
Borophosphate	1.05	3.49	6.30	$\Omega_6 > \Omega_4 > \Omega_2$	0.55
CdS	10.38	7.4	0.95	$\Omega_2 > \Omega_4 > \Omega_6$	7.79
Borate	0.50	4.98	5.00	$\Omega_6 > \Omega_4 > \Omega_2$	0.99
Chlorophosphate	2.32	3.05	5.86	$\Omega_6 > \Omega_4 > \Omega_2$	0.52
Aluminoborophosphate	0.88	5.24	6.59	$\Omega_6 > \Omega_4 > \Omega_2$	0.79

Radiative properties

For estimating various radiative properties, the JO intensity parameters calculated from absorption spectra are combined with transitions from $^3P_0$, $^3P_1$ and $^1D_2$ states of Pr^{3+} (3.0 mol %) with ZnS (1.0 mol%) doped sol-gel silica glass. The emission peaks cross-section [$\sigma_P(\lambda_P)$] among initial (ΨJ) and a terminal manifold ($\Psi' J'$) are calculated from (Rai *et al.*, 2011)

$$\sigma_p(\lambda_p) = \frac{\lambda_p^4}{8\pi c n^2 \Delta\lambda_{eff}} A(\Psi J; \Psi' J') \quad (4.10)$$

where λ_p is the emission peak wavelength, $\Delta\lambda_{eff} = \frac{\Delta I(\lambda) d\lambda}{I_{max}}$ is the effective bandwidth, n is the refractive index, and $A(\Psi J; \Psi' J')$ is the emission probability of the particular transition estimated in Table 4.6. The electric-dipole probability is the only factor considered in the radiative transition probability computation between the

initial (ΨJ) and terminal manifold ($\Psi' J'$) (Dawngliana *et al.*, 2022) along with the average wavelength of transition λ.

$$A_{ed}(\Psi J; \Psi' J') = \frac{64\pi^4 e^2 n(n^2+2)^2}{3h\lambda^3 (2J+1)9} \sum_{\lambda=2,4,6} \Omega_\lambda x (\Psi J||U^\lambda||\Psi' J')^2 \quad (4.11)$$

The summation of $A(\Psi J; \Psi' J')$ represents all states that participated in the transition from excited state ΨJ to ground state $\Psi' J'$, in turn denotes the total radiative probability (A_s), mathematically $A_s = \sum A(\Psi J; \Psi' J')$, the inverse of this total radiative probability (τ_R) is termed the radiative lifetime that determines the depopulation rate from a specific state (Dawngliana *et al.*, 2022).

The various transitions' branching ratios are computed as

$$\beta_R = \frac{A(\Psi J; \Psi' J')}{\sum^A (\Psi J; \Psi' J')} \quad (4.12)$$

An excited state $\Psi' J'$ can have its radiative lifetime computed from

$$\tau_R = \frac{1}{\sum(\Psi J; \Psi' J')} \quad (4.13)$$

The above relations (4.12) and (4.13) are used to calculate the different radiative parameters of Pr^{3+} (3.0 mol %) doped ZnS (1.0 mol %) silica glass as displayed in Table 4.5. The Figure of Merit (FOM) which is used to evaluate the bandwidth properties of optical fiber amplifiers and is defined as (Mohan *et al.*, 2018), is also calculated. Its value suggests that the doped glass system may find application in optical amplifier devices.

$$FOM = \Delta\lambda_{eff} X \sigma_p \quad (4.14)$$

Table 4.5: Radiative transition probability (A_{ed}), total radiative probability (A_T), radiative lifetime (τ_R) and branching ratio (β_r (in %)) for the emission of Pr^{3+} (3.0 mol %) doped ZnS (1.0 mol %) silica glass.

Transition	**Energy (in cm^{-1})**	**A_{ed} (in s^{-1})**	**β_r (in %)**
$^3P_0 \rightarrow {}^3H_4$	20833	1412.00	46.32
$^3P_1 \rightarrow {}^3H_5$	18868	15.40	0.51
$^1D_2 \rightarrow {}^3H_4$,	16260	1421.03	46.62
$^3P_0 \rightarrow {}^3F_2$	15456	1179.50	38.69
$^3P_0 \rightarrow {}^3F_4$	13624	432.34	14.18
		A_T = 3048.28	τ_R= 0.33 (ms)

Table 4.6: Transitions wavelength, energy, effective bandwidth, stimulated cross-section and FOM of different peaks of Pr^{3+} (3.0 mol %) doped ZnS (1.0 mol %) doped silica glass.

Transition	**Wavelength (λp) (nm)**	**Energy (in cm^{-1})**	**λ_{eff} (nm)**	**σ_p (x 10^{-23} cm^2)**	**FOM**
$^3P_0 \rightarrow {}^3H_4$	484	20833	6.02	38.05	22.91
$^3P_1 \rightarrow {}^3H_5$	530	18868	32.90	1.10	3.62
$^1D_2 \rightarrow {}^3H_4$,	615	16260	32.27	1.88	6.1
$^3P_0 \rightarrow {}^3F_2$	647	15456	16.92	1.17	1.98
$^3P_0 \rightarrow {}^3F_4$	734	13624	56.55	1.40	7.91

Annealing effect on PL spectra

The PL spectra of Pr^{3+} (3.0 mol %) doped with a fixed amount of ZnS (1.0 mol%) nanoparticles in sol-gel glass at various annealing temperatures are shown in Fig. 4.11 and Fig. 4.12 illustrate the annealing temperature versus prominent emission peaks of the $^3P_0 \rightarrow {}^3H_4$ transition. An exponential increase in the intensity was observed after heating the studied glass from 600^{o}C onwards. We know that the sol-gel technique is a wet chemical process; there are a lot of hydroxyl groups present at lower temperatures, which lowers the emission intensity. As illustrated in Fig. 4.11 and 4.12, improving annealing temperature removing the hydroxyl groups, causing a dramatic enhancement in the emission intensity. The elimination of the hydroxyl group also lowers the weight of the sample. Slow annealing at 1000°C minimizes hydroxyl quenching and stops additional atmospheric moisture absorption by constricting and sealing the pores thereby enhancing the luminescence. Consequently, resulting in densification of the sample, thereby sealing the pores present, which protect them from atmospheric reabsorption and sustain luminescence properties after a long time (Fanai *et al.*, 2019). For PL spectra for different concentrations of Pr^{3+} co-doped ZnS nanoparticles in sol-gel silica glasses (Table 4.7), it is observed to show Stark splitting at transitions $^3P_0 \rightarrow {}^3H_4$ in Pr^{3+} in silica glass when annealed at 1000 °C which is consistent with the fact of modification of host at the higher temperature (Dawngliana *et al.*, 2022). Similarly, the variation of annealing temperature of Pr^{3+} (3.0 mol%) co-doped ZnS nanoparticles in sol-gel silica glass also shows Stark splitting at transitions $^3P_0 \rightarrow {}^3H_4$ as presented in Table 4.8.

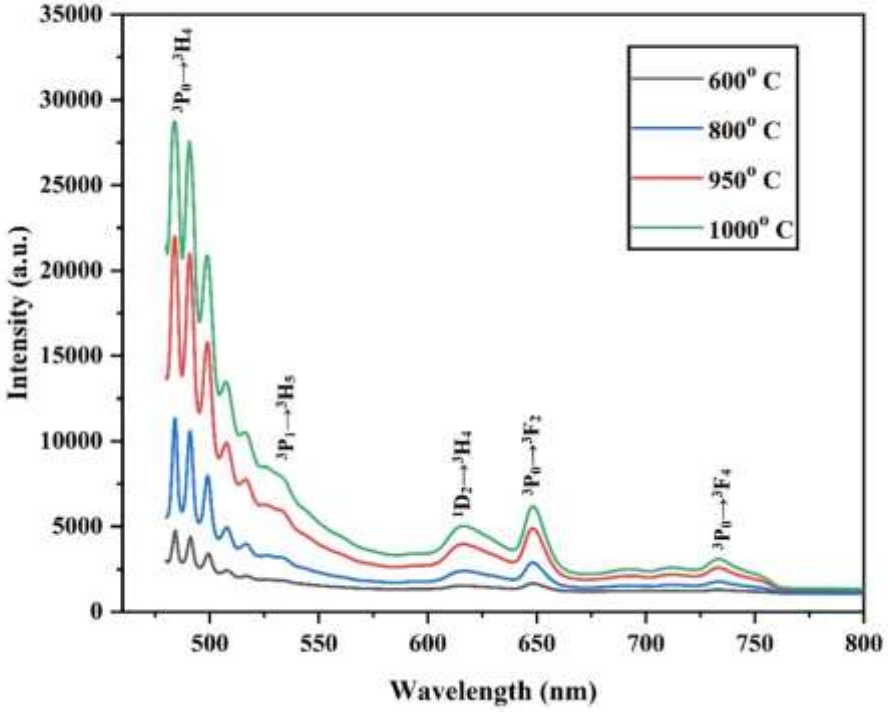

Fig. 4.11: PL spectra of studied glass at various annealing temperatures.

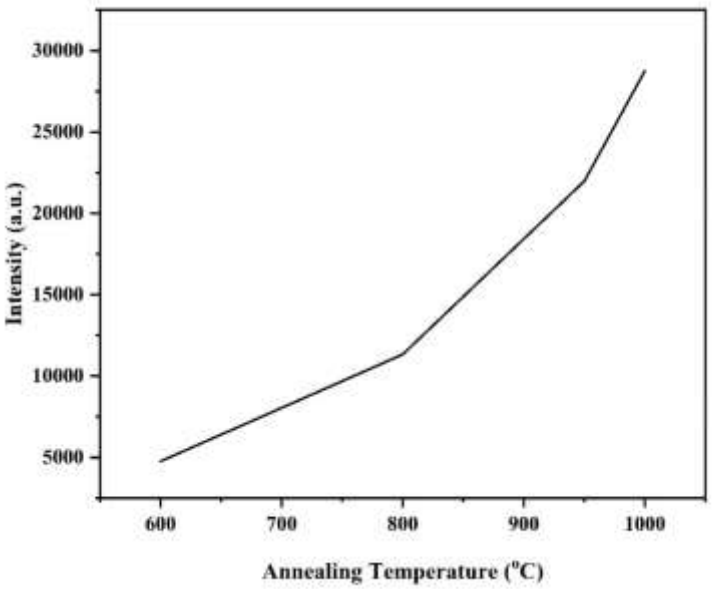

Fig. 4.12: Annealing temperature Vs. PL intensity of $^3P_0 \rightarrow {}^3H_4$ transition.

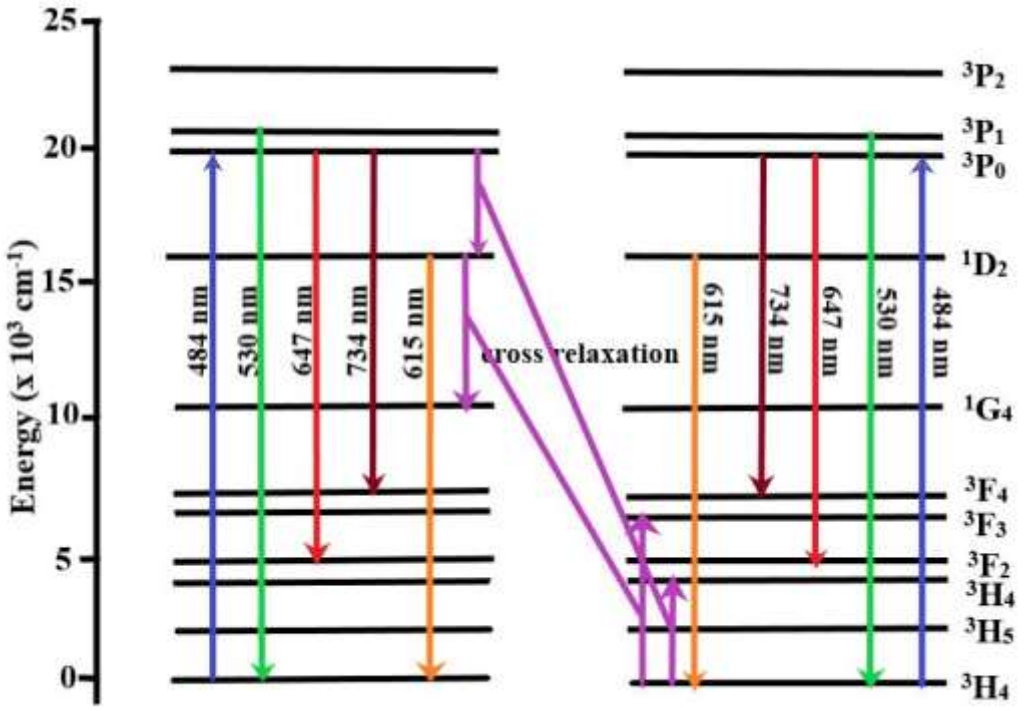

Fig. 4.13: Cross-relaxation mechanism of Pr^{3+} co-doped ZnS silicate glass.

Table 4.7: Stark splitting in the spectrum for different concentration of Pr^{3+} (1.0, 3.0, 5.0 mol %) co-doped ZnS nanoparticles in sol-gel silicate glasses.

Transitions $^3P_0 \rightarrow {}^3H_4$	**Wavelength (λ_P) (nm)**	**Energy (in cm^{-1})**	**Assignment**
1.0 mol %	483	20703	0
	491	20366	337
	498	20080	623
	508	19685	1018
	518	19305	1398
3.0 mol %	484	20661	0
	491	20366	295
	498	20080	581
	507	19724	937
	516	19380	1281
5.0 mol %	484	20661	0
	491	20366	295
	498	20080	581
	508	19685	976
	517	19342	1319

Table 4.8: Stark splitting in the spectrum for Pr^{3+} (3.0 mol%) doped ZnS in sol-gel silicate glasses at different annealing temperatures.

Transitions $^3P_0 \rightarrow {}^3H_4$	**Wavelength (λ_P) (nm)**	**Energy (in cm^{-1})**	**Assignment**
600° C	484	20661	0
	491	20366	295
	499	20040	621
	508	19685	976
	517	19342	1319
800° C	484	20661	0
	491	20366	295
	499	20040	621
	508	19685	976
	517	19342	1319
950° C	484	20661	0
	491	20366	295
	499	20040	621
	508	19685	976
	517	19342	1319
1000 °C	484	20661	0
	491	20366	295
	498	20080	581
	508	19685	976
	516	19380	1281

CIE Chromaticity

In order to determine the actual color emissions of the material, examining the color coordinates shown on a traditional chromaticity diagram is necessary. A tool used to measure the tunability of the emission wavelength and the intensity variation in the emission band is the (Kirdsiri *et al.*, 2019) CIE 1931 (Commission International de'Eclairage) diagram. It is a universal method of representing every color by combining three primary colours. The CIE Chromaticity diagram of ZnS doped with varying concentrations of Pr^{3+} is shown in Fig. 4.14 which were derived from their corresponding PL spectra at 450nm excitation. The following equations (4.2), (4.3), and (4.4) are used to derive the chromaticity coordinates from the tri-stimulus values (Wang *et al.*, 2010).

The green emission is one of the important characteristics of Pr^{3+} ions emissions, hence, glasses doped with Pr^{3+} can be used as a candidate for a green light

source. The aforementioned factor explains why current glasses emit light in the green region at a noticeable intensity for laser action, light-emitting diodes and display applications.

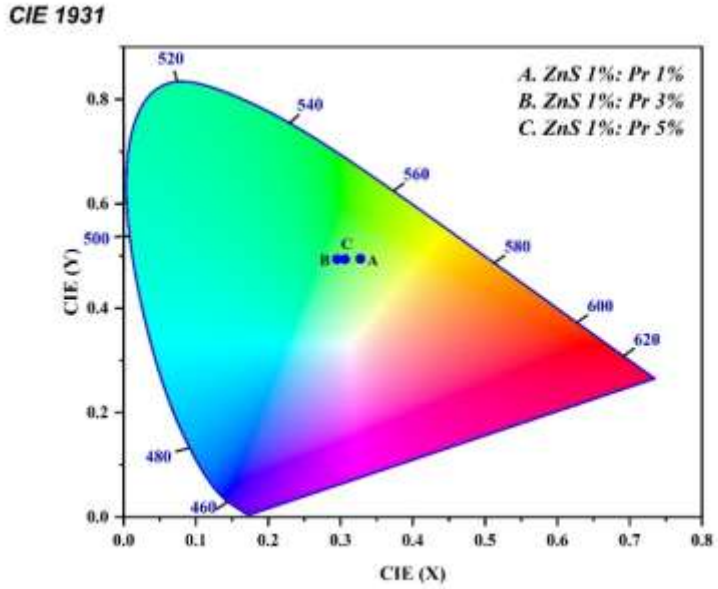

Fig. 4.14: CIE Chromaticity of different concentrations of Pr^{3+} doped with a fixed amount of ZnS nanoparticle in silica glass.

Table 4.9: CIE chromaticity coordinates of different concentrations of Pr^{3+} ions doped ZnS nanoparticle.

ZnS: *x* Pr^{3+}	**X**	**Y**
1.0 mol %	0.328	0.495
3.0 mol %	0.295	0.494
5.0 mol %	0.306	0.494

4.3.3 Effect of γ- ray irradiation on the optical properties of Sm^{3+} doped silica glass

4.3.3.1 Before and after gamma irradiation of PL spectra

In Fig. 4.15(a), illustrate the PL spectra of Sm^{3+} doped silica glass recorded after exciting it with wavelength 450 nm in the range of 520-750 nm. The result revealed three emission peaks at about 567 nm ($^4G_{5/2} \rightarrow {}^6H_{5/2}$ transition) with

intensity 1323 cm^{-1}, 606 nm ($^4G_{5/2} \rightarrow {}^6H_{7/2}$ transition) with intensity 1420 cm^{-1} and 652 nm ($^4G_{5/2} \rightarrow {}^6H_{7/2}$ transition) with intensity 2263 cm^{-1}. In the present report, attention has been paid to these emission peaks for studying the effect of γ-irradiation.

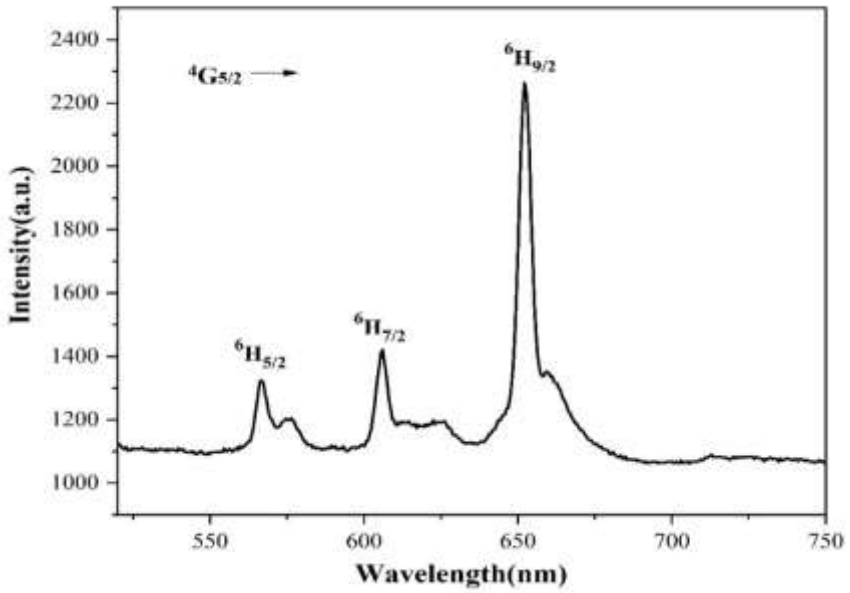

Fig.4.15(a): Before gamma irradiation of PL spectra

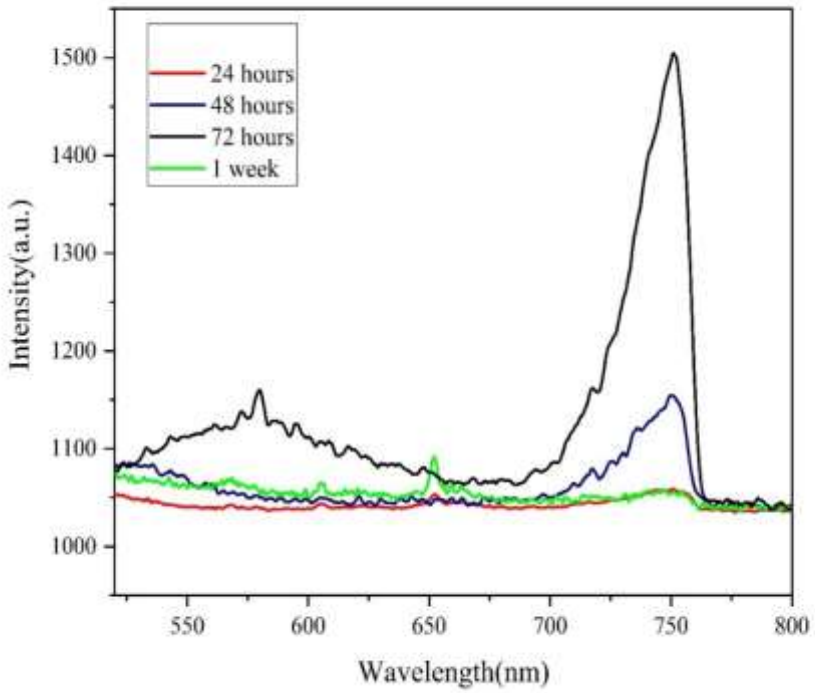

Fig. 4.15(b): After ɣ-irradiation of PL spectra

In Fig. 4.15(b), the photoluminescence spectra of studied glass excitation with 450nm wavelength after gamma radiation within one week. The figure reveals that after irradiating the studied glass with gamma (10 Gy). The emission peaks of the normal glass dissappeared after the sample was irradiated with gamma. Moreover, a new peak belonging to Sm^{2+} appears at 750 nm and Sm^{3+} retains its normal condition after 1 week of irradiation. From this figure, we can understand the detailed effects of gamma irradiation on the studied glass.

4.3.3.2 Gamma induced defects in glasses.

PL spectra of Sm^{3+} doped silica glass were recorded before and after ɣ-irradiation of 10 Gy at room temperature. As we can see from Fig. 4.16, broad emission peaks were observed at 750 nm while a normal glass does not show it. This observation shows that the valence state of Samarium ions changes from Sm^{3+} to Sm^{2+} during gamma irradiation, and this shift is time-dependent. The gamma ray produces ionization in SiO_2 with the release of electrons. The free electrons travel

through conduction bands and are finally trapped at the electronegative Sm^{3+} site, and the Sm^{3+} is converted into Sm^{2+}. That photoreduction of Sm^{3+} to Sm^{2+} by gamma irradiation was also reported for Sm^{3+} doped oxyfluoroborate glasses and alumina-silicate glasses (Madhu *et al.*, 2020; Hari Babu *et al.*, 2012). As a result of the irradiation process, free electrons were able to move throughout the glass network structure, creating positive holes. These generated pairs of electrons and positive holes are reacted to or captured through intrinsic defects or trace impurities already present in the glasses (Rai *et al.*, 2012). So, that gamma irradiation may improve the glasses optical properties. While change in valency was not reported for other Sm^{3+} doped glasses, which means some dopants show obvious shielding to irradiation and optical spectra still remain after irradiation (Okasha *et al.*, 2018; Marzouk *et al.*, 2018). After 24 hours of irradiation, the sample shows a low intensity peak even after 48 hours also, while at 72 hours the band shows the highest intensity indicating that the changing of the valence state of Sm from Sm^{3+} to Sm^{2+} reaches a maximum after 72 hours of irradiation. After 1 week or 144 hours, the sample does not show not many Sm^{2+} characteristics as seen from Fig. 4.17. In general, charged defects in the material are extremely easily produced by high energy gamma irradiation. It appears that photons interact with the ions in the silica glass as they pass through it. When a photon's energy exceeds 0.1 MeV, the Compton Effect is more likely to occur. A portion of the photon's energy is transmitted to the Compton electron that has been detached from the atom during Compton scattering. This electron then interacts with other electrons in the material to form a number of secondary electrons (Rai *et al.*, 2012). In the current experiment, these secondary electrons can be caught by Sm^{3+} ions, oxygen vacancies, and other ions. As a result, the number density of Sm^{3+} ions will drop and the intensity will rise due to an increase in Sm^{2+}, as seen in the experimental results. Which means in irradiated glasses, the energy transfer takes place between Sm^{3+} and Sm^{2+} by cross relaxation between $^4G_{5/2} \rightarrow {}^6H_{5/2}$ and $^5D_0 \rightarrow {}^7F_0$ (Madhu *et al.*, 2020). It can be expressed as

O^{2-} (collided by Compton electron)$\rightarrow O^- + e^-$

$V_o + e^- \rightarrow F^+$ (one electron trapped at vacancies of oxygen atom)

$F^+ + e^- \rightarrow F$ (two electrons trapped at the vacancy of oxygen ion)

$Sm^{3+} + e^- \rightarrow Sm^{2+}$

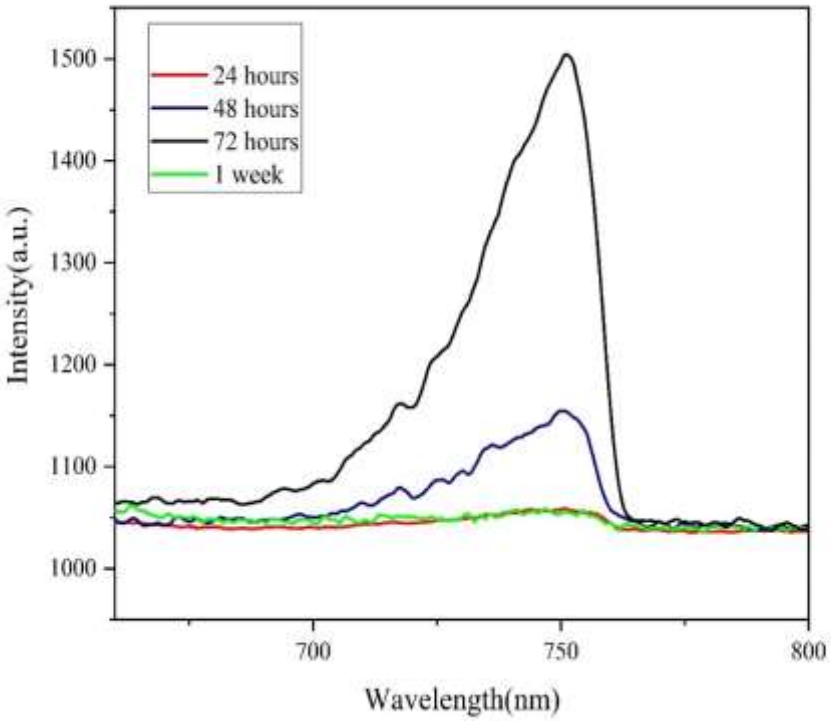

Fig.4.16: Changing intensity of Sm^{2+} after Gamma irradiation at room temperature.

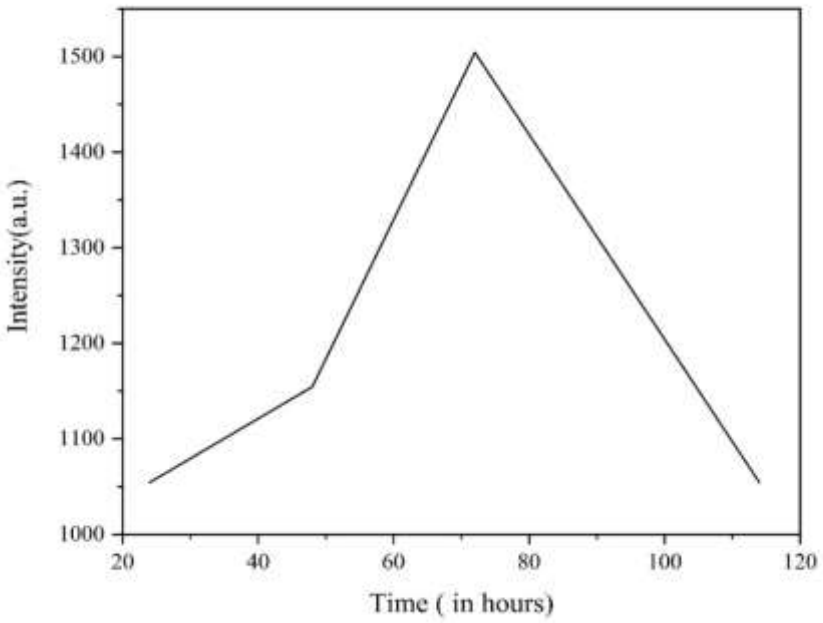

Fig.4.17: Changing intensity of Sm^{2+} after gamma irradiation with time.

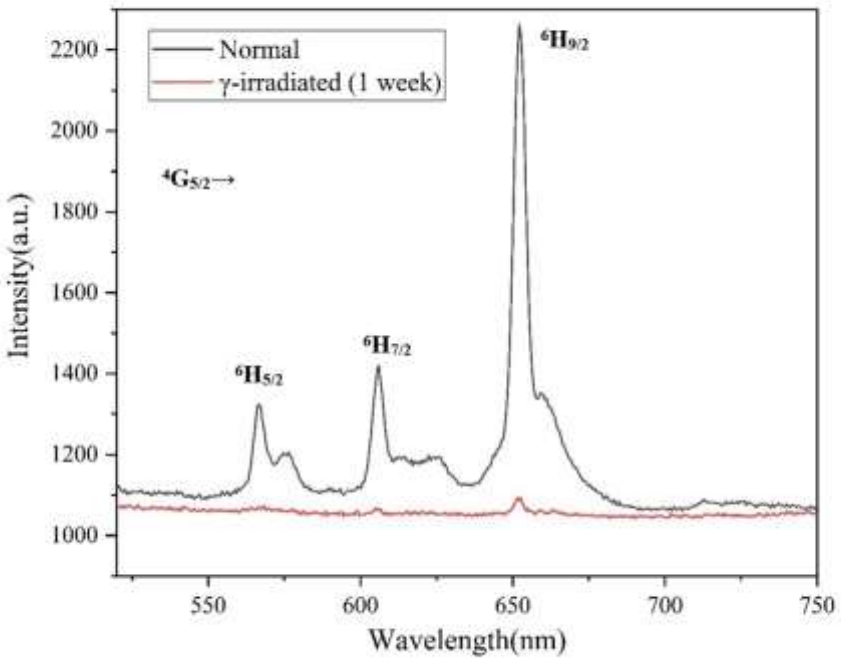

Fig. 4.18: Sm^{3+} spectra of normal and gamma irradiated (one week) glasses at room temperature.

These irradiation induced changes seems to be irreversible at room temperature in the present studied glass, as it's starting to show similar spectra after one week of irradiation, as shown in Fig. 4.18. This might be because the material isn't conducting in nature and the mobility of the flaws is very low or nonexistent. After annealing, a reversal process has been seen in some irradiated crystals (Rai, 2010; Marzouk *et al.*, 2018).

4.3.3.3 Effect of irradiation on FTIR of Sm^{3+} doped silica glass

Fig. 4.19(a) and Fig. 4.19(b) represent the FTIR spectra of the present glass before gamma irradiation and after gamma irradiation. The most effective method that can reliably identify the type of glass and the constitutional network building units is infrared spectroscopy. As can be seen in Figs. 4.19(a) and 4.19(b), there was no distinct change in the FTIR spectrum following the irradiation treatment. The observed peaks of the sample can be interpreted as shown in Table 4.10.

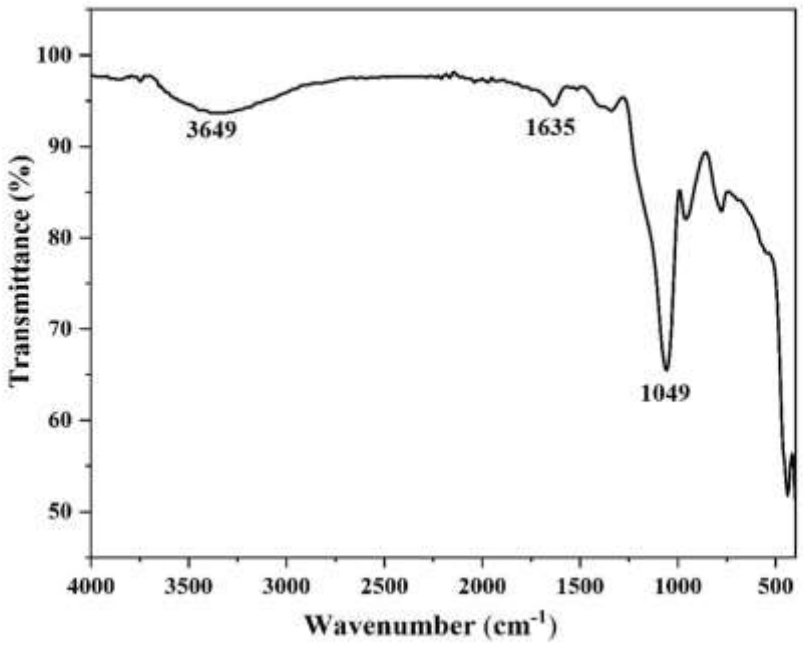

Fig. 4.19(a): Before ɣ-irradiation of FTIR spectra.

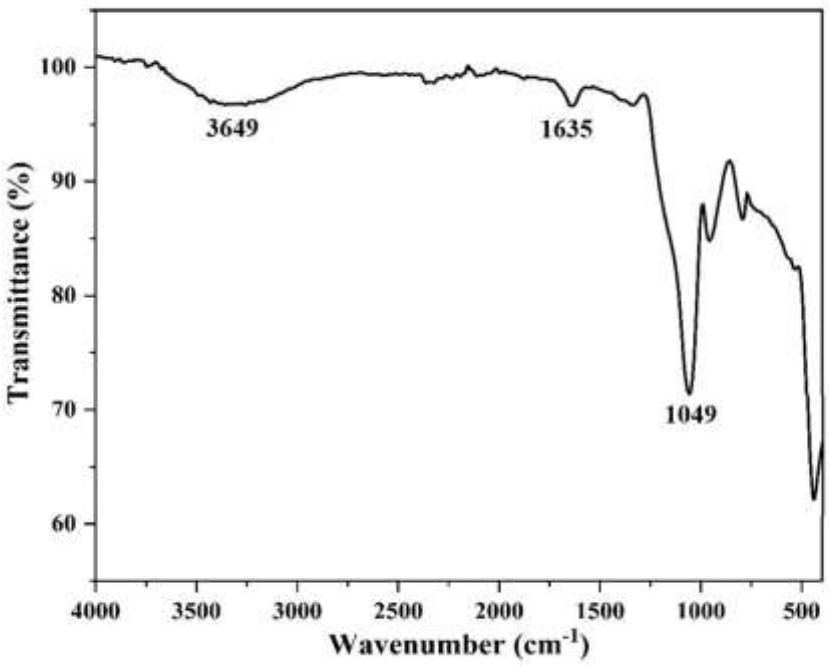

Fig. 4.19(b): After ɣ-irradiation of FTIR spectra.

Table 4.10: Assignment of peaks

Peak position(cm^{-1})	**Assignment**
1049-1056	Si-O-Si stretching
1342-1635	Sm^{3+} stretching
2962-3649	Related to water, O-H stretching

4.4 Conclusions

Samarium doped glass

Sm^{3+} ions doped with a fixed amount of ZnS (1 mol %) nanoparticle in silica glass matrix have been synthesized successfully using a sol-gel technique. Therefore, sol-gel methods are recommended for synthesizing the glass sample since it is a very low-cost method compared to other techniques. The density, refractive index, and various physical properties were calculated. SAED studies confirmed the development of hexagonal polycrystalline structure, while XRD studies the formation of amorphous nature. TEM confirmed that the particles size varies from 10 to 50 nm. The PL spectra have three emission bands that correspond to $^4G_{5/2}\rightarrow{}^6H_{5/2}$, $^4G_{5/2}\rightarrow{}^6H_{7/2}$ and $^4G_{5/2}\rightarrow{}^6H_{9/2}$ correspondingly at 565 nm, 603 nm, and 650 nm with the most prominent bands in the green and orange-red region. The examined glass can produce a nearly pure white hue when triggered at 370 nm, according to the CIE color chromaticity and CCT measurements.

Praseodymium doped glass

The fixed concentration of ZnS nanoparticles doped with different concentrations of Pr^{3+} in silica glass matrix has been successfully prepared by the sol-gel method. The FTIR spectra reveal the composition, quality of the sample, and removal of OH group with annealing. SAED studies confirmed the development of

polycrystalline structure, while XRD studies the formation of amorphous nature. TEM confirmed that the particle size varies from 10 to 50 nm. The Judd-Ofelt parameters Ω_2, Ω_4 and Ω_6 were calculated from the absorption spectrum in the visible region and compared with different glasses. PL emission was carried out with 450nm excitation in the VIS-NIR regions with bands at 484 nm, 530 nm, 615 nm, 647 nm and 734 nm due to $^3P_0 \rightarrow {}^3H_4$, $^3P_1 \rightarrow {}^3H_5$, $^1D_2 \rightarrow {}^3H_4$, $^3P_0 \rightarrow {}^3F_2$, $^3P_0 \rightarrow {}^3F_4$ transitions, respectively. Co-doping with ZnS enhanced green luminescence of the $^3P_0 \rightarrow {}^3H_4$ transition with a stark splitting was observed. The CIE chromaticity indicates that the studied glasses can be used as a candidate for green light generation for device application. In addition, slow annealing at 1000 °C is recommended for RE-doped with ZnS sol-gel silica glasses because it minimizes hydroxyl quenching and stops additional atmospheric moisture absorption by constricting and sealing the pores. Our report may be useful for applications in solid-state laser development.

γ- ray irradiation effect on Sm^{3+} doped silica glass

The PL spectra of Sm^{3+} doped silica glass have been studied before and after γ- irradiation. It has been found that the valency of Sm^{3+} was reduced to Sm^{2+} after gamma irradiation process due to energy transfer from Sm^{3+} to Sm^{2+}. The report reveals that the Sm^{2+} characters were highest after 72 hours of irradiation. Moreover, the Sm^{3+} regained its original characteristics after 148 hours or 1 week of irradiation, indicating that the valency reducing process was irreversible in nature and a time dependent mechanism. On the other hand, the FTIR spectra show that the composition of glasses was not affected by the gamma irradiation. This experimental report shows the co-existence of Sm^{3+} and Sm^{2+} which needed higher energy to trigger it out; it is also evidence that the 10 Gy of gamma was an efficient dose for trigging out the Sm^{2+} nature. Such research may be useful in discovering radiation-hard glass materials and glasses with enhanced radiative characteristics for high power lasers.

REFERENCES

Annapurna Devi Ch.B., K. Swapna, S.K. Mahamuda, M. Venkateswarla, M.V.V.K.S. Prasad, K. Siva Rama Krishna Reddy, Nisha Deopa, A.S. Rao (2019) Spectroscopic studies and lasing potentialities of Sm^{3+} ions doped single alkali and mixed alkali fluoro tungsten tellurite glasses. *Opt. Laser Technol.* **111**:176-183. doi: https://doi.org/10.1016/j.optlastec.2018.09.051

Yasi J, Fusong J, Fuxi G (1982) Optical and other physical properties of Al $(PO_3)_3$-containing fluorophosphate glasses. *J. Phys.* **43**:315-318. doi:10.1051/jphyscol:1982958

Haralampieva A, Lozanova I.S., Dimitrov V. (2012) Optical properties and structure of Bao-V_2O_5 and Fe_2O_3-Bao-V_2O_5 glasses. *J. Chem. Technol. Metallurgy* **47**:392-397.

Tiwary C.S., Kumbhakar P, Mitra A.K., Chattopadhyay K (2009) Synthesis of wurtzite-phase ZnS nanocrystal and its optical properties. *J. Lumin.* **129**:1366-1370. doi: https://doi.org/10.1016/j.jlumin.2009.07.004

Dieke G.H. (1968) Spectroscopy & Energy Levels of Rare Earth Compounds, Inter Science, New York.

Carnall W.T., Fields P.R., Rajnak K (1968) Spectral Intensities of the Trivalent Lanthanides and Actinides in Solution. II. Pm^{3+}, Sm^{3+}, Eu^{3+}, Gd^{3+}, $Tb^{3+,}$ Dy^{3+}, and Ho^{3+}. *J. Chem. Phys.* **49**:4412-4428. doi: https://doi.org/10.1063/1.1669892

Yoon S.J., Pi J.W., Park K (2018) Structural and photoluminescence properties of solution combustion-processed novel ZrO_2 doped with Eu^{3+} and Al^{3+}. *Dyes and Pigments* **150**: 231-240. doi: https://doi.org/10.1016/j.dyepig.2017.12.012

McCamy C S (1992) Correlated color temperature as an explicit function of chromaticity coordinates. *Color Res. Appl.* **17**:142. doi: https://doi.org/10.1002/col.5080170211

Ambast A K, Goutam J, Som S, Sharma S K (2014) $Ca_{1-x-y}D_{yx}K_y\ WO_4$: A novel near UV converting phosphor for white light emitting diode. *Spectrochim. Acta A Mol. Biomol. Spectrosc.* **122**:93-99. doi: https://doi.org/10.1016/j.saa.2013.11.032

Dawngliana KMS, Rai S (2022) Linear and nonlinear and optical properties of Sm^{3+} co- doped alumino-silicate glass prepared by sol-gel method. *J. Non-Cryst. Solids* **598**:121929. doi: https://doi.org/10.1016/j.jnoncrysol.2022.121929

Liaolin Zhang, Guoping Dong, Mingying Peng, Jianrong Qiu (2012) Comparative investigation on the spectroscopic properties of Pr^{3+}-doped boro-phosphate, boro-germo-silicate and tellurite glasses. *Spectrochim. Acta A Mol. Biomol. Spectrosc.* **93**:223-227. doi: https://doi.org/10.1016/j.saa.2012.02.076

Joydeb Biswas, Samar Jana, Sourav Ghosh, Venkataramanan Mahalingam (2022) Optical and luminescence properties of Sm_2O_3 doped SrO–PbO–ZnO–P_2O_5–TeO_2 glasses for visible laser applications. *Solid State Sci.* **129**:106910. doi: https://doi.org/10.1016/j.solidstatesciences.2022.106910

Marcin Sobczyk, Janusz Drozdzyn'ski (2010) Optical properties of U4+-doped KPb_2Cl_5 single crystal. *Struct. Chem.* **21**:455–459. doi:10.1007/s11224-009-9559-0

Wang Q, Zhu G, Li Y, Wang Y (2015) Photoluminescent properties of Pr3+ activated Y2WO6 for light emitting diodes. *Opt. Mater.* **42**: 385–389. doi: http://dx.doi.org/10.1016/j.optmat.2015.01.032

Carnall W. T, Fields P. R, Wybourne B. G. (1965) Spectral Intensities of the Trivalent Lanthanides and Actinides in Solution. I. Pr3+, Nd3+, Er3+, Tm3+ and Yb3+. *J. Chem. Phys.* **42**:3797–3806. doi: https://doi.org/10.1063/1.1695840.

Yang Yanmin, Yao Baoquan, Chen Baojiu, Wang Cheng, Ren Guozhong, Wang Xiaojun (2007) Judd–Ofelt analysis of spectroscopic properties of Tm^{3+}, Ho^{3+} doped $GdVO_4$ crystals. *Opt. Mater.* **29(9)**: 1159-1165. doi: https://doi.org/10.1016/j.optmat.2006.06.003

Henrie D.E., Fellows R.L., Choppin G.R. (1976) Hypersensitivity in the electronic transitions of lanthanide and actinide complexes. *Coord. Chem. Rev.* **18(2)**:199-224. doi: https://doi.org/10.1016/S0010-8545(00)82044-5

Raja J. Amjad, Dousti M.R., Sahar M.R. (2015) Spectroscopic investigation and Judd–Ofelt analysis of silver nanoparticles embedded Er^{3+}-doped tellurite glass. *Curr. Appl. Phys.* **15(1)**:1-7. doi: https://doi.org/10.1016/j.cap.2014.10.022

Bokatial L, Rai S (2010) Optical properties and up-conversion of Pr^{3+} doped CdS nanoparticles in sol–gel glasses. *J. Lumin.* **130**: 1857-1862. doi: https://doi.org/10.1016/j.jlumin.2010.04.022

Kirdsiri K, Rajaramakrishna R, Damdee B, Kim H.J., Nuntawong N., Mati Horphathum, Kaewkhao J (2019) Influence of alkaline earth oxides on Eu3+ doped lithium borate glasses for photonic, laser and radiation detection material applications. *Solid State Sciences* **89**:57-66. doi: https://doi.org/10.1016/j.solidstatesciences.2018.12.019

Fanai AL, Khan U, Rai S (2019) Luminescence enhancement of Pr^{3+} doped sol-gel silica glass as a result of Al^{3+} co-doping. *J. Non-Cryst. Solids* **503-504**: 89-93. doi: https://doi.org/10.1016/j.jnoncrysol.2018.09.027

Shaweta Mohan, Simranpreet Kaur, Puneet Kaur, Singh D.P. (2018) Spectroscopic investigations of Sm3+-doped lead alumino-borate glasses containing zinc, lithium and barium oxides. *J. Alloys Compd.* **763**:486-495. doi: https://doi.org/10.1016/j.jallcom.2018.05.319

Liping Wang, Xudong Xu, Xin Yuan (2010) Preparation and photoluminescent properties of doped nanoparticles of ZnS by solid-state reaction. *J. Lumin.* **130**: 137–140. doi: https://doi.org/10.1016/j.jlumin.2009.07.036

Marzouk M.A., Hamdy Y.M., Elbatal H.A., Ezz-Eldin F.M. (2018) Study on the reducing effect of γ-irradiation on Sm^{3+} doped LiAl fluorophosphate glasses through optical, structural and luminescence analysis. *J. Mater Sci. Mater. in Sci* **2**.

Rai V.N., Raja Sekhar B.N., Jagtap B.N. (2012) Study of gamma induced defects in Nd doped Phosphate glass using Uv-Vis Spectrophotometer and photo-physics beamline on Indus-I. *Asian J. Spectrosc.*, special issue, 143-154.

CHAPTER-5
ENERGY TRANSFER STUDY BETWEEN TB^{3+} AND EU^{3+} DOPED ZNS NANOPARTICLE

This chapter focuses on the physical, structural, and energy transfer studies of ZnS NP's co-doped with a fixed amount of Eu^{3+} with changing concentrations of Tb^{3+} and ZnS NP's singly doped with Tb^{3+} ions and Eu^{3+} ions in a silica glass matrix.

5.1 Abstract

A series of singly doped ZnS:Eu, ZnS:Tb, and co-doped ZnS:Tb:Eu have been successfully prepared by the sol-gel method. The various physical properties were calculated. Compression of the glass sample network occurred as a result of ZnS being substituted for SiO_2. The singly doped ZnS:Eu and ZnS:Tb emit red and green light due to the characteristic transitions of 4f-4f transitions of Tb^{3+} and Eu^{3+} ions, respectively. Under excited with Eu^{3+} emission wavelength, there is strong overlap between Eu^{3+} excitation and Tb^{3+} emissions peaks, which clearly manifest the confirmation of possible transfer of energy from Tb^{3+} to Eu^{3+} in ZnS doped silicate glass. The lifetime of the ZnS:Tb and ZnS:Tb:Eu was examined in relation to the energy transfer mechanism and luminescence dynamics. The emission spectra of codoped ZnS:Tb:Eu glass strongly depend on the donor concentration. The color tunability falls within the blueish to purplish region as the Tb^{3+} ion concentration increases for the co-doped ZnS:Tb:Eu sol-gel silica glass matrix.

5.2 Experimental

The following materials were purchased from Sigma-Aldrich: distilled water, tetraethyl orthosilicate (TEOS, 99.9%), methanol (99.9%), Europium (III) nitrate hexahydrate (99.9%), Terbium (III) nitrate hexahydrate, zinc sulphide (99.9%), and HNO_3. Without additional purification, all chemicals and solvents were utilized directly. Sample preparation followed the mechanism highlighted in Chapter-2.

The glass sample under study was coated with 1-bromonaphthalene ($C_{10}H_7Br$) as an adhesive coating, and its refractive index was determined using an Abbe refractometer. Using xylene (C_8H_{10}) as an immersion liquid, the density of the glass sample under study was calculated using the Archimedes principle. PL

excitation, absorption, emission, and decay curve spectra of the glass samples were recorded using F-4700 Fluorescence Spectrometer. FTIR spectra were recorded by IRAffinity-1S (SHI-MADZU).

5.3 Result and Discussions

5.3.1 Physical properties

From the measured values of glass density and refractive indices, another physical property such as Average molecular weight (M_T), Ion's concentration (N_i), Dielectric constant (ε_d), Optical dielectric constant (ε_d-1), Molar volume (V_m), Reflection Losses (R_L), Molar Refractivity (R_M), Energy gap (E_g), Polaron Radius (Rp), Interionic distance (R_i) (Dawngliana *et al.*, 2023), Field strength (F_s), Molar polarizability (α_m) and Metallization Criterion (M_c) were calculated by using appropriate expression (Devi *et al.*, 2019) and represented in Table 5.1. Fig. 5.1 showed the variation of density (ρ) and molar volume (V_m) of ZnS:Tb:Eu doped glass with a fixed concentration of Eu^{3+} ions, ZnS and a varying concentrations of Tb^{3+} ions. The value of molar volume is maximum of 0.5 mol% and minimum for 1.0 mol%. For this specific glass composition, the maximum molar volume for 0.5 mol% indicates an increase in bond length and the interatomic spacing. An increase in the force constant and a shorter bond length of the bonds inside the network (Mohan *et al.*, 2018) can account for the lower value of the molar volume for 1.0 mol%. As ZnS is added in the silica glass, the glass samples become denser due to the higher molecular weight of ZnS (Mw. = 97.07 g/mol) compared to SiO_2 (Mw. = 60.08 g/mol). The ionic distance between Zn-S and Si-O is 1.62 Å and 2.54 Å, respectively. This suggests that the compression of the glass sample network occurred as a result of ZnS being substituted for SiO_2. Fig. 5.2 demonstrated the variation of polaron radius and field strength of ZnS:Tb:Eu doped with varying concentrations of Tb^{3+} ions and a fixed concentration of Eu^{3+} ions and ZnS nanoparticles. The polaron radius decreases as the concentration of Tb^{3+} ion increases since the increase in Tb^{3+} ion concentration (Ni), which results in high field strength, could be the cause of this decline. The electronic polarizability (α_e) which controls the non-linear dynamic of the materials, was derived by using Volt Lorentz-Lorentz theory (Yasi *et al.*, 1982; Haralampieva *et al.*, 2012) as follows:

$$\frac{(n^2-1)}{(n^2+1)} V_m = \frac{4}{3\pi} N\alpha_e \quad (5.1)$$

Where N is Avogadro's number, V_m is molar volume and *n* is refractive index.

Table 5.1: Various physical properties ZnS:Tb:Eu in sol-gel silicate glass.

Physical properties	**0.5 % Eu^{3+}:1.0 % ZnS: *x* mol % Tb^{3+}**		
	***x* = 0.5 %**	***x* = 0.75 %**	***x* = 1.0 %**
Refractive index (n_i)	1.42	1.44	1.47
Density (ρ) (g/cm^3)	1.09	1.13	1.24
Thickness (Z_t)	0.187	0.191	0.194
Average molecular weight M_T (g)	64.17	65.10	66.04
Ion's concentration (N_i x 10^{20})	2.55	0.59	1.14
Dielectric constant (ε_d)	2.02	2.07	2.16
Optical dielectric constant (ε_d-1)	1.02	1.07	1.16
Molar volume (V_m) (cm^3/mol)	58.87	57.61	53.26
Reflection Losses (R_L)	0.015	0.016	0.018
Molar Refractivity (R_M)	19.88	20.08	19.55
Energy gap (E_g)	8.77	8.49	8.01
Polaron Radius (Rp x 10^{-8}) (cm^{-3})	0.22	0.05	0.20
Interionic distance (R_i x 10^{-7}) (cm^{-3})	1.31	5.65	2.90
Electronic polarizability (α_e x 10^{21})	1.00	1.04	1.11
Field strength (F_s x 10^{13})	38.56	76.13	48.71
Molar polarizability (α_m)	7.88	7.97	7.76
Metallization Criterion (M_c)	0.66	0.65	0.63

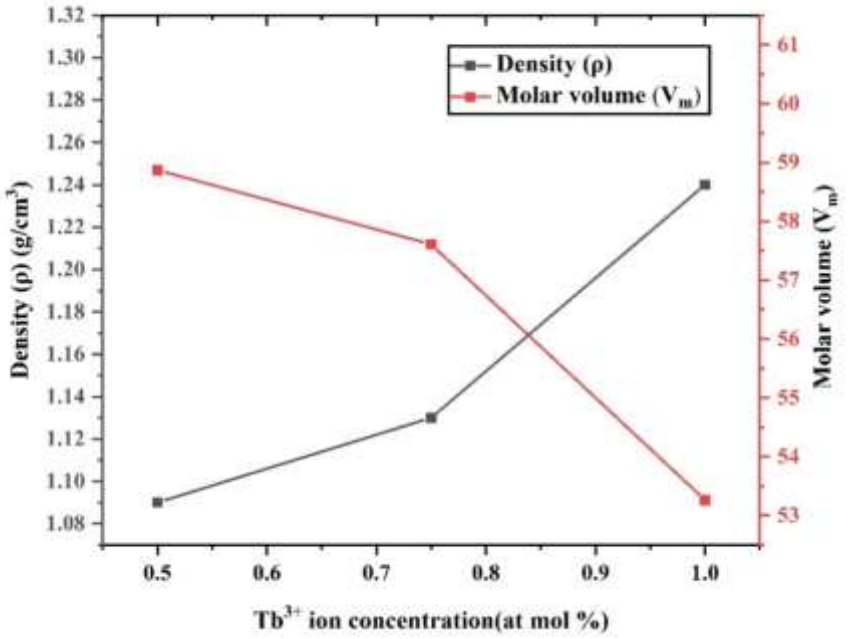

Fig. 5.1: Change in density (ρ) and molar volume (V_m) of ZnS:Tb:Eu doped silica glass with varying concentration of Tb^{3+} ion.

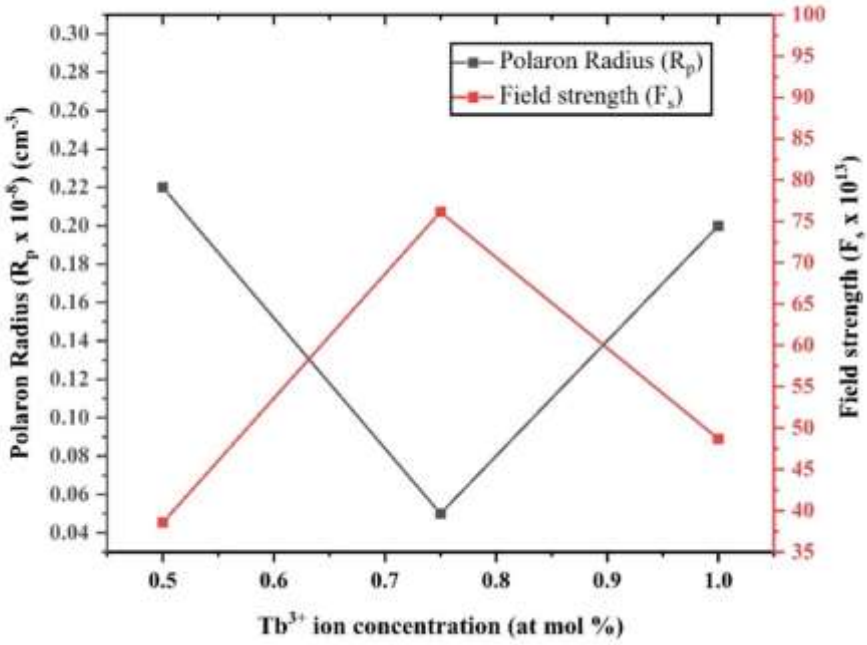

Fig. 5.2: Change in polaron radius (Rp) and field strength (F_s) of ZnS:Tb:Eu doped silica glass with varying concentration of Tb^{3+} ion.

5.3.2 FTIR Spectra

Fig. 5.3 shows the FTIR spectra of ZnS:Tb:Eu in silica glass matrix annealed at 950^0 C. The spectra were recorded between 500 cm^{-1} to 4000 cm^{-1}. There is a substantial amount of water and other organic material in the gel stage sample. The obtained sample is heated incrementally in an electric muffle furnace, which gradually extracts different chemicals from the gel matrix and contributes to the formation of a robust glassy network. Bands at 794 cm^{-1} are caused by the ZnS vibration, while bands at 1072 cm^{-1} are caused by the stretching of Si-O-Si (Kong *et al.*, 2017). Bands at around 1512 cm^{-1} and 1597 cm^{-1} are influenced (Li *et al.*, 2022) by the doped Tb^{3+} and Eu^{3+} in the glass matrix. The sample absorbs CO_2 which results in bands at around 1751 cm^{-1} that is C-O vibrational modes. O-H stretching is associated with bands at about 3732 cm^{-1} that gradually vanish, indicating that annealing removes the O-H vibrations.

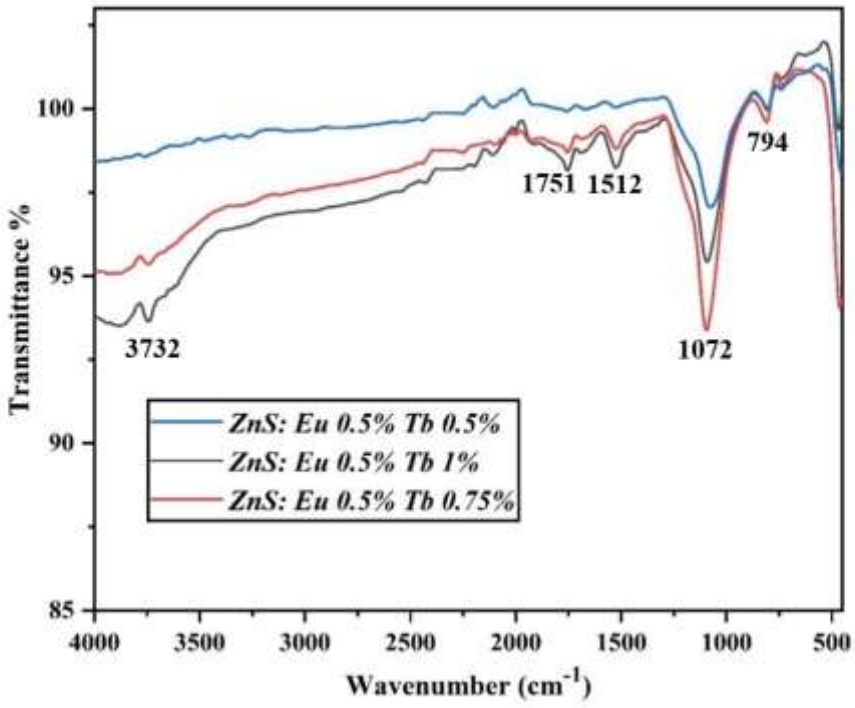

Fig. 5.3: FTIR spectra of ZnS:Tb:Eu doped silicate glass.

5.3.3 PL of ZnS:Eu doped glass

The PL excitation and emission spectra of ZnS (1 mol %) and Eu (0.5 mol %) doped silicate glass matrix is shown in Figs. 5.4(a) and 5.4(b). Fig. 5.4(a) shows the excitation spectrum monitored at 613 nm, which shows a sharp peak from 230 to 580 nm due to the transition of $^7F_0 \rightarrow {}^5D_4$ (361 nm), $^7F_0 \rightarrow {}^5G_2$ (379 nm), $^7F_0 \rightarrow {}^5L_6$ (392 nm), $^7F_0 \rightarrow {}^5D_3$ (413 nm), $^7F_0 \rightarrow {}^5D_2$ (462 nm), and $^7F_0 \rightarrow {}^5D_1$ (530 nm). Two prominent peaks were observed at 391 nm and 553 nm, which indicates that this glass could be excited by the near UV (UVA) light and green light (Som *et al.*, 2014), which may find applications in solid-state lighting devices. The PL spectra (Fig. 5.4(b)) consist of four broad peaks appear at 578 nm, 593 nm, 613 nm, 653 nm, and 703 nm which correspond to transitions of $^5D_0 \rightarrow {}^7F_0$, $^5D_0 \rightarrow {}^7F_1$, $^5D_0 \rightarrow {}^7F_2$, $^5D_0 \rightarrow {}^7F_3$, and $^5D_0 \rightarrow {}^7F_4$ respectively. All assignments of transition bands are done with lanthanide spectra transition reported by Dieke and Carnal et al. The emission at around 578 nm and 593 nm may be assigned to a magnetic-dipole allowed transition which obeys the selection rule $\Delta J = 1$ (Suthanthirakumar *et al.*, 2018), which is independent of the local environment of the host lattice. $^5D_0 \rightarrow {}^7F_0$ transition is also used for determining the environment in which the Eu^{3+} ions are bonded. The emission bands correspond to $^5D_0 \rightarrow {}^7F_2$ (613 nm), $^5D_0 \rightarrow {}^7F_3$ (653 nm), and $^5D_0 \rightarrow {}^7F_4$ (703 nm) were a transition enabled by an electric dipole, and its intensity is hypersensitive to the variation of the bonding environment of the Eu^{3+} ions. The main causes of electric dipole transitions are the lack of a centre of symmetry and the mixing of $4f^5$ orbitals with the opposite parity orbital (Kumaresh *et al.*,2016). These transitions appear due to a charge imbalance between Zn^{2+} and Eu^{3+} ions. Here, the electric-dipole transition $^5D_0 \rightarrow {}^7F_2$ (613 nm) is more dominant than the magnetic dipole transition $^5D_0 \rightarrow {}^7F_1$ (593 nm), indicating that the majority of Eu^{3+} is located at the non-inversion symmetry center (Yu *et al.*, 2007) in ZnS. It is also stated that the ratio between that integrated emission intensity of $^5D_0 \rightarrow {}^7F_1$ and $^5D_0 \rightarrow {}^7F_2$ transitions, known as the asymetric ratio $(R/O)^{12}$, can be used as a local crystal field probe to measure the nature of the local Eu^{3+} surroundings (Som *et al.*, 2014). Consequently, this ratio represents the extent of distortion from the Eu^{3+} ion local environment's inversion symmetry. The calculated assymetric value is 2.64, this value is very small and does not significantly affect the direction of R/O of Eu^{3+}. This provides compelling evidence that the Eu^{3+}

ions primarily occupy the lattice site without inversion symmetry. To examine the color coordinate and CCT value, the chromaticity diagram was also plotted, and it is shown in the inset of Fig. 5.4(b). The calculated color coordinate value was X= 0.328046 and Y= 0.280999, which falls within the red region, the CCT value was 5808 K, which provides that light appears ‘cool’.

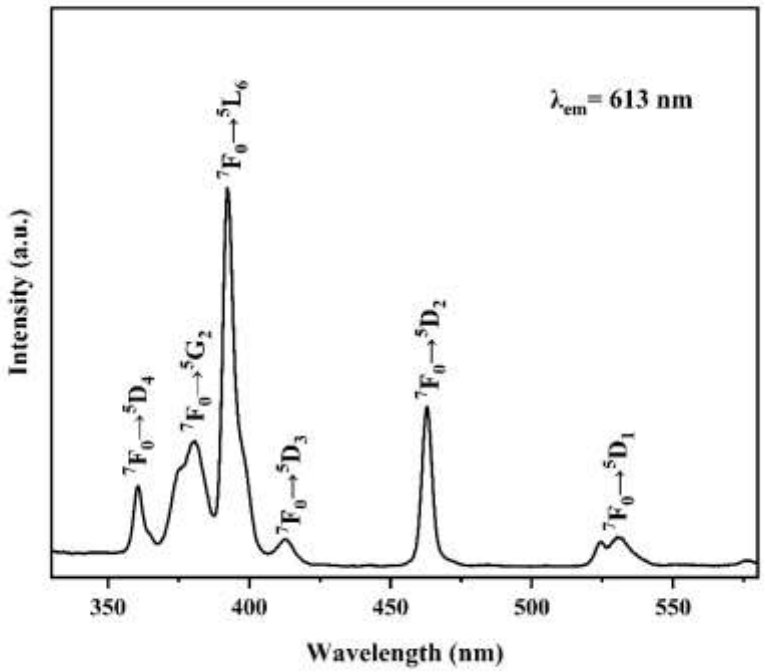

Fig. 5.4(a): Excitation spectra of ZnS:Eu (0.5%) doped glass matrix at λ_{em}= 613 nm

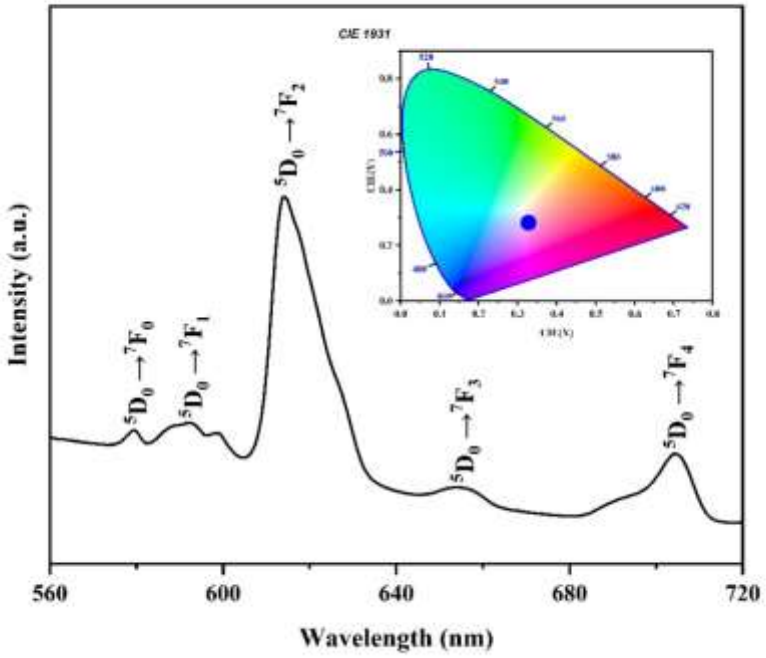

Fig. 5.4(b): Emission spectra and CIE Chromaticity of ZnS:Eu(0.5%) doped glass matrix at λ_{ex}= 370 nm

5.3.4 PL of ZnS:Tb doped glass

Fig. 5.5(a) shows the excitation spectrum of Tb^{3+}(0.5 mol %) co-doped ZnS (1 mol %) nanoparticles in silicate glass when monitored at 545 nm, which reveals several prominent peaks between 200 and 500 nm due to the transitions of ground state $^7F_6$ to the different excited states of Tb^{3+} i.e., at 317 nm ($^5D_0$), 325 nm ($^5H_7$), 340 nm ($^5G_2$), 351 nm ($^5L_9$), 367 nm ($^5L_{10}$), 378 nm ($^5D_3$) and 486 nm ($^5D_4$) respectively (Som *et al.*, 2014). The emission spectra (Fig. 5.5(b)) show four strong emission peaks at 488 nm, 545 nm, 586 nm, and 623nm due to the transitions of $^5D_4 \rightarrow {}^7F_6$, $^5D_4 \rightarrow {}^7F_5$, $^5D_4 \rightarrow {}^7F_4$ and $^5D_4 \rightarrow {}^7F_3$ respectively. As expected, the transition from $^5D_4 \rightarrow {}^7F_5$ (green emission) is the most intense and has the highest affinity for both electric-dipole and magnetic-dipole-induced transitions (Kasturi *et al.*, 2018). It is also sensitive to the nature of the surrounding atoms. No emission was observed from higher level of $^5D_3$ due to the cross-relaxation effect. The CIE coordinates for this glass are X= 0.274359 and Y= 0.462343, which corresponds to green light.

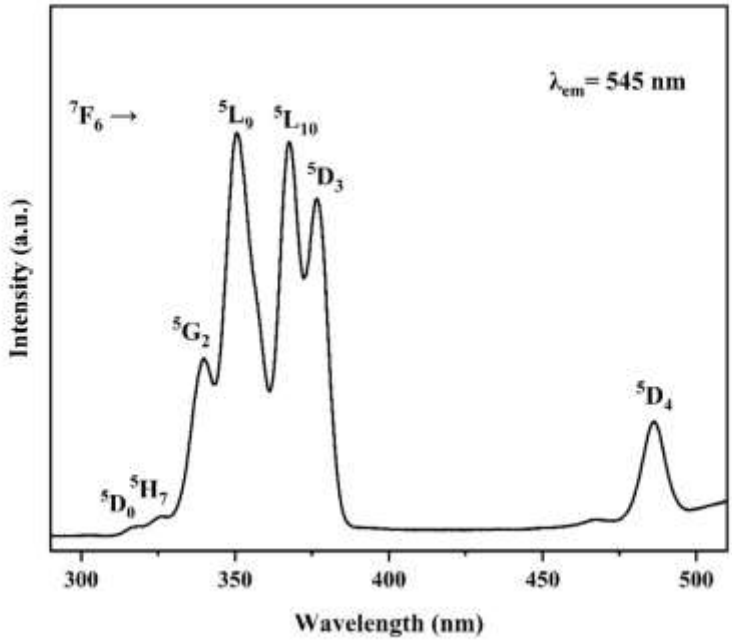

Fig. 5.5(a): Excitation spectra of ZnS:Tb(0.5%) doped glass matrix at λ_{em}= 545 nm

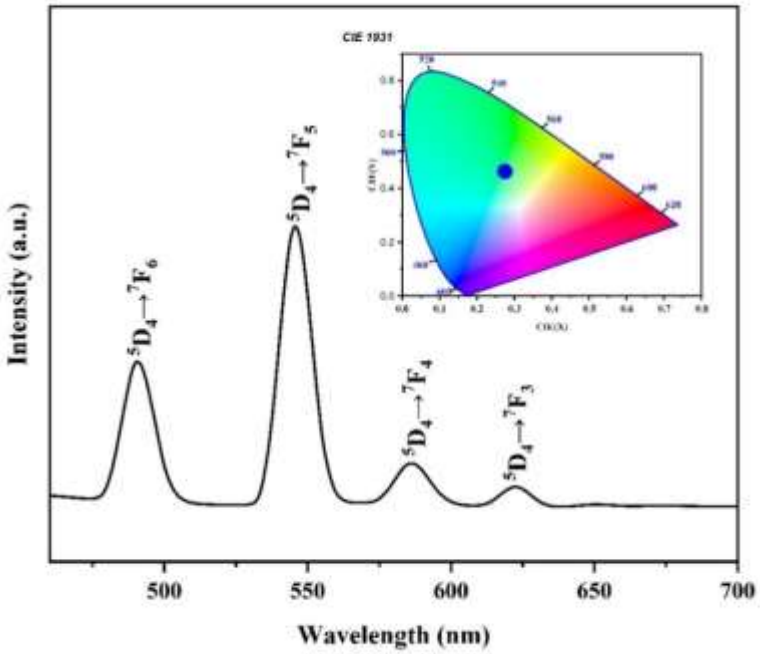

Fig. 5.5(b): Emission spectra and CIE chromaticity of ZnS:Tb(0.5%) doped glass matrix at λ_{ex}= 370 nm.

5.3.5 PL of ZnS:Tb:Eu doped glass

Energy transfer from a donor to an acceptor can be confirmed by if we detect the donor's excitation peak by monitoring the acceptor's emission. Fig. 5.6 shows only Tb^{3+} excitation peaks and no extra Eu^{3+} excitation peaks were observed when monitoring the 545 nm Tb^{3+} emission. This suggest there is no transfer of energy from Eu^{3+} to the Tb^{3+} ion. This is expected as there is no energy level of Tb^{3+} resonant with the metastable $^5D_0$ state of Eu^{3+}. The excitation spectrum of ZnS:Tb:Eu doped glass by monitoring of Eu^{3+} emission at 613 nm is shown in Fig. 5.6. The spectrum reveals new prominent peaks different from ZnS:Eu, Fig. 5.4(a), because of the combination of spin allowed/spin forbidden ($4f^8 \rightarrow 4f^7 5d^1$) of Tb^{3+} and $O^{2-} \rightarrow Eu^{3+}$ charge transfer band of the Eu^{3+} ion. Because of this, several peaks were observed at 303 and 317nm due to the $^7F_6 \rightarrow {}^5H_6$, $^7F_6 \rightarrow {}^5D_0$ transitions of Tb^{3+} and at 361, 379, 392, 413, 462, and 530 nm due to $^7F_0 \rightarrow {}^7D_4$, $^7F_0 \rightarrow {}^5G_2$, $^7F_0 \rightarrow {}^5L_6$,$^7F_0 \rightarrow {}^5D_3$, ,$^7F_0 \rightarrow {}^5D_2$ and $^7F_0 \rightarrow {}^5D_1$ transitions of Eu^{3+}, respectively. Therefore, it is evident that the co-doped ZnS doped glass excitation spectrum contains every characteristic of the single-doped ZnS:Tb and ZnS:Eu glass. When the co-doped excitation spectrum is compared to the single doped glasses, the two match precisely in terms of spectrum summation (shown in Figs. 5.4(a) and 5.5(a). Consequently, energy transfer from the Tb^{3+} to Eu^{3+} ions is clearly demonstrated by the presence of the Tb^{3+} (Zhu *et al.*, 2017) excitation peaks among the various photo-stimulation paths for the activation of the Eu^{3+} (613 nm) $^5D_0 \rightarrow {}^7F_2$ transition. The Eu^{3+} excitation spectra and Tb^{3+} emission is also highlighted for direct comparison, as shown in Fig. 5.7. Fig. 5.7 reveals that there is strong overlap between Eu^{3+} excitation peaks $^7F_0 \rightarrow {}^5D_2$ (462 nm), $^7F_0 \rightarrow {}^5D_1$ (530 nm), and Tb^{3+} emissions peaks $^5D_4 \rightarrow {}^7F_6$ (488 nm), $^5D_4 \rightarrow {}^7F_5$ (545 nm), and $^5D_4 \rightarrow {}^7F_4$ (586 nm), respectively clearly manifest the confirmation of possible transfer of energy from Tb^{3+} to Eu^{3+} in ZnS doped silicate glass. In the excitation spectra energy transfer from the host ZnS to Eu^{3+} and Tb^{3+} is possible. The presence of strong excitation bands in the excitation spectra of Eu^{3+} and Tb^{3+} indicates that ET occurs probably from SiO_2 in the ZnS host matrix to Eu^{3+} and Tb^{3+} because there exist some f-f transitions in the excitation line for Eu^{3+}, $^5D_0 \rightarrow {}^7F_J$ and Tb^{3+}, $^5D_4 \rightarrow {}^7F_J$.

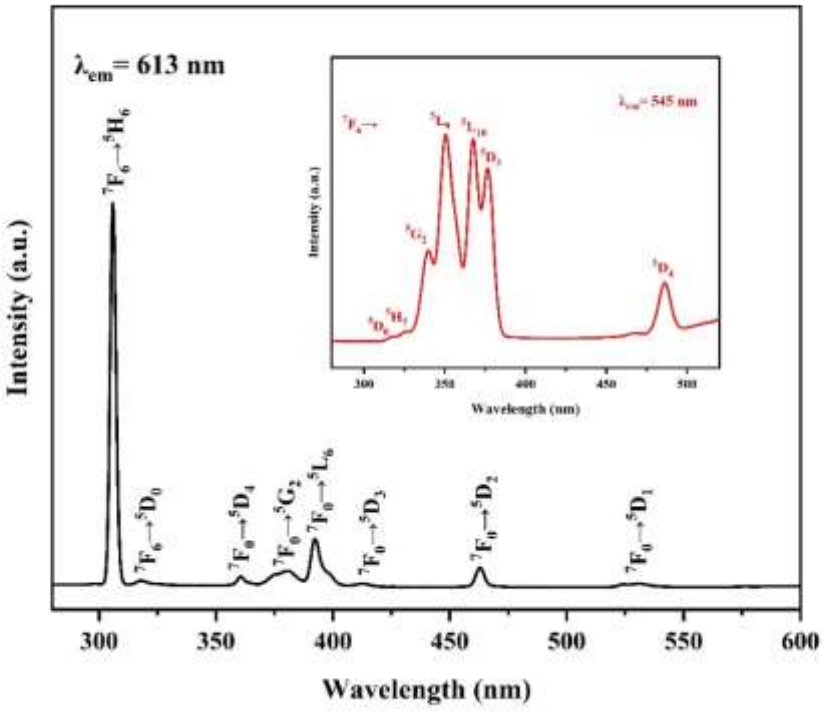

Fig 5.6: Excitation spectra of ZnS:Tb:Eu doped silicate glass at λ_{em}= 613 nm and λ_{em}= 545 nm.

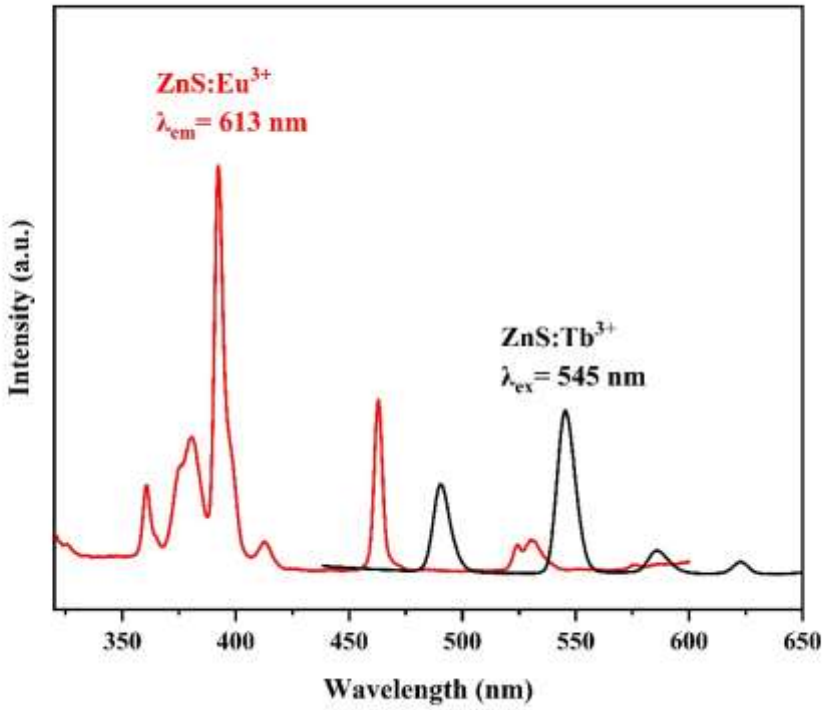

Fig. 5.7: Spectral overlap between Eu^{3+} excitation and Tb^{3+} emission in ZnS doped silicate glass.

To know the emission colour tunability and effect of concentration on the luminescence properties of ZnS:Tb:Eu doped silicate glass. Different concentrations of Tb^{3+} doped with a fixed concentration of Eu^{3+} (0.5 mol %) and ZnS (1 mol %) are prepared and their emission intensity is shown in Fig. 5.8. In the spectra, we can observe both the sharp characteristic peaks of Tb^{3+} and Eu^{3+}. The bands observed at 418 nm, 436 nm, 450 nm, 467 nm, 485 nm, and 545 nm are due to the transitions of $^5D_3 \rightarrow {}^7F_5$, $^5D_3 \rightarrow {}^7F_4$, $^5D_3 \rightarrow {}^7F_3$, $^5D_3 \rightarrow {}^7F_2$, $^5D_4 \rightarrow {}^7F_6$, $^5D_4 \rightarrow {}^7F_5$ of Tb^{3+} ions respectively. In addition, the bands observed at 593 nm, 613 nm, and 653 nm are due to $^5D_0 \rightarrow {}^7F_1$, $^5D_0 \rightarrow {}^7F_2$ and $^5D_0 \rightarrow {}^7F_3$ transitions of Eu^{3+} ions respectively. Because of the concentration quenching, the emission intensity of Tb^{3+} increases first and then deceases with the increases in Tb^{3+} content. A decrease in the intensity of the Tb^{3+} peak and a gradual increase in the Eu^{3+} emission intensity peak (613 nm) with the addition of Tb^{3+} content occur when the Eu^{3+} concentration remains constant at

0.5%. This suggests that the energy transfer from Tb^{3+} to the Eu^{3+} ion sensitizes the emission of Eu^{3+} ions (Zhu *et al.*, 2017). The sensitization effect between Tb^{3+} and Eu^{3+} in ZnS doped glass was investigated using the optimal concentration (highest intensity peaks) from Fig. 5.8. However, its intensity decreases when the Tb^{3+} content exceeds 0.75%, which can be assigned to the concentration quenching effect. We know that the symmetry position of Eu^{3+} affects the emission intensity of $^5D_0 \rightarrow {}^7F_1$ (593 nm) and $^5D_0 \rightarrow {}^7F_2$ (613 nm). The Eu^{3+} holds the strongest peak at 613 nm, which means most of the Eu^{3+} is located at a non-inversion symmetry center in ZnS.

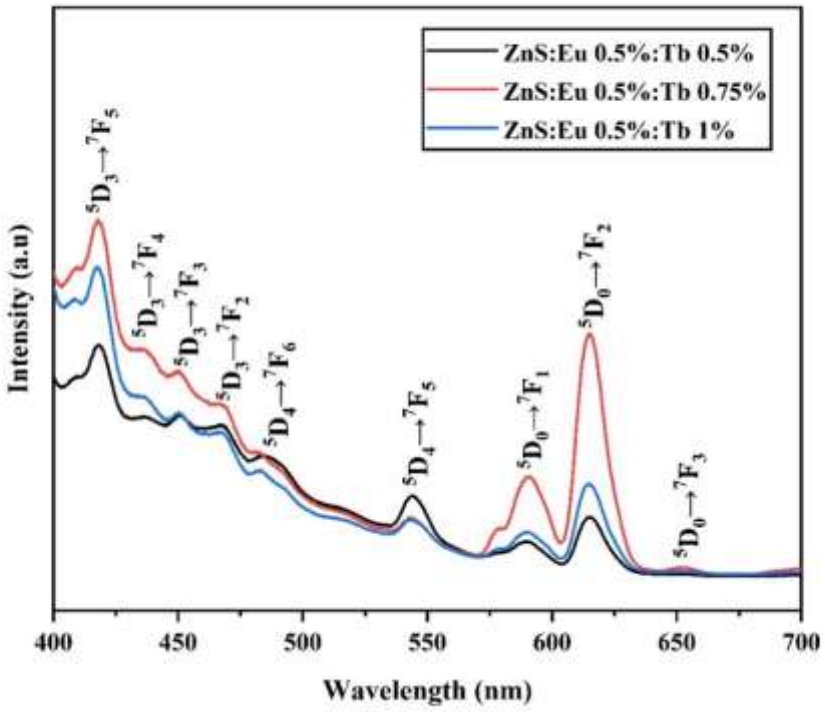

Fig 5.8: Emission spectra of ZnS:Tb:Eu doped silicate glass.

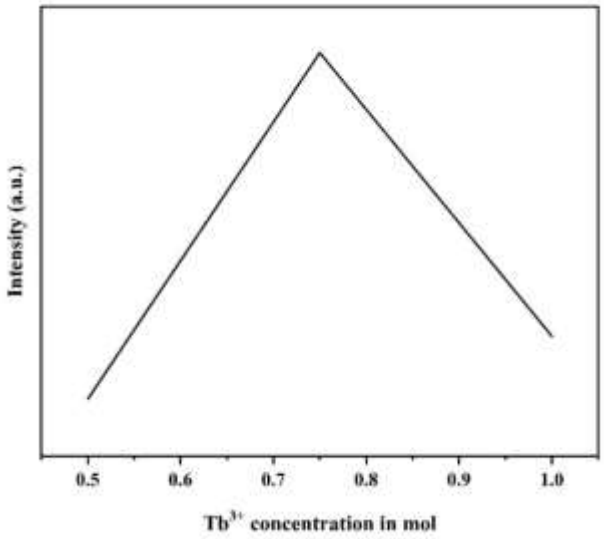

Fig. 5.9: Dependence of emission intensity on the Tb^{3+} concentration in ZnS:Tb:Eu silica glass.

5.3.6 Energy Transfer Mechanism

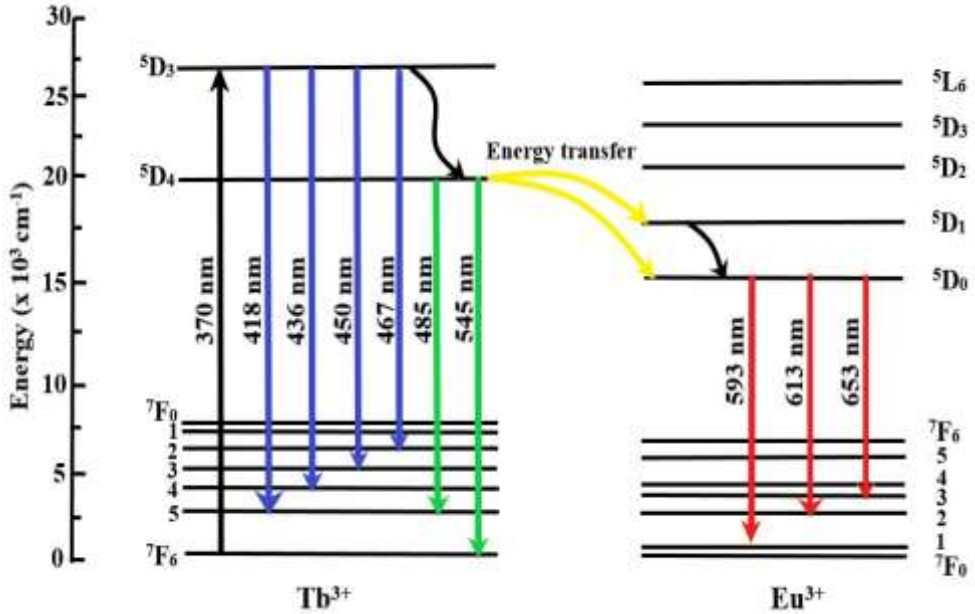

Fig. 5.10: Schematic energy level showing the possible energy transfer between Tb^{3+} and Eu^{3+} ion in ZnS:Tb:Eu doped silicate glass.

Fig. 5.10 represents the schematic energy level showing the possible energy transfer from Tb^{3+} to Eu^{3+} ions in ZnS:Tb:Eu doped sol-gel silica glass under excited with an UV light source with wavelength λ_{ex} = 370 nm. Under excited with λ_{ex} = 370 nm, different concentrations of Tb^{3+} ions absorbed energy and excited to higher energy level $^5D_3$ through non-radiative transitions. From $^5D_3$ most of the electrons were de-excited to ground level ($^7F_5$, $^7F_4$, $^7F_3$, $^7F_2$) of the Tb^{3+} ion through radiative transitions to emit blue light. While the rest of the excited electrons were relaxed to lower energy level $^5D_4$ through multi phonon relaxation (Bedyal *et al.*, 2019) and then to the ground level ($^7F_6$, $^7F_5$) of the Tb^{3+} ion to emit green light. Therefore, when Eu^{3+} ions are introduced in the same host matrix, some of the Tb^{3+} ions (Dhaterwal *et al.*, 2024) rather than being de-excited to the ground state also transfer their energy to the $^5D_0$ and $^5D_1$ energy levels of Eu^{3+} ions through various cross relaxation (Liu *et al.*, 2014) channels, as it is evident that there is a spectral overlap between the Eu^{3+} excitation and Tb^{3+} emission peaks. When receiving the energy, the Eu^{3+} ions then de-excited to the ground levels ($^7F_1$, $^7F_2$, $^7F_3$) to release red light. Therefore, on exciting with an UV light, Tb^{3+} ions not only emit green light but also transfer their energy to Eu^{3+} ions to emit red light (Li *et al.*, 2017).

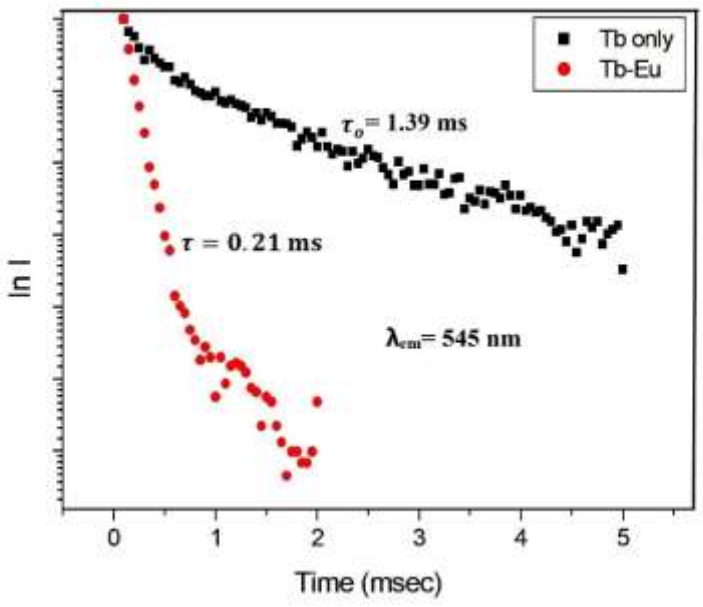

Fig. 5.11: Decay curve of ZnS:Tb(0.5%) and ZnS:Tb(0.5%):Eu(0.5%) doped silica glass.

To comprehend the specific mechanism underlying the process of energy transfer. The normalized decay curves of ZnS:Tb(0.5%) and ZnS:Tb(0.5%):Eu(0.5%) were examined and displayed in Fig. 5.11. The curve clearly shows that the emission decays more quickly with the presence of Eu^{3+} ion. The measured lifetime can be fitted to a single exponential for lower concentrations but not for higher concentrations. Therefore, the lifetime was calculated by using the relation.

$$\tau_{exp} = \int \frac{t\, I(t)dt}{I(t)dt} \tag{5.2}$$

The calculated values for average lifetime (τ) for ZnS: Tb were 1.39 ms and for ZnS: Tb: Eu were 0.21 ms, respectively. The drop in τ values further indicates that the addition of Eu^{3+} ions cause the decay to more accelerate, which also implies the occurrence of energy transfer from Tb^{3+} to Eu^{3+} ions.

The probability of energy transfer from Tb^{3+} to Eu^{3+} ions was determined by the equation

$$P_{Tb\rightarrow Eu} = \left(\frac{1}{\tau}\right) - \left(\frac{1}{\tau_o}\right) \tag{5.3}$$

Where τ_o and τ are the lifetime of the Tb^{3+} ions in the absence and presence of Eu^{3+} ions for the same concentration. The value of energy transfer probability was calculated as 40.41%.

Additionally, the general equation used to approximate the energy transfer efficiency from Tb^{3+} to Eu^{3+} ions is given by

$$\eta_{Tb\rightarrow Eu} = 1 - \left(\frac{\tau}{\tau_o}\right) \tag{5.4}$$

The value of energy transfer efficiency was calculated as ≈ 84.9 %. The energy transfer between Tb^{3+} and Eu^{3+} typically occurs through a process known as resonant energy transfer. The high value of energy transfer eifficiency indicates a very efficient energy transfer process. This means that a substantial portion of the energy absorbed by Tb^{3+} ions is successfully transferred to Eu^{3+} ions, which can then emit light at a different wavelength. The high efficiency of energy transfer also leads to enhanced luminescent properties in the material. The Eu^{3+} ions, upon receiving energy from Tb^{3+}, can emit light in the red region of the spectrum, which is often

desirable in phosphor applications. In dosimetry systems, this efficient energy transfer can improve the sensitivity and accuracy of radiation detection, as the emitted light can be measured to determine radiation exposure levels.

The energy transfer between the donor ion and acceptor ion can mainly take place by two different mechanisms

(i) exchange interaction, which is only achievable when the donor and acceptor orbits overlap and the critical energy transfer distance is between 1 and 4 Å.

(ii) multipolar interaction

Blaise formula estimated the critical energy distance between the donor and acceptor ions as

$$R_c \approx 2\left[\frac{3V}{4\pi X_c N}\right]^{1/3} \quad (5.5)$$

Where V is the volume, N is the number of cations in the unit cell, X_c is the total concentration of Tb^{3+} and Eu^{3+}, for which the energy transfer efficiency is 50%.

Bedyal *et al*. (2019), Rawat *et al*. (2022) and Luo *et al*. (2019) studied that the Tb^{3+} and Eu^{3+} co-doped with $NaSrBO_3$, $Ca_2Ga_2SiO_7$, and $LaPO_4$ phosphor. They showed that the values of R_c are 11.94 Å,15.86 Å and 18.16 Å respectively, which is greater than 5 Å, confirming that the possible energy transfer mechanism (Liu *et al.*, 2023) between them is multipolar interaction with dipole-dipole interaction in nature, as the best linear relationship was found for n=6. Multipolar interaction with the value of n=8, which is dipole-quadrupole interaction for co-doped with $YTaO_4$ and $Sr_3B_2O_6$ phosphors, was confirmed by Nan *et al*. (2020) and Tuyen *et al*. (2017). For co-doped with Gd_2O_3 phosphors, Dong Zhu *et al*. (2019) suggest that the process of ET is multipolar in nature with quadrupole-quadrupole electronic interaction as n=10.

However, there is not much information on the detailed mechanism of the energy transfer process from Tb^{3+} to Eu^{3+} ion co-doped silicate glasses for different hosts. The Tb^{3+} and Eu^{3+} co-doped with zinc aluminoborosilicate, and lead borate, metaphosphate, aluminosilicate, zinc phosphate glass was studied by Zheng *et al.* (2020), Pisarska *et al.* (2014), Said *et al.* (2019), and Zhu *et al.* (2013), Caldino *et al.* (2013); they all confirmed that the Tb^{3+} transferred energy to the Eu^{3+} ion via multipolar interaction. Zheng *et al.* (2020) investigated that quadrupole-quadrupole

interaction was a dominant mechanism for doped zinc aluminoborosilicate glass; Caldino *et al.* (2013) stated that for zinc phosphate glass, dipole-dipole interaction was a dominant mechanism while no detail information on transfer mechanism was found for lead borate, metaphosphate, and aluminosilicate glass. For our studied sample ZnS:Tb:Eu, the value of R_c was calculated as 7.26 Å, which is greater than 5 Å, confirming that the possible energy transfer mechanism between them is multipolar interaction. By utilizing the highest intensity peak from ZnS:Tb:Eu doped silica glass, i.e., Tb^{3+}(0.75%) and Eu^{3+}(0.5%) we were estimating the nature of the energy transfer mechanism, whether it is dipole-dipole, dipole-quadrupole, or quadrupole-quadrupole electronic interaction in detail.

Table 5.2: Comparison of Tb^{3+} and Eu^{3+} co-doped R_c values in different hosts.

Host	R_c values	Nature of interaction
(ZnS)Present work	7.26 Å	Multipolar
$NaSrBO_3$	11.94 Å	Multipolar
$Ca_2Ga_2SiO_7$	15.86 Å	Multipolar
$LaPO_4$	18.16 Å	Multipolar
$Sr_3B_2O_6$	19.9 Å	Multipolar

The detailed expression for the energy transfer process was given by the Reisfeld approximation and Dexter's energy transfer formula as

$$\frac{\eta_0}{\eta} = x^{n/3} \tag{5.6}$$

x is the sum of molar concentrations of Tb^{3+} and Eu^{3+}, η_0 and η are the quantum efficiencies of Tb^{3+} in the presence and absence of Eu^{3+}, respectively. The *n* values denote dipole-dipole interaction (for *n*=6), dipole-quadrupole interaction (for *n*=8) and quadrupole-quadrupole interaction (for *n*=10) (Jeon *et al.*, 2001). Furthermore, the values of η_0 and η can be replaced by their respective intensities, I_o and I respectively. Therefore, the above equation reduces to

$$\frac{I_0}{I} = x^{n/3} \tag{5.7}$$

where I and I_o are the intensities of Tb^{3+} in the presence and absence of the Eu^{3+} ion respectively (Qian *et al.*, 2023).

Forster, alternatively, defined and related the transfer eifficiency (η_T) to a change in the fluorescence yields in the presence and absence of acceptor as,

$$\eta_T = 1 - \frac{\eta}{\eta_o} = 1 - \frac{I}{I_o} \quad (5.8)$$

And, the nonradiative transition probability (P_{da}) for donor-acceptor concentration may be computed as

$$P_{da} = \frac{1}{\tau_o}\left(\frac{\eta_0}{\eta} - 1\right) \quad (5.9)$$

Where, τ_o is the radiative lifetime of donor in the absence of acceptor which is found to be 1.39 ms, shown in the Fig. 5.11, and this value is used in this calcalculation.

With eqns (5.8) and (5.9), the transfer efficiency (η_T), fluorescence yield ratio ($\frac{\eta}{\eta_o}$) and transition probability (P_{da}) between Tb^{3+} and Eu^{3+} at different concentration of Tb^{3+} in ZnS:Tb:Eu doped sol-gel silica glasses at 370 nm excitation was calculated and compile in the Table 5.3.

Table 5.3: Transfer efficiency (η_T), fluorescence yield ratio ($\frac{\eta}{\eta_o}$) and ET probability (P_{da}) between Tb^{3+} and Eu^{3+} at different concentration of Tb^{3+} in ZnS:Tb:Eu doped sol-gel silica glasses for the $^5D_4 \rightarrow {}^7F_5$ transition of Tb^{3+} at 370 nm excitation.

Conc. of Eu^{3+} (C_{Eu}) (Mol %)	Conc. of Tb^{3+} (C_{Tb}) (Mol %)	$(C_{Eu} + C_{Tb})^2$	$\frac{\eta}{\eta_o}$	η_T	(P_{da}) (s^{-1})
0.5	0.5	1	0.056	0.944	12127.34
0.5	0.75	1.56	0.046	0.954	15266.19
0.5	1	2.25	0.040	0.960	17266.19

ET probability (P_{da}) and relative fluorescence yield ($\frac{\eta_0}{\eta}$) variation with the square of the donor and acceptor concentration $(C_{Eu} + C_{Tb})^2$ are studied and shown in Fig. 5.12 and 5.13, respectively. Their linear behaviour confirming that the transfer rate is propotional to the inverse sixth power of donor-acceptor distance suggesting the involvement of dipole-dipole interaction in ET mechanism.

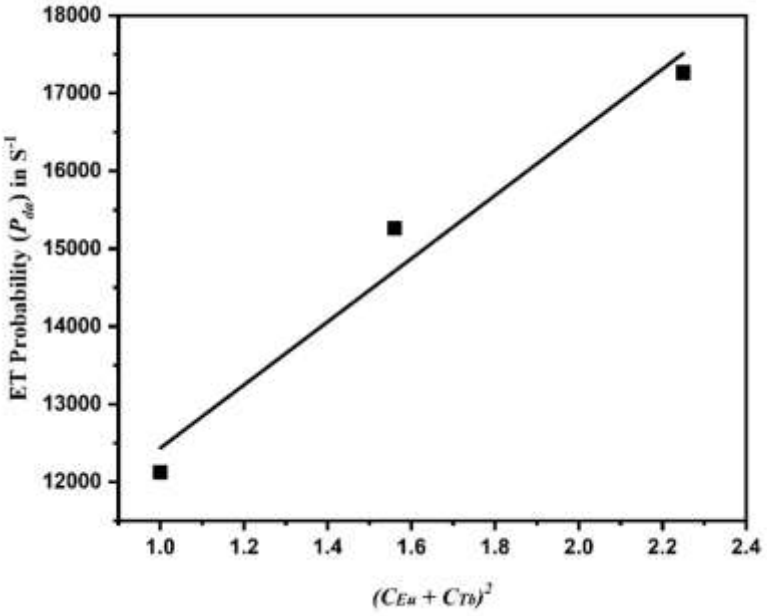

Fig. 5.12: Variation of ET probability (P_{da}) with square of donor-acceptor concentration $(C_{Eu} + C_{Tb})^2$.

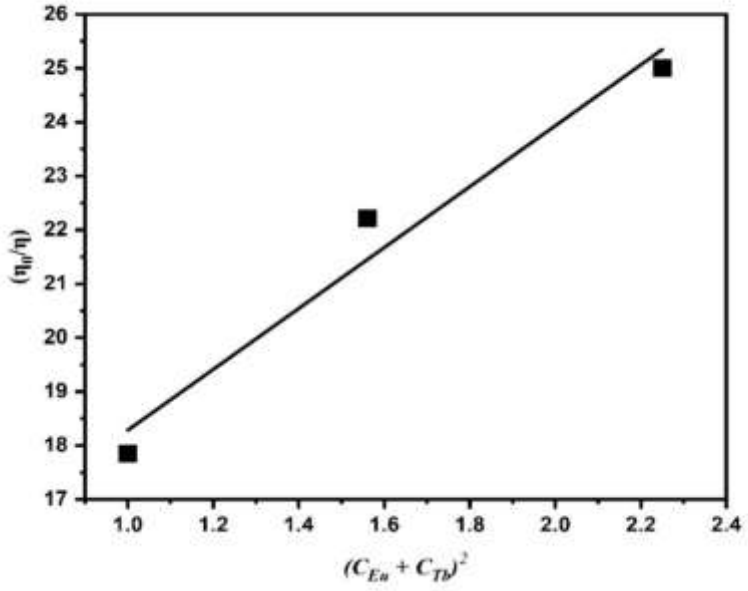

Fig. 5.13: Variation of relative fluorescence yield $(\frac{\eta_0}{\eta})$ with square of donor-acceptor concentration $(C_{Eu} + C_{Tb})^2$.

In addition, eqn (5.7) is used to plot the graph between $\frac{I_0}{I}$ and $x^{n/3}$ for different values of n as depicted in Fig. 5.13. As the value of R^2 approaches 1 for n = 6, the plot exhibits a good linear relationship that suggest that the dipole-dipole interaction is the more prominent mechanism for multi-polar interaction in the current system, accounting for the energy transfer from Tb^{3+} to Eu^{3+} ions.

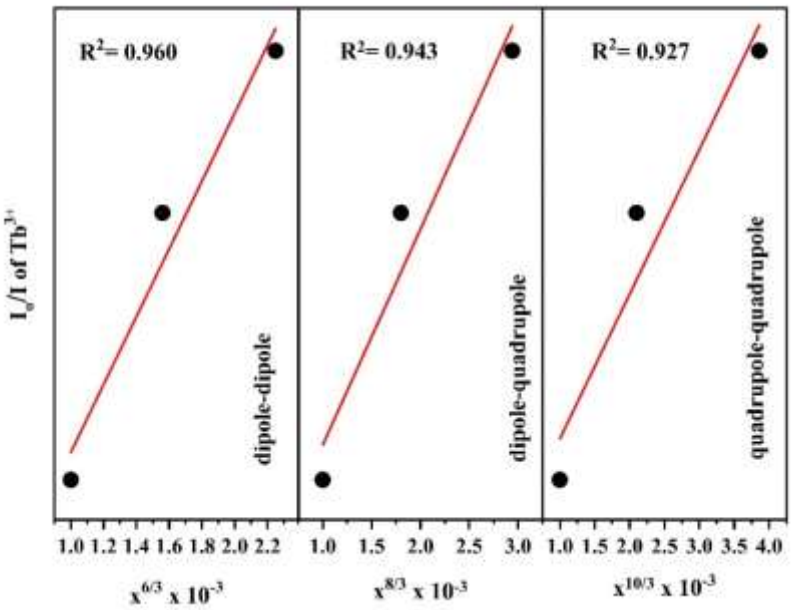

Fig. 5.14: Plot of $\frac{I_0}{I}$ vrs $x^{n/3}$ for different values of n, the linear fits are shown by the red solid lines.

Table 5.4: Variation of $x^{n/3}$ values for different concentrations

Different concentrations	$x^{6/3}$	$x^{8/3}$	$x^{10/3}$	I_o/I
ZnS:Eu 0.5%:Tb 0.5%	1	1	1	2.84
ZnS:Eu 0.5%:Tb 0.75%	1.56	1.8	2.1	3.51
ZnS:Eu 0.5%:Tb 1%	2.25	2.94	3.86	4.35

Vai Uitert's stated that the nature of multipolar interaction demonstrating the energy transfer can be confirmed by examine the effect of acceptor (Eu^{3+}) concentration on the emission intensity of the donor (Tb^{3+}) ion. The formula for this is

$$\frac{I}{I_o} = \left[1 + \beta \left(\frac{x}{x_o}\right)^{n/3}\right]^{-1} \quad (5.10)$$

The concentration and critical transfer concentration are represented by x and x_o respectively. Depending on the type of interaction, n = 6, 8, and 10 correspond to the dipole–dipole, dipole–quadrupole, and quadruple–quadrupole interactions (Som *et al.*, 2014), respectively and β is the constant of interaction (Qian *et al.*, 2023). Fig. 5.15 denotes the plot of $\left(\frac{I_0}{I} - 1\right)$ vrs x on a log-log scale. The plot data is fitted with a linear equation with $slope \frac{n}{3} = 1.67$ so $n = 5.01$ which is close to 6 indicating that the possible transfer energy mechanism from Tb^{3+} to Eu^{3+} is dipole-dipole interaction (Tian *et al.*, 2013) which is consistent with previous findings made using Dexter's energy transfer formula, which is based on the Reisfeld approximation.

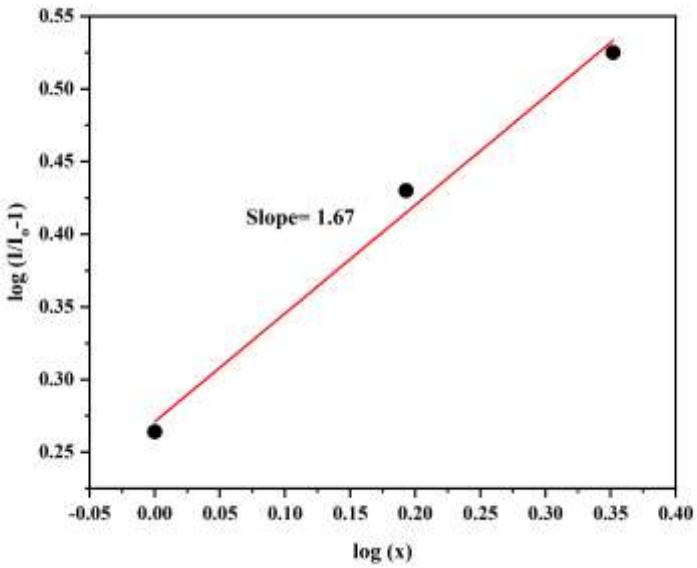

Fig. 5.15: Plot of log $\left(\frac{I_0}{I} - 1\right)$ vrs log(x) using Vai Uitert's model, the linear fits are shown by the red solid lines.

5.3.7 Color tunability

In order to determine the actual color tunability of the material, examining the color coordinates shown on a traditional chromaticity diagram is necessary. A tool used to measure the tunability of the emission wavelength and the intensity variation in the emission band (Kirdsiri *et al.*, 2019) is the 1931 (Commission International de'Eclairage) diagram. It is a universal method of representing every color by combining three primary colours. The CIE Chromaticity diagram of ZnS:Tb:Eu with varying concentrations of Tb^{3+} is shown in Fig. 5.16, which were derived from their corresponding PL spectra at 370 nm UV light excitation. The following equations are used to derive the chromaticity coordinates from the tri-stimulus values (Liping Wang *et al.*, 2010).

$$x = \frac{X}{X+Y+Z} \tag{5.11}$$

$$y = \frac{Y}{X+Y+Z} \tag{5.12}$$

$$z = \frac{Z}{X+Y+Z} = 1 - x - y \tag{5.13}$$

The color coordinates (x, y) values of the studied samples are represented in Table 5.5; the color tunability falls within the blueish to purplish region as the Tb^{3+} ion concentration increases.

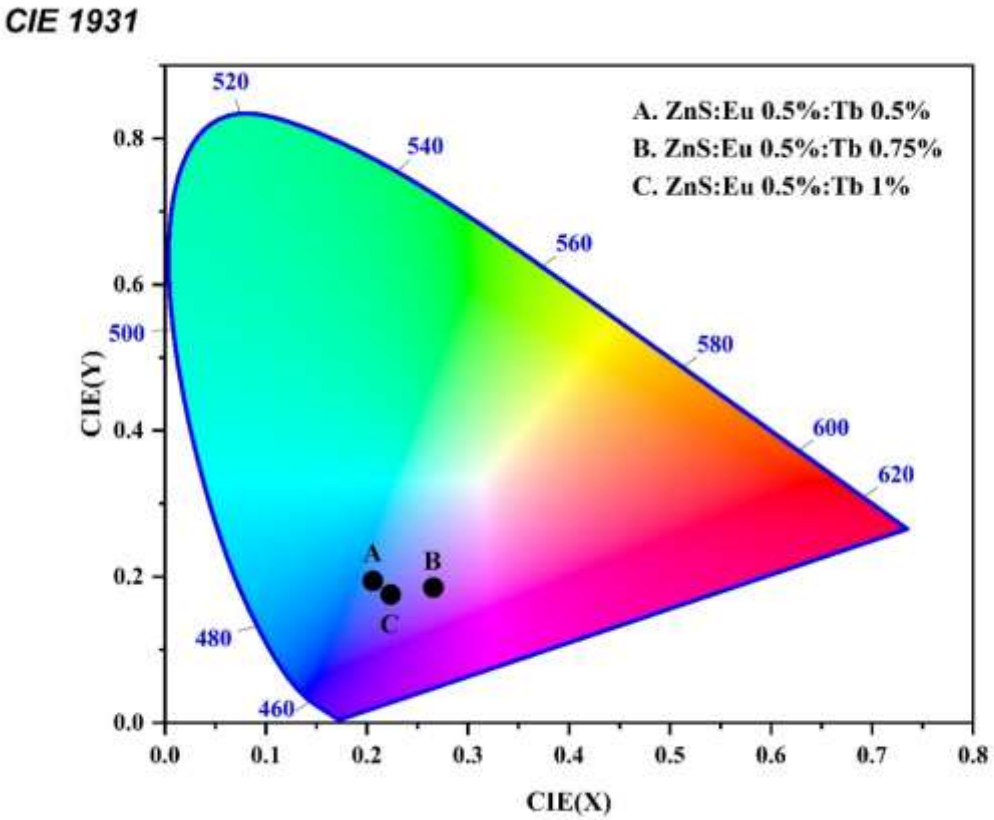

Fig. 5.16: CIE Chromaticity of ZnS:Tb:Eu doped silicate glass

Table 5.5: CIE chromaticity coordinates of ZnS:Tb:Eu doped silicate glass.

ZnS: Eu^{3+} 0.5%: *x* Tb %	**X**	**Y**
0.50 mol %	0.20591	0.19415
0.75 mol %	0.26564	0.18518
1.0 mol %	0.22343	0.17567

5.4 Conclusion

Tb^{3+} ion and Eu^{3+} ion single doped with a fixed concentration of ZnS NPs and co-doped with a fixed concentration of Eu^{3+} ion and changing concentration of Tb^{3+} ion have been successfully synthesized by a sol-gel method. The various physical properties were calculated. The FTIR spectra reveal the removal of the OH group with annealing, and the change in concentration does not have a significant impact on the IR spectra. The PL excitation and emission spectra showed that there is a transfer of energy from Tb^{3+} ions to Eu^{3+} ions. The transfer efficiency is calculated as 84.9%. Dipole-dipole interaction can be asserted as the dominant mechanism for the energy transfer from Tb^{3+} to Eu^{3+} ions, as anticipated by two distinct energy transfer formulas: (i) Dexter's energy transfer formula combined with Reisfeld's approximation; (ii) Van Uitert's. The PL also revealed that the emission colour tunability falls within the blueish to purplish region by varying Tb^{3+} ion concentration under excited with an UV light source with wavelength 370 nm.

REFERENCES

Kumaresh A, Kumar R Arun, Ravikumar N, Madhusoodanan U, Panigrahi B S, Marimuthu K and Anuradha M (2016). Structural and photoluminescence studies on europium-doped lithium tetraborate (Eu:$Li_2B_4O_7$) single crystal grown by microtube Czochralski (μT-Cz) technique. *Chin. Phys. B* **25(5)**: 058105. doi: 10.1088/1674-1056/25/5/058105.

Yu C.C., Liu X.M., Yu M., Lin C.K., Li C.X., Wang H., Lin J. (2007) Enhanced photoluminescence of Ba_2GdNbO_6: Eu^{3+}/Dy^{3+} phosphors by Li+ doping. *J. Solid State Chem.* **180(11)**:3058-3065. doi: https://doi.org/10.1016/j.jssc.2007.08.028

Carboxylatopillar [5] arene as stationary phase. *Electrophoresis* **39(2)**: 363-369. doi: https://doi.org/10.1002/elps.201700320

Kong Deying, Chen Zilin (2017) Open-tubular capillary electrochromatography using doi: https://doi.org/10.1039/D3CE01044A

Jeon H.S, Kim S.K, Park H.L, Kim G.C, Bang J.H, Lee M (2001) Observation of Two Independent Energy Transfer Mechanisms in $BaAl_{12}O_{19}$: Ce^{3+}0.06+Eu^{2+}x phosphor. *Solid State Commun.* **120 (5–6)**: 221-225. doi: https://doi.org/10.1016/S0038-1098(01)00323-4

Liu Junliang, Lu Liping, Liu Xiuling, Mi Xiaoyun (2023) Luminescence performance and energy transfer mechanism investigation of RE^{3+} (Eu^{3+}/Tb^{3+}/Ce^{3+})-doped Y_2O_3 phosphors. *Cryst. Eng. Comm.* **26**:160-169.

Shaweta Mohan, Simranpreet Kaur, Puneet Kaur, D.P. Singh (2018) Spectroscopic investigations of Sm^{3+}-doped lead alumino-borate glasses containing zinc, lithium and barium oxides. *J. Alloys Compd.* **763**: 486-495. doi: https://doi.org/10.1016/j.jallcom.2018.05.319

Singh Kasturi, R. Marikumar, Sivakumar Vaidyanathan (2018) Trivalent rare-earth activated hexagonal lanthanum fluoride (LaF_3:RE^{3+}, where RE = Tb, Sm, Dy and Tm) nanocrystals: Synthesis and optical properties. *Lumin.* **33(5)**: 897-906. doi: https://doi.org/10.1002/bio.3488

Qian Xinyu, Song Qingsong, Liu Jian, Chen Peng, Wang Wudi, Xue Yanyan, Guixin Cao, Xiaodong Xu, Xu Jun (2023) Ce, Tb, Gd: YAG-Al_2O_3 eutectic crystal phosphor plates for high-power warm white LED applications. *Opt. Maters.* **137**:113567. doi: https://doi.org/10.1016/j.optmat.2023.113567

Zhu Xuemei, Zhou Zhufa (2017) Photoluminescence and energy transfer mechanism of a novel tunable color phosphor Na_2MgSiO_4:Tb^{3+}, Eu^{3+}. *J. Lumin.* **188**: 589-594. doi: https://doi.org/10.1016/j.jlumin.2017.05.003

Tian Yue, Chen Baojiu, Tian Bining, Yu Naisen, Sun Jiashi, Li Xiangping, Jinsu Zhang, Lihong Cheng, Haiyang Zhong, Qingyu Meng, Ruinian Hua (2013) Hydrothermal synthesis and tunable luminescence of persimmon-like sodium lanthanum tungstate: Tb^{3+}, Eu^{3+} hierarchical microarchitectures. *J. Colloid Interface Sci.* **393**:44-52. doi: https://doi.org/10.1016/j.jcis.2012.10.031

Zelun Li, Xiaotong Zhao, Xuekun Hong, Hujiang Yang, Dongyu Fang, Yonggang Wang, Ming Lei (2022) Hierarchically porous boron nitride nanoribbon for

safe and high-performance bisphenol A adsorption. *Mater. Lett* **307**:131022. doi: https://doi.org/10.1016/j.matlet.2021.131022

Kirdsiri K., Rajaramakrishna R., Damdee B., Kim H.J., Nuntawong N., Horphathum Mati, Kaewkhao J. (2019) Influence of alkaline earth oxides on Eu3+ doped lithium borate glasses for photonic, laser and radiation detection material applications. *Solid State Sci.* **89**:57-66. doi: https://doi.org/10.1016/j.solidstatesciences.2018.12.019

Honglan Li, Guixia Liu, Jinxian Wang, Xiangting Dong, Wensheng Yu (2017) Eu3+/Tb3+ doped cubic BaGdF5 multifunctional nanophosphors: Multicolor tunable luminescence, energy transfer and magnetic properties. *J. Lumin.* **186**:6-15. doi: https://doi.org/10.1016/j.jlumin.2017.02.005

Suthanthirakumar P., Arunkumar S., Marimuthu K. (2018) Spectroscopic properties and excited state dynamics of Sm3+ ions in zinc telluro-fluoroborate glasses. *J. Lumin.* **202**: 289-300. doi: https://doi.org/10.1016/j.jlumin.2018.05.069

Dhaterwal Deepika, Matoria Mahesh, Singh Sonika (2024) Study of the synthesis techniques and photoluminescence properties of Eu^{3+}- Tb^{3+} co-doped phosphors: A review. *Next Nanotechnology* **5**: 100033. doi: https://doi.org/10.1016/j.nxnano.2023.100033

Liu Chunmeng, Hiu Dejian, Yan Jing, Zhou Lei, Kuang Xioujun, Liang Hongbin, Huang Yun, Zhang Bingbing, Tao Te (2014) Energy Transfer and Tunable Luminescence of NaLa $(PO_3)_4$: Tb^{3+}/Eu^{3+} under VUV and Low-Voltage Electron Beam Excitation. *J. Phys. Chem. C* **118(6)**: 3220–3229. doi: https://doi.org/10.1021/jp410131q

Som S., Mitra P., Kumar Vijay, Vinod Kumar, Terblans J. J., Swarta H. C., Sharma S. K. (2014) Energy transfer phenomena and colour tunability in $Y_2O_2S:Eu^{3+}/Dy^{3+}$ micro-fibers for white emission in solid state lighting application.
Dalton Trans. **43**: 9860-9871. doi: https://doi.org/10.1039/C4DT00349G

Dawngliana K.M.S., Fanai A.L., Rai S. (2023) Structural and optical studies of Sm^{3+}-doped silica glass along with TiO_2 nanoparticles for photonic applications. *J Non-Cryst. Solids* **607** :122226. doi: https://doi.org/10.1016/j.jnoncrysol.2023.122226

Zhu, D. Li, J.; Guo, X.; Li, Q.; Wu, H.; Meng, L.; Liu, Z (2019) Controlled Synthesis of Tb^{3+}/Eu^{3+} Co-Doped Gd_2O_3 Phosphors with Enhanced Red Emission. *Molecules* **24***:* 759. doi: https://doi.org/10.3390/molecules24040759

Shangrui Nan, Feng Hong, Haiping Xu, Jingzhi Dou, Guixia Liu, Xiangting Dong, Jinxian Wang, Wensheng Yu (2020) Luminescence properties and energy transfer of Tb^{3+}, Eu^{3+} co-doped $YTaO_4$ phosphors obtained via sol–gel combustion process. *J. Maters Sci.: Maters. in Elects.* **31**:13688–13695. doi: https://doi.org/10.1007/s10854-020-03926-2

Van Tuyen Ho and Son Nguyen Manh (2017) Luminescence properties and energy transfer of Tb^{3+}–Eu^{3+} co-doped $Sr_3B_2O_6$ phosphors. *Int. J. Modern Physics B* **31**:15. doi: http://dx.doi.org/10.1142/S0217979217501284

Bedyal A. K., Ramteke D. D., Kumar Vinay, Swart H. C. (2019) Excitation wavelength and Eu^{3+}/Tb^{3+} content ratio dependent tunable photoluminescence from $NaSrBO_3:Eu^{3+}/Tb^{3+}$ phosphor. *J. Mater. Sci:*

Maters. in Elects. **30**:11714–11726 doi: https://doi.org/10.1007/s10854-019-01533-4

Rawat Kusum, Vishwakarma Amit K., Jha Kaushal (2022) Multicolour emission and energy transfer dynamics in thermally stable $Ca_2Ga_2SiO_7:Tb^{3+}/Eu^{3+}$ for warm w-LEDs application. *Optics & Laser Tech.* **145**:107455. doi: https://doi.org/10.1016/j.optlastec.2021.107455

Zheng Xingxing, Yang Maolin, Wang Guanhua, Zhou Wenli, Zhang Jilin, Liping Yu, Ping Wang, Zhongxian Qiu, Chengzhi Li, Shixun Lian (2020) Luminescence tuning of Tb/Eu Co-doped zinc aluminoborosilicate glasses for white LED applications. *Ceramics Inter*. **46(17)**: 26608-26615. doi: https://doi.org/10.1016/j.ceramint.2020.07.129

Pisarska Joanna, Kos Agnieszka, Marta Sołtys, Lidia Żur, Wojciech A. Pisarski (2014) Energy transfer from Tb^{3+} to Eu^{3+} in lead borate glass. *J. Non-Cryst. Solids* **388**:1-5. doi: https://doi.org/10.1016/j.jnoncrysol.2014.01.019

Said Hajer, Oueslati Omrani Refka, Ruiz Arana Laura, Dhouha El Bahri, Slim Boussen, Chaker Bouzidi, Huayna Terraschke, Ahmed Hichem Hamzaoui, Adel M'nif (2019) The effect of silica additive on the structural and luminescence properties of Eu^{3+}/Tb^{3+} co-doped metaphosphate glasses. *J. Mole. Struc.* **1192**: 42-48. doi: https://doi.org/10.1016/j.molstruc.2019.04.087

Zhu Chaofeng, Chaussedent Stéphane, Shujiang Liu, Yanfei Zhang, André Monteil, Nathalie Gaumer, Yuanzheng Yue (2013) Composition dependence of luminescence of Eu and Eu/Tb doped silicate glasses for LED applications. *J. Alloys Compds* **555**: 232-236. doi: https://doi.org/10.1016/j.jallcom.2012.12.052

Caldino U., A´lvarez E., Speghini A., Bettinelli M. (2013) New greenish-yellow and yellowish-green emitting glass phosphors: Tb^{3+}/Eu^{3+} and $Ce^{3+}/Tb^{3+}/Eu^{3+}$ in zinc phosphate glasses. *J. Lumin.* **135**: 216-220. doi: http://dx.doi.org/10.1016/j.jlumin.2012.10.013

Luo Yuxia, Liu Zhenyu, Hon Tung Wong, Lei Zhou, Ka-Leung Wong, Kwok Keung Shiu and Peter A. Tanner (2019). Energy Transfer between Tb^{3+} and Eu^{3+} in $LaPO_4$: Pulsed versus Switched-off Continuous Wave Excitation. *Adv. Sci.* **6**:1900487. doi: 10.1002/advs.201900487

Yasi J., Fusong J., Fuxi G. (1982) Optical and other physical properties of Al $(PO_3)_3$-containing fluorophosphate glasses. *J. Phys.* **43**:315-318. doi: 10.1051/jphyscol:1982958

Haralampieva A., Lozanova I.S., Dimitrov V. (2012) Optical properties and structure of Bao-V_2O_5 and Fe_2O_3-Bao-V_2O_5 glasses. *J. Chem. Technol. Metallurgy* **47**:392-397.

Annapurna Devi Ch.B., Swapna K., Mahamuda S.K., Venkateswarla M., Prasad M.V.V.K.S., Siva Rama Krishna Reddy K., Nisha Deopa, Rao A.S. (2019) Spectroscopic studies and lasing potentialities of Sm^{3+} ions doped single alkali and mixed alkali fluoro tungsten tellurite glasses. *Op.t Laser. Technol.* **111**:176-183. doi: https://doi.org/10.1016/j.optlastec.2018.09.051

Dieke G.H. (1968) Spectroscopy & Energy Levels of Rare Earth Compounds, Inter Science, New York.

Carnall W.T., Fields P.R., Rajnak K. (1968) Spectral Intensities of the Trivalent Lanthanides and Actinides in Solution. II. Pm^{3+}, Sm^{3+}, Eu^{3+}, Gd^{3+}, $Tb^{3+,}$ Dy^{3+}, and Ho^{3+}. *J. Chem. Phys.* **49**:4412-4428. doi: https://doi.org/10.1063/1.1669892

Liping Wang, Xudong Xu, Xin Yuan (2010) Preparation and photoluminescent properties of doped nanoparticles of ZnS by solid-state reaction. *J. Lumin.* **130**: 137–140. doi: https://doi.org/10.1016/j.jlumin.2009.07.036

CHAPTER-6
ENERGY TRANSFER STUDY BETWEEN RHODAMINE B AND RHODAMINE 6G

In this chapter, we used the absorption and photoluminescence techniques for the study of the prepared samples. The interest of absorption and fluorescence spectroscopy is obvious in photonics. These techniques allow one to determine the energy transfer between Laser Dyes embedded in a glass matrix.

6.1 Introduction

Applications of dyes lasers are extensive and varied today. They are found in communication techniques, in microscopy, and in many spectroscopic applications such as Raman spectroscopy for following photochemical reactions and ultrafast reaction kinetics, in isotope separation (Shankarling *et al.*, 2010) and also in medical fields such as trace analysis, port wine-stains treatment, lithostripsy, angioplasty, and vascular lesions. Polymer films containing luminescent dyes are widely used in sensors, which maximize the effectiveness of the dye; thereby the dye dissolves in the solvent of the polymer.

6.2 Solid State Dye Lasers

Dye lasers, using organic colorants to bring out coherent emissions in the UV to IR spectral region when optically pumped by flashlamps or lasers, operate in the vapor, liquid and solid states. Vapor phase dye lasers, even though more efficient, required high temperatures. Liquid state dye lasers are primarily studied as they are conveniently prepared by dissolving the dyes in a suitable solvent. However, the liquid dyes are restricted in use outside the laboratory and cannot be used in certain applications because of the fact that they require large volumes of solvents.

On the other hand, a solid-state dye laser can be arranged by embedding the dye into an appropriate (organic) polymer or (inorganic) sol-gel host, or into a composite of both, to obtain a physically rigid structure (Schafer, 1990). The use of solid matrices containing laser dyes is an attractive alternative to a conventional liquid dye solution (Singh *et al*., 2003). The first solid-state dye laser was reported in

the late 1960s by Saffer and Mc Farland (1967) and Peterson and Snavely (1968). However, work on solid- state dye lasers was not pursued for over a decade due to low lasing efficiencies and fast photo-degradation of the dye (Singh *et al*., 2003). In recent years, a significant breakthrough has been achieved in the development of practical tunable solid-state dye lasers (Duarte *et al.*, 2004; Costela *et al.*, 2001).

Solid-state dye lasers offer various benefits in comparison to traditional liquid dye lasers. These lasers have the advantage of being easily handled and having low production costs and high operational safety. They can also be used for atmosphere and underwater sensing and local area communications networks. Other technical advantages, i.e., Stoke's shift and photostability are larger in the glass matrix compared to the liquid sample, and front-face fluorescence stability is also observed. Compactness, manageability, and versatility; lack of flammability and toxicity can also be added. Moreover, the flow function and solvent evaporation are considerably reduced in the case of solid–state dye lasers (Singh *et al*., 2003). Nevertheless, to increase the photo-stability which depends on the inter-molecular and intra-molecular interactions of the dye molecules with surrounding chemically active molecules (Singh *et al*., 2003), and to extend the range of output of the dyes due to long lived absorption that gradually builds up, reduces the gain, and ultimately terminates the lasing process, is still a challenge in developing solid-state dye lasers.

6.3 RhB and Rh6G doped in Silica Glass Matrix

In the last few years, many efforts have been performed to embed dye molecules in silica glasses (Esperance *et al.*, 1992; Suratwala *et al.*, 1998) with the aim to obtain solid state dye laser devices that could replace the liquid dye laser. Silica is prepared to its superior mechanical, thermal, and optical properties. Due to the inorganize Si-O-Si backbone, they present improved thermal and mechanical properties as compared to common organic polymers (Costela *et al.*, 2001). TEOS has better lasing stability as compared to others, evidencing the influence of the size of the lateral substituent group on the laser properties of the resulting material (Costel *et al.*, 2007). Rhodamine-B dye and Rhodamine-6G can be immobilized in silica hosts. RhB and Rh6G are among the Xanthene group dyes in which most of them show efficient laser action in the 560 to 800 nm region, but the Rhodamine

group covers the wavelength region from 500 to 700 nm and is generally very efficient (Shankarling *et al.*, 2010). Most of the commercial dyes come under this Xanthene class group. The Rh6G shows laser action in 590nm region and lases with about one percent efficiency in most flash lamp pumped dye lasers, that's why it is used as a reference dye to measure and exhibits good photo-stability. The most promising combinations of dye and host for efficiency and photostability were found (Costela *et al.*, 2001) in Rh6G sol-gel glass. The thermo optical and mechanical parameters are determined by a silica matrix whose thermo optical constants are better by two orders of magnitude than those of polymers (Singh *et al*., 2003). When Rh6G is used as a gain medium, both the lasing efficiency and the photo-stability first increase with the proportion of the organic component (Costela *et al.*, 2001). To optimize the photostability of the dye, a compromise must reach between the enhancement of thermal dissipation in the material and the increase in the photochemical destruction of the dye by carefully controlling the inorganic-organic matrix composition (Costela *et al.*, 2001). The presence of the inorganic component in the hybrid matrices increases the rigidity and fragility of the resulting materials (Costela *et al*., 2001) and photo-stabilities increased with the solid content. Incorporating dyes into the ionic Rhodamine performed best in the inorganic-organic sol-gel glass host. Alternatively, the nanoparticle can be incorporated into a solid host to enhance the dye's optical characteristics. The luminescence intensity and quantum yield of organic molecules and chromophore dyes when doped in porous solid matrices are increased by several orders compared to their values in liquid solvent (Bora *et al.*, 2014). Therefore, laser dyes doped in solid matrices are extensively used in the development of solid-state dye lasers (Bora *et al.*, 2014). But, to our knowledge, very few works are reported on the co-doped effect on luminescence properties of dye doped solid matrices (Bora *et al.*, 2014).

6.4. Molecular Structure

The molecular formulas of RhB and Rh6G is $C_{24}H_{31}ClN_2O_3$ and $C_{28}H_{31}ClN_2O_3$ respectively. RhB consists of green crystal or reddish-violet powder, whereas Rh6G consists of bronze or red powder. Their molecular weight is 479.02 g/mol. The molecular structure of RhB and Rh6G is shown below.

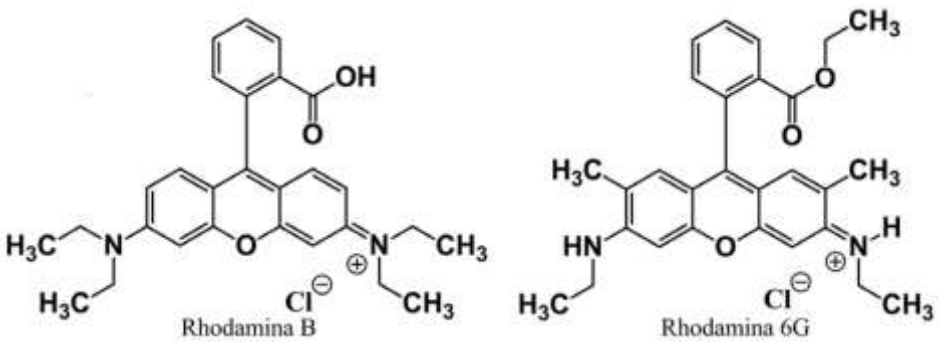

(a) (b)

Fig 6.1: Structural formula of (a) Rhodamine B (b) Rhodamine 6G

6.5 Intermolecular Energy Transfer

The precise theory of dye laser energy transfer is considered thoroughly elsewhere. The energy transfer efficiency (E) can be calculated as

$$E = 1 - \frac{I}{I_0} \tag{6.1}$$

Where, I_0 is the fluorescence intensity of the donor in the absence of the donor and I is the fluorescence intensity in the presence of the acceptor (Ghosh *et al.*, 2009).

According to Forster Dexter Theory, the rate of transfer for a donor and acceptor separated by a distance r is given by

$$k_T(\mathrm{r}) = \frac{Q_D k^2}{\tau_D r^6}\left(\frac{9000(ln10)}{128\pi^5 N n^4}\right)\int_0^\infty F_D(\lambda)\varepsilon_A(\lambda)\lambda^4 d\lambda \tag{6.2}$$

where Q_D is the quantum yield of the donor in the absence of the acceptor (Brouwer, 2011), N is Avogadro's number, n is the refractive index of the medium between the donor and acceptor, τ_D is the lifetime of the donor in the absence of the acceptor; $F_D(\lambda)$ is the corrected fluorescence intensity of the donor in the wavelength range λ to $\lambda + \Delta\lambda$, with the total intensity normalized to unity; $\varepsilon_A(\lambda)$ is the extinction coefficient of the acceptor at λ, which is typically in units of M^{-1} cm^{-1}; $k^2$is the well-known orientation factor of two dipoles interacting and is usually assumed to be equal to 2/3, which is appropriate for dynamic random averaging of the donor and acceptor (Seth *et al.*, 2005).

The overlap integral J(λ) expresses the degree of spectral overlap between the donor fluorescence and the acceptor absorption.

$$J(\lambda) = \frac{\int_0^\infty F_D(\lambda)\varepsilon_A(\lambda)\lambda^4 d\lambda}{\int_0^\infty F_D(\lambda) d\lambda} \quad (6.3)$$

Where $F_D(\lambda)$ is dimensionless. If $\varepsilon_A(\lambda)$ is expressed in units of M^{-1} cm^{-1} and λ is in nanometers, then $J(\lambda)$ is in units of M^{-1} cm^{-1} nm^{-4} (Seth *et al.*, 2005). Eq. (3) can be expressed as

$$k_T(r) = \frac{1}{\tau_D}\left(\frac{R_0}{r}\right)^6 \quad (6.4)$$

Where R_0 is defined as

$$R_0^6 = \left(\frac{9000(ln10)k^2Q_D}{128\pi^5 N n^4}\right)\int_0^\infty F_D(\lambda)\varepsilon_A(\lambda)\lambda^4 d\lambda \quad (6.5)$$

The above equation can be reduced to

$$R_0 = 9.78 \times 10^3[k^2 n^{-4} Q_D J(\lambda)]^{1/6} \text{ (in Å)} \quad (6.6)$$

Where R_0 is known as Förster distance, which is the distance at which the donor decay rate is equal to the transfer rate $k_T(r)$ in the absence of the acceptor (τ_D^{-1}). That is the separation distance that yields 50% energy transfer efficiency (Seth *et al.*, 2005).

The efficiency of energy transfer (E) is the fraction of photons absorbed by the donor that is transferred to the acceptor (Seth *et al.*, 2005). This fraction is given by,

$$E = \frac{k_T}{\tau_D^{-1} + k_T} \quad (6.7)$$

This represents the proportion of the transfer rate to the donor's overall decay rate. Recalling that

$k_{ET} = \tau_D^{-1}\left(\frac{R_0}{r}\right)^6$, we can rearrange Eq. (6.7) to yield (Lakowicz, 2006; Seth *et al.*, 2005)

$$E = \frac{R_0^6}{R_0^6 + r^6} \quad (6.8)$$

The main mechanisms proposed for energy transfer are:

(1) Radiative energy transfer, i.e., the absorption of donor emission by an acceptor molecule. The mechanism can be illustrated as

Donor emission: $D^* \longrightarrow D + h\upsilon_A$

Acceptor absorption: $A + h\upsilon_A \longrightarrow A^*$

Where the asterisk represents an electronically excited state. The fluorescence lifetime of both donor and acceptor dye molecules is kept unchanged in the radiative energy transfer process.

(2) Diffusion-controlled collision and energy transfer; this process is a non- radiative process and is viscosity (Yang *et al.*, 2005) independent.

(3) Resonance energy transfer due to an excited donor molecule with the excitation energy to the acceptor molecule of the ground state due to long-range dipole-dipole interaction (Mahato *et al.*, 2023). This is a non-radiative energy transfer process. FRET is a process where the excitation energy of a donor is non-radiatively transferred to a nearby acceptor (Chowdhury *et al.*, 2005). Its efficiency depends on the inverse sixth power of the distance of separation between the donor and acceptor molecules.

The idea of energy transfer, in which molecules that are electronically excited transfer their energy to nearby molecules, is widely employed as an effective tool for measuring distances on the nanoscale and examining molecular interactions. The process of energy transfer wherein an excited donor and an acceptor molecule interact dipole-to-dipole. Potential uses for this energy transfer include luminescence tagging, imaging, bio-sensors, analytical biochemistry, medical diagnostics, and environmental analysis. It is also of great interest to the bio-sensor community. The energy transfer between donor and acceptor pairs is also found to be very effective in controlling and tuning light emission in laser gain media (Kodeary, 2015). Therefore, many exertions are being made by the researchers to improve laser efficiency and to extend their spectral region of operation (Kodeary, 2015).

On basis of the report made by Kodeary (Kodeary, 2015)," The transfer of energy from the donor Rh6G dye to the acceptor RhB dye in liquid state was highest in mixing the concentrations ($1x10^{-5}$ Rh6G and $1x10^{-6}$ RhB)". In light of this report, the energy transfer between their mixtures (Rh6G and RhB dyes) in silica hosts prepared by the sol-gel method, doped with a concentration range of 10^{-6} to 10^{-3}, was studied in this chapter. Information regarding the interaction between Rh6G and RhB dyes is provided by the investigations.

6.6 Experimental

The prepared sample's fluorescence and absorption spectra were captured using an iHR320 imaging spectrometer (HORIBA). Room temperature was used to record all optical measurements. Diode laser excitation wavelengths were set at 370 nm.

6.7 Rh6G doped and pure absorption spectra at varying concentrations in silica glass

Rh6G-doped and pure absorption spectra at varying concentrations in silica glass are shown in the Figs. 6.2 and 6.3. The typical absorption band of Rh6G is observed at (a) 531.5 nm, (b) 533 nm, and (c) 532 nm as shown in Fig. 6.2. When Rh6G concentration in ethanol solution increases, so does absorbance also. Table 6.1 shows that the FWHM rises as Rh6G concentration rises; in turn, Fig. 6.2 experienced a red shift. The absorption spectra of Rh6G doped with silica at three different concentrations were once again observed at (a) 525.48 nm, (b) 501.57 nm, and (c) 525.48 nm, as shown in Fig. 6.3. Furthermore, as Table 6.1 illustrates, the absorption intensity rises with Rh6G concentration while FWHM falls with increasing concentrations.

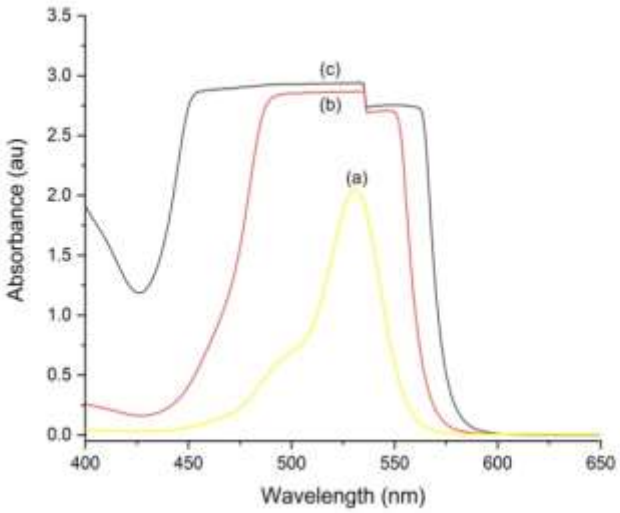

Fig. 6.2: Rh6G pure absorption spectra at varying concentrations (a)1×10^{-5}mol.L^{-1} Rh6G (b)1×10^{-4}mol.L^{-1} Rh6G (c)1×10^{-3}mol.L^{-1} in ethanol solvent.

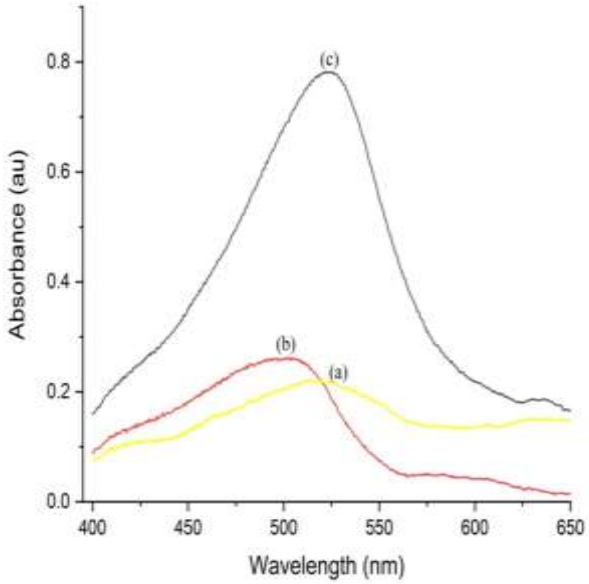

Fig. 6.3: Rh6G doped absorption spectra at varying concentrations (a) 1×10^{-5}mol.L^{-1} Rh6G (b)1×10^{-4}mol.L^{-1} Rh6G (c) 1×10^{-3}mol.L^{-1} in silica glass.

Table 6.1: Absorption of Rh6G in liquid and silica glass

Concentrations(M/L)	$1x10^{-5}$		$1x10^{-4}$		$1x10^{-3}$	
Rh6G in liquid and glass	liquid	silica glass	liquid	silica glass	liquid	silica glass
Wavelength (nm)	531.5	525.48	533	501.57	532	525.48
Absorbance (a.u)	2.048	0.218	2.868	0.263	2.944	0.782
FWHM (nm)	32.5	150.37	120	118.72	132.5	106.78

6.8 Rh6G doped and pure emission spectra at varying concentrations in silica glass

Figs. 6.4 and 6.5 display the emission spectra of pure Rh6G and Rh6G doped at various concentrations in silica glass. Fig. 6.4 displays the emission peak at (a) 558 nm with an intensity of 1252 (a.u.), (b) 579 nm with an intensity of 2737 (a.u.) and (c) 566.8 nm with an intensity of 4664 (a.u.). Therefore, the intensity of Rh6G's emission spectra increases from 1×10^{-3}mol.L^{-1} to 1×10^{-4}mol.L^{-1}, reaches its

maximum at 1×10^{-4}mol.L^{-1} and then decreases once more when the concentration is increased to 1×10^{-5}mol.L^{-1}. From Table 6.2, the FWHM increases with increasing concentrations in solid and liquid samples. The emission peak exhibited at (a) 536.94 nm with intensity 14788 (a.u.), (b) 555.53 nm with intensity 43493 (a.u.), and (c) 604.35 nm with intensity 43550 (a.u.) was observed from Fig. 6.5. In this case, concentration intensity reaches its maximum at 1×10^{-3}mol.L^{-1} and its minimum at 1×10^{-5}mol.L^{-1}.

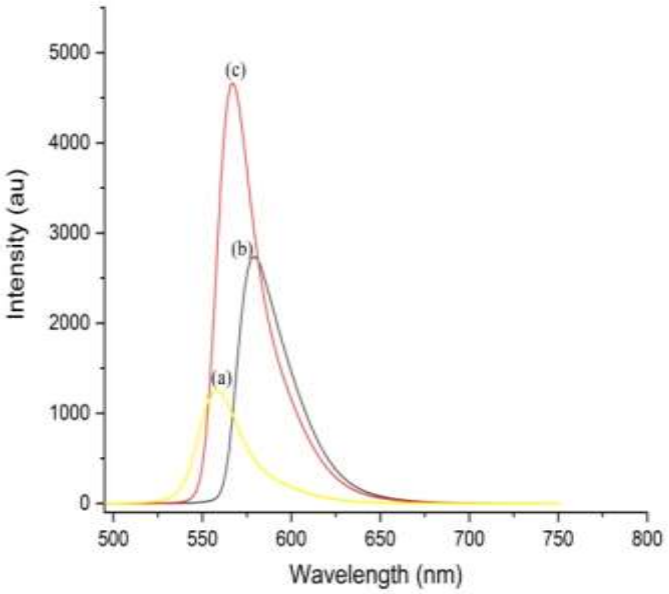

Fig. 6.4: Emission spectra of pure Rh6G at various concentrations (a)1×10^{-5} mol. L^{-1} Rh6G (b) 1×10^{-3} mol. L^{-1} Rh6G and (c)1×10^{-4} mol. L^{-1} Rh6G in ethanol solvent.

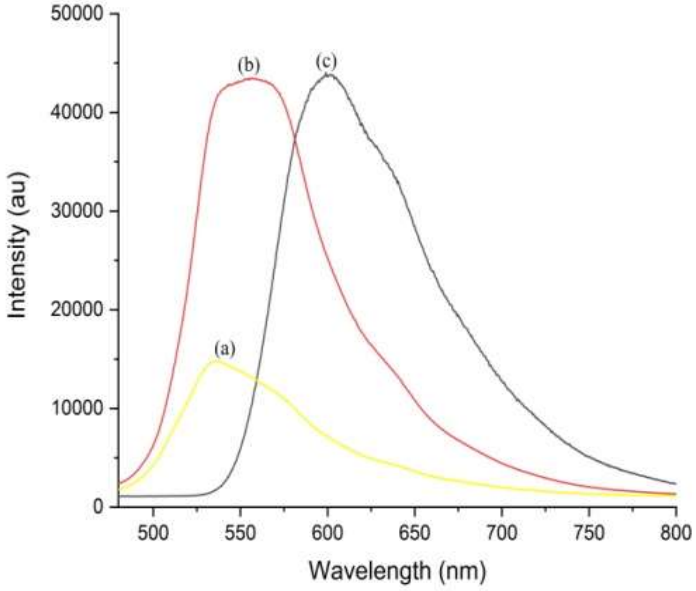

Fig. 6.5: Emission spectra of Rh6G doped at various concentrations (a)$1x10^{-5}$ mol. L^{-1} Rh6G (b)$1x10^{-4}$ mol. L^{-1} Rh6G and (c) $1x10^{-3}$ mol. L^{-1} mol. L^{-1} in silica glass.

Table 6.2: Emission of Rh6G in liquid and silica glass

Concentrations(M/L)	$1x10^{-5}$		$1x10^{-4}$		$1x10^{-3}$	
Rh6G in liquid and glass	liquid	silica glass	liquid	silica glass	liquid	silica glass
Wavelength (nm)	558	536.94	566.8	555.53	579	604.35
Intensity (a.u)	1252	14788	4664	43493	2737	43550
FWHM (nm)	28.8	88.13	27	88.65	32.8	99.16

6.9 Emission spectra of a mixture with a constant Rh6G dye concentration and varying RhB dye concentrations in a silica matrix.

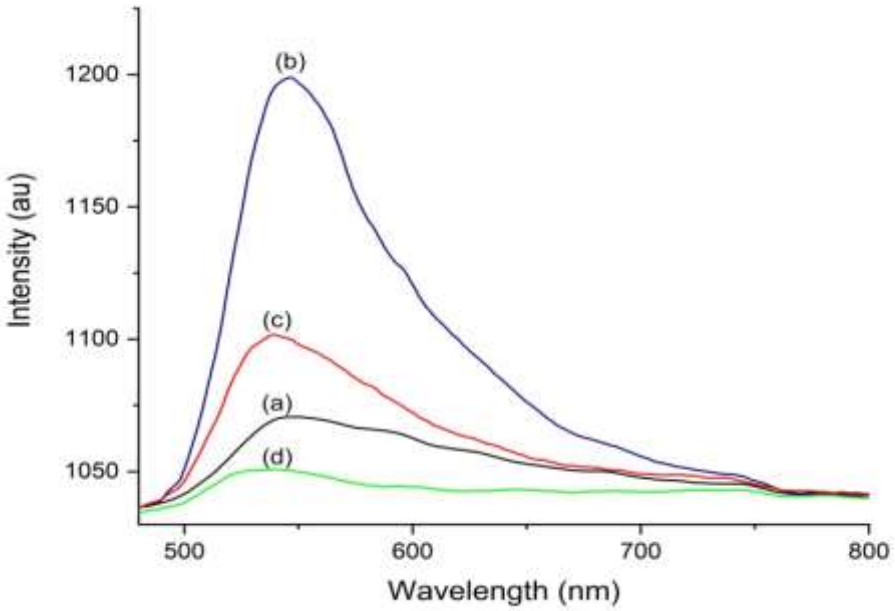

Fig. 6.6: Emission spectra of a mixture of 2% of $1x10^{-5}$ Rh6G with (a)1% of $1x10^{-6}$RhB (b) 1.5% of $1x10^{-6}$ RhB (c) 2% of $1x10^{-6}$ RhB (d)2.5% of $1x10^{-6}$ RhB with silica

Fig. 6.6 shows the room temperature emission spectra of Rh6G/RhB doped sol-gel silica glass under 450nm excitation. Four emission bands were observed at (a) 541.39 nm with intensity 1072 a.u. (b) 544.58 nm with intensity 1205 a.u. (c) 532.37 nm with intensity 1109 a.u. (d) 535.55 nm with intensity 1054 a.u. The emission intensity increases with increasing the concentration; therefore a red shift occurrs, attains maximum value, and decreases with further increasing the concentration due to the quenching effect. It is observed that there is a significant increase in the PL intensities of RhB due to the addition of Rh6G. These reveal that there is an efficient energy transfer from Rh6G to RhB in the studied host. It can also be seen that the emission spectrum of the acceptor increases when increasing the concentration of acceptor dye from 1% of $1x10^{-6}$ to 1.5% of $1x10^{-6}$ RhB. It attains the maximum intensity at 1.5% of $1x10^{-6}$ of RhB, suggesting energy transfer and intensity start

decreasing when increasing the concentrations. From Table 6.3, the FWHM increases as the Rh6G concentration grows from 1 to 1.5%, suggesting that the tunability increases with energy transfer. Increases in the intensity of acceptor spectra provide the larger number of photons with a wavelength within the absorption acceptor molecule; the convergence of molecules from each other when increasing the concentration is that these lead to interact more efficiently (Kodeary, 2015). We see a very wide spectrum extends from 500 nm to 700 nm, which is a very broad spectrum ideal for manufacturing lasers for midwife toning ranges of wavelength (Kodeary, 2015).

Table 6.3: Emission of Acceptor RhB with a fixed concentration of donor Rh6G

Acceptor concentration	$1x10^{-6}$	$1.5x10^{-6}$	$2x10^{-6}$	$2.5x10^{-6}$
Wavelength(nm)	541.39	544.58	532.37	535.55
Intensity (a.u.)	1072	1205	1109	1054
FWHM	86.53	132.65	113.59	83.35

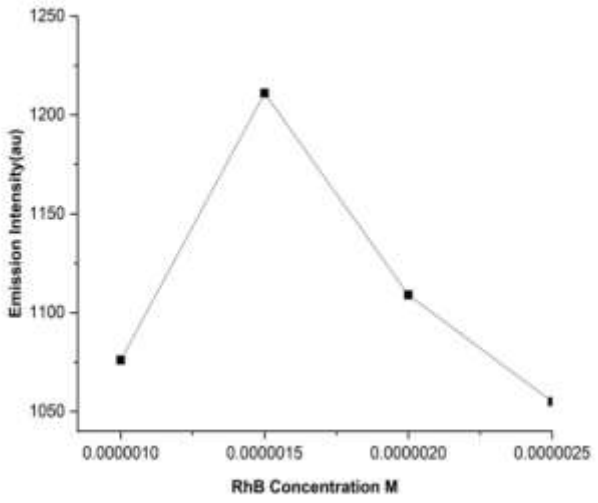

Fig. 6.7: Change the intensity of emission spectra of a mixture to fixed concentration of Rh6G dye and changing concentration of RhB dye.

6.10 Emission spectra of a mixture to fixed concentration of RhB dye and changing concentrations of Rh6G dye in silica matrix

Fig. 6.8 shows the mechanism of transfer of energy from the RhB dye to the Rh6G dye by mixing a fixed concentration of RhB dye and changing concentrations of Rh6G dye, as it shows that the emission spectra are excited wavelength 450 nm (Kodeary, 2015). As seen from the figure, the intensity of the emission spectra of the RhB dye increases by greater the amount of donor molecule, which means increases the number of photons within the wavelength range of the acceptor molecule (Kodeary, 2015). The merging of molecules from each other when increasing concentrations leads, to they interact more and more coherently (Kodeary, 2015).

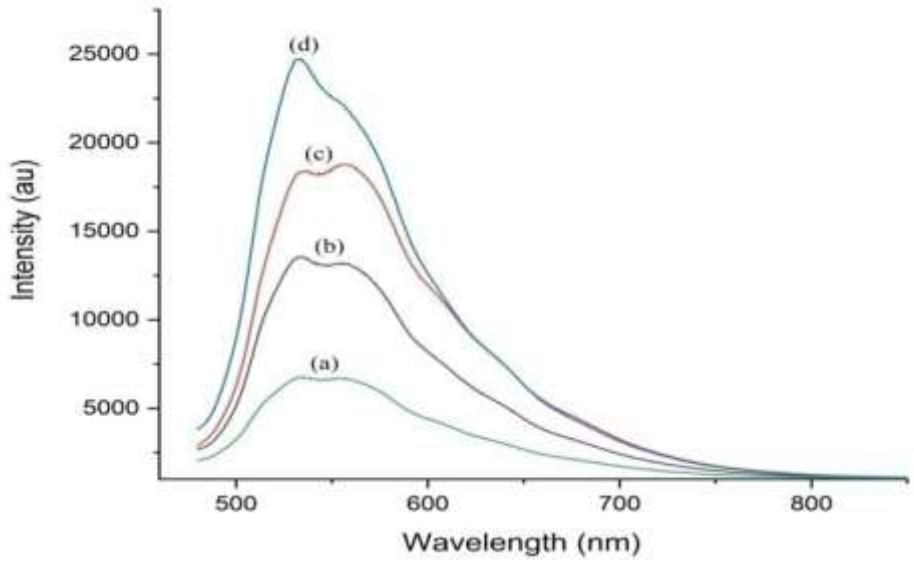

Fig. 6.8: Emission spectra of a mixture of 2% of $1x10^{-5}$ RhB with (a) 1% of $1x10^{-6}$ Rh6G (b)1.5% of $1x10^{-6}$Rh6G (c)2% of $1x10^{-6}$ Rh6G (d) 2.5% of $1x10^{-6}$ Rh6G with silica.

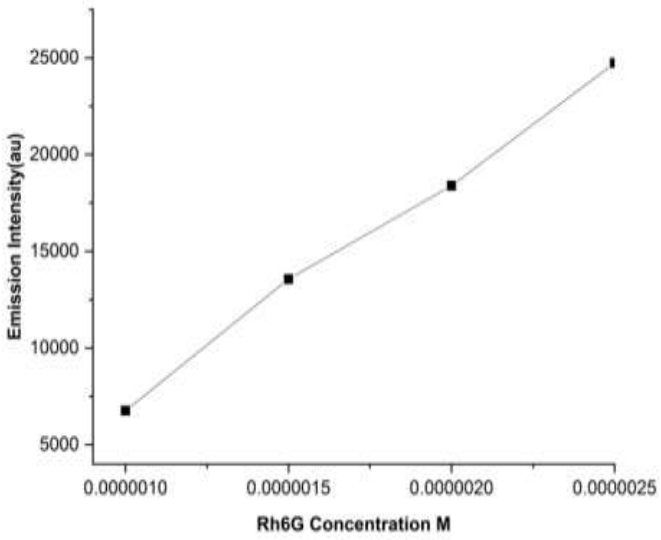

Fig.6.9: Change the intensity of emission spectra of a mixture to fixed concentration of RhB dye and changing concentration of Rh6G dye.

6.11 Conclusion

We concluded from this study that the absorption spectra for Rh6G increase with increasing concentrations for both the solid and liquid phases. Whereas emission spectra first increase with increasing the concentration, attain maximum value, and then decrease with further increasing the concentration for both the solid and liquid phases. Likewise, energy transfer between the donor RhG dye and acceptor RhB dye escalates with improving the donor concentration due to the merging of molecules. Moreover, while RhG dye and RhB dye interchange as acceptor and donor, energy transfer first increases with concentration of RhB, attains maximum value at 1.5%, then gradually decreases with further increasing the concentrations.

REFERENCES

Singh S, Kanetkar V R, Sridhar G, Muthuswamy V, Raja K (2003) Solid state polymeric dye lasers. *J. Lumin.* **101(4)**: 285–291. doi: https://doi.org/10.1016/S0022-2313(02)00571-9

Soffer B H, Mcfarland B B (1967) Continuously Tunable, Narrow-Band Organic Dye Lasers. *Appl. Phys. Lett.* **10(10)**: 266-267. doi: http://dx.doi.org/10.1063/1.1754804

Suratwala T, Gardlund Z, Davidson K, Uhlmann D R (1998) Silylated coumarin Dyes in sol-gel Hosts 2 Photostability and sol-Gel processing. *Chem. Mater.* **10(1)**: 199-209. doi: https://doi.org/10.1021/cm970340s

Al-Shamiri H A S, Abou Kana M T H (2010) Laser performance and photostability of RhB in solid host matrices. *Appl. Phys. B* **101(1)**:129-135. doi: http://dx.doi.org/10.1007/s00340-010-4192-6

Al-Shamiri H A S, Badr Y A, Abou Kana M T H (2011) Optical, Photophysical properties and photostability of laser dyes impregnated in Sol-Gel matrix. Saudi International Electronics, Communications, and Photonics Conference (SIECPC) Doi:10.1109/Siecpc 2011 5876987

Anand U, Jash C, Boddepalli R K, Shrivastava A, Mukherjee S (2011) Exploring the Mechanism of Fluorescence Quenching in Proteins Induced by Tetracycline. *J. Phys. Chem. B* **115(19)**: 6312–6320. doi: http://dx.doi.org/10.1021/jp2008978

Clapp A R, Medintz I L, Mattoussi H (2006) Forster Resonance Energy Transfer Investigations Using Quantum-Dot Fluorophores. *Chem. Phys. Chem.* **7(1)**: 47–57. doi: https://doi.org/10.1002/cphc.200690000

Costela A, Garcia –Moreno L, Sastre R, Materials for Solid state dye lasers, in Handbook of Advanced Electronic and Photonic materials and Devices, edited by Nalwa H S, Academic San Diego, CA, 2001, Vol 7, Chap 4.

Dayal S, Burda C (2007) Surface effects on quantum dot-based energy transfer. *J. Am. Chem. Soc.* **129(25)**:7977–7981. doi: https://doi.org/10.1021/ja071457c

Demes J N, Crosby G A (1971) Measurement of photoluminescence quantum yields Review. *J. Phys. Chem.* **75(8)**: 991-1024. doi: https://doi.org/10.1021/j100678a001

Szabelski M, Luchowski R, Gryczynski Z, Kapusta P, Ortmann U, Gryczynski I (2009) Evaluation of instrument response functions for lifetime imaging detectors using quenched Rose Bengal solutions. *Chem. Phys. Lett.* **471(1-3)**: 153–159. doi: http://dx.doi.org/10.1016/j.cplett.2009.02.001

Yariv E, Schultheiss S, Saraidarov T, Reisfeld R (2001) Efficiency and Photostability of dye-doped solid-state laser in different hosts. *Opt. Mater.* **16(1-2)**: 29-38. doi: http://dx.doi.org/10.1016/S0925-3467(00)00056-2

Zhou D, J D Piper J D, Abell C, Klenerman D, Kang D J, Ying L (2005) Fluorescence resonance energy transfer between a quantum dot donor and a dye acceptor attached to DNA. *Chem. Commun.* **38**: 4807–4809. doi: https://doi.org/10.1039/B508911E

Kodeary Ahmed Kadem (2015) Energy transfer studies in binary laser dye Mixtures between Rhodamine 6G and Rhodamine B. *Int. J of Scientific & Engineering Research* **6(9)**: 870-875.

Suratwala T, Gardlund Z, Davidson K, Uhlmann D R (1998) Silylated coumarin Dyes in sol-gel Hosts 2 Photostability and sol-Gel processing. *Chem. Mater.* **10(1)**: 199-209. doi: https://doi.org/10.1021/cm970340s

Duarte F J, Costela A, Dye lasers, in Encyclopedia of Modern Optics, edited by Guenther R D, steel D G, Bayvel L, Elsevier, New York, 2004, pp 400-4

Espérance D L, Chronister E L (1992) Optical energy transfer in Quinizarin doped sol gel glasses. *J. Opt. Soc. Am. A* **9(11)**: 2041-2046. doi: https://doi.org/10.1364/JOSAB.9.002041

Govindaraju S, Ankireddy S R, Viswanath B, Kim J, Yun K (2017). Fluorescent Gold Nanoclusters for Selective Detection of Dopamine in Cerebrospinal fluid. *Sci. Rep. 7 (1-7)*: 40298. doi: http://dx.doi.org/10.1038/srep40298

Kristoffersen A.S., Erga S.R., Hamre B., Frette Ø. (2014). Testing Fluorescence Lifetime Standards using Two-Photon Excitation and Time-Domain Instrumentation: Rhodamine B, Coumarin 6, and Lucifer Yellow. *J. Fluoresc.* **24**: 1015-1024. doi: https://doi.org/10.1007/s10895-014-1368-1

Kuriakose A C, Nampoori V P N, Thomas S (2020) Enhancement of optical properties in Neutral Red Dye through energy transfer from CdS Quantum Dots. *Chem. Phys. Lett.* **738(42)**:136851. doi: http://dx.doi.org/10.1016/j.cplett.2019.136851

Lakowicz J R, Principles of fluorescence spectroscopy 3rd editions (Springer Science + Business Media, New York, 2006).

Seth D, Chakrabarty D, Chakraborty A, Sarkar N (2005) Study of energy transfer from 7 amino coumarin donors to rhodamine 6G acceptor in non-aqueous reverse micelles. *Chem. Phys. Lett.* **401(4-6)**: 546–552. doi: http://dx.doi.org/10.1016/j.cplett.2004.11.119

Namboodiri C K R, Bisht P B, Dantham V R (2021) Cascaded Förster Resonance Energy Transfer and Role of Relay Dyes. *J. at mol. Condens. Nano. Phys.* **8**: 1–14. doi: http://dx.doi.org/10.26713/jamcnp.v8i1.1491

Ozsan M E, Johnson D R, Sadeghi M, Sivapathasundaram D (1996) Optical and electrical characterization of CdS thin films. *J. Mater. Sci.: Mater. Electron* **7**:119-125. doi: https://doi.org/10.1007/BF00225634

Peng H, Zhang L, Kjallman T H M, Soeller C, Sejdic J T (2007) DNA Hybridization Detection with Blue Luminescent Quantum Dots and Dye-Labeled Single-Stranded DNA. *J. Am. Chem. Soc.* **129**: 3048–3049.

Peterson O G, Snavely B B (1968) Stimulated emission from flash lamp excited organic dyes in polymethyl methacrylate. *App. Phys. Lett.* **12(7)**: 238-240. doi: https://doi.org/10.1063/1.1651972

Ray P C, Fortner A, Darbha G K (2006) Gold Nanoparticle-Based FRET Assay for the Detection of DNA Cleavage. *J. Phys. Chem. B* **110(42)**: 20745-20748-8. doi: http://dx.doi.org/10.1021/jp065121l

Reis H C O, Cossolin A S, Santos B A P, Castro K C, Pereira G M, Silva V C, Sousa Jr P T, Dall'Oglio E L, Vasconcelos L G, Morais E B (2018) Malt Bagasse Waste as Biosorbent for Malachite Green: An Ecofriendly Approach for Dye Removal from Aqueous Solution. *Int. J. Biotechnol. Bioeng.* **12(4)**: 118-126. doi: http://dx.doi.org/10.5281/zenodo.1340591

Shivkumar M A, Inamdar L S, Rabinal M H K, Mulimani B G, Advi Rao G M, Inamdar S R (2013) FRET from CdSe/ZnS Core-Shell Quantum Dots to Fluorescein 27 Dye. *Open J. Phy. Chem.* **03(01)**: 40-48. doi: http://dx.doi.org/10.4236/ojpc.2013.31006

Campbell Katie, Zappas Andrew, Uwe Bunz, Yonathan S. Thio, David G. Bucknall (2012) Fluorescence quenching of a poly (para-phenylene ethynylenes) by C60 fullerenes. *J. Photochem. and Photobiol. A* **249**: 41-46. doi: https://doi.org/10.1016/j.jphotochem.2012.08.015

Shankarling G.S., Jarag, K.J. (2010) Laser dyes. *Reson* **15**:804–818. doi: https://doi.org/10.1007/s12045-010-0090-9

Yang Yu, Qian Guodong, Su Deliang, Wang Zhiyu, Wang Minquan (2015) Energy transfer mechanism between laser dyes doped in ORMOSILs. *Chem. Phys. Lett.* **402(4-6)**: 389–394. doi: http://dx.doi.org/10.1016/j.cplett.2004.12.071

Costel A, I. García-Moreno, D. del Agua, O. García, R. Sastre (2007) Solid state dye lasers: new materials based on silicon. *Opt. Journal* **1**:1-6. doi: http://hdl.handle.net/10261/212150

Ghosh Debanjana, Debosreeta Bose, Deboleena Sarkar, Nitin Chattopadhyay (2009) Excited-State-Proton-Transfer-Triggered Fluorescence Resonance Energy Transfer: from 2-Naphthylamine to Phenosafranin. The *J. Phys. Chem. A* **113 (39)**:10460-10465. DOI: 10.1021/jp9054318

Chowdhury Paramita Saha, Sen Pratik, Patra Amitava (2005) Optical properties of CdS nanoparticles and the energy transfer from CdS nanoparticles to Rhodamine 6G. *Chem. Phys. Lett.* **413(4–6)**:311-314. doi: https://doi.org/10.1016/j.cplett.2005.07.088

Mahato Kapil Dev, Kumar Uday (2023) A comparative study of conventional FRET and light harvesting properties of Rh-110/Rh-6G and Rh-19/Rh-B organic dye pairs impregnated in sol-gel glasses. *Methods Appl. Fluoresc.* **11** 035003. doi: 10.1088/2050-6120/accfe4

Bora Dulen, Hazarika Subrata (2014) Optical Properties of Malachite Green Dye Doped SiO_2 Glasses: Effect of Transition Metal (Fe-I) Used as a Codopant. *Int. J. of Optics* vol. 2014, Article ID 865814, 9 pages, 2014. doi: https://doi.org/10.1155/2014/865814

SUMMARY AND FUTURE PROSPECTS

This chapter summarizes the general conclusions, findings, and future prospects of our research work. Our work mainly consists of sol-gel synthesis of RE (Tb^{3+}, Eu^{3+}, Sm^{3+}, Pr^{3+} ions) doped silica glass and the study of the annealing, co-doping with ZnS nanoparticles on the physical, structural, and spectroscopic properties of the doped glass to improve their suitability for optical applications. The high energy γ- irradiation effects on the optical properties of Sm^{3+} ions doped silica glass and the study of energy transfer between Tb^{3+}, Eu^{3+}co-doped ZnS in silica glass is also presented. In addition to RE doped glass, the synthesis and spectral characteristics of laser dyes RhB and Rh6G and their mixture in a solid matrix were also studied in detail.

Annealing produced optically clear and densified samples without the need for drying control chemical additives; however, in certain situations, an excessive rate of drying and annealing resulted in cracking and opacity. The FTIR spectrum of the sample displays a significant reduction in the hydroxyl absorption peak, indicating the effective removal of any remaining hydroxyls with annealing. Removal of the hydroxyl group also decreases the weight of the sample, thereby causing densification of the sample and closing the pores present, which preserve them from atmospheric moisture reabsorption.

Analysis of physical properties shows that the refractive index, density, and thickness of sample increase with increasing the concentration. A linear relationship between field strength and highest emission intensity peak was observed for all samples, while the polaron radius was inversely proportional to it.

XRD studies suggest the amorphous nature of silica hosts while the crystallinity of ZnS host enhances with an increase in annealing temperature by giving blende and hexagonal phases. TEM analysis confirmed that the studied ZnS host has a set of ring structures, which reveals that it has a polycrystalline structure in nature. The band gap energy of the doped samples decreases with the reduction of particle size. This phenomenon is termed the heavy doping effect. This size dependent variation in the band gap energy is due to the quantum confinement effect.

The CIE chromaticity color coordinates from emission spectra is used to calculate color tunability of studied samples. The color tunability always changes with change in RE concentrations as well as change in host concentration. Tb^{3+}, Eu^{3+}, Sm^{3+}, Pr^{3+} doped glass produced green light, white light, white hue light and green light, respectively and Tb^{3+} and Eu^{3+} co-doped falls within blueish to purplish region. The luminescence studies also give rise to understand the effect of high energy γ- ray irradiation effect on RE doped glass which may find applications in discovering radiation hard glass materials and glasses with enhanced radiative characteristics of high-power lasers. In addition, the luminescence studies permit us to study the energy transfer between co-doped RE glass.

At the same time, the luminescence studies help in identifying the energy transfer between two laser dyes: RhB and Rh6G in a silica glass matrix, which may find application in lasers for midwife toning ranges of wavelength.

Future Prospects

Based on the work carried out in the thesis and the results obtained, suggestions for further work are given as follows:

The decrease in hydroxyl content was the primary cause of the increased luminescence observed upon annealing. Annealing's structural modifications might have a big impact on luminescence as well. More thorough research on the structural evolution during annealing could provide more light on how it affects the RE-doped glasses' optical characteristics.

In this work, we performed the high energy gamma irradiation on RE doped silicon dioxide (SiO_2) glass itself. In the future prospects, this high energy effect on the structural and optical properties of RE doped with different hosts in SiO_2 doped glass would be interesting to synthesize.

Different RE ions have the distinctive color emissions. Sm^{3+} emits blue light, Eu^{3+} produces red light, $Pr^{3+}$and Tb^{3+} emit green light. It has been demonstrated that multiple RE doping in other glass hosts can result in the emission of white light through red, green, and blue luminescence. Making multi-RE doped sol-gel glasses that can emit white light when excited by UV or NIR light through up conversion would be an interesting task.

Energy transfer between laser dyes RhB and Rh6G showed that it is ideal for manufacturing lasers for midwife toning range of wavelength in silica glass. It would be interesting to synthesize with nanoparticle host which may give better insight on the improvement of optical properties.

BIODATA

Name	**:**	LALRUATPUIA
Father's name	**:**	LALRAMCHHANA
Date of birth	**:**	16th March 1993
Address	**:**	Ramhlun Veng, Buarpui
		Lunglei District, Mizoram

Educational qualifications:

HSLC	2008	MBSE
HSSLC	2010	MBSE
B. Sc (Physics)	2015	MZU
M.Sc (Physics)	2017	MZU

Research experience:

Registered Ph.D. researcher in Dept. of Physics. Mizoram University under the supervision of Prof. S. Rai since 2019.

List of Paper Publications/Accepted/Communications

1. Lalruat Puia, Uzair Khan, KMS Dawngliana (2022) Synthesis and Spectral Characteristics of RhB and Rh6G Dyes and their Mixture in Solid Matrix. *Indian Journal of Pure and Applied Physics* **60**: 883-891. doi: 10.56042/ijpap. v60i10.62440

2. Lalruat Puia, KMS Dawngliana, A.L. Fanai, S. Rai (2023) Effect of ZnS nanoparticles in photoluminescence properties of Tb^{3+} ion doped silica glass for photonic applications. *Applied Physics A* **129**: 751. doi: https://doi.org/10.1007/s00339-023-07037-7

3. Lalruat Puia, S. Rai (2024) Structural and Spectroscopic Studies of Sm^{3+} Ions Doped ZnS Nanoparticle in Silica Glass Matrix. *Indian Journal of Science and Technology* **17(9)**: 773-779. doi: https://doi.org/10.17485/IJST/v17i9.2939

4. Lalruat Puia, KMS Dawngliana, S. Rai (2024) Spectroscopic investigation of Pr^{3+} doped ZnS nanoparticle in silica glass matrix prepared by sol-gel method. *Applied Physics A* **130**: 812. doi: https://doi.org/10.1007/s00339-024-07963-0

5. KMS Dawngliana, Lalruat Puia, A.L. Fanai, S. Rai (2022) Optical basicity and electronic polarizability of Sm^{3+}-doped silica glass prepared by sol–gel process. *Materials Today: Proceedings* **65(5)**: 2572-2577. doi: https://doi.org/10.1016/j.matpr.2022.04.784

6. KMS Dawngliana, Lalruat Puia, Lalrempuia Ralte, S. Rai (2024) Effect of ZnS nanoparticles on the optical properties of Sm^{3+} ions in silicate matrix. *Journal of Non-Crystalline Solids* **632**: 122871. doi: https://doi.org/10.1016/j.jnoncrysol.2024.122871

7. KMS Dawngliana, Lalruat Puia, A.L. Fanai, S. Rai (2024) Effect of Al on photoluminescence properties of Nd^{3+} in silicate glass-ceramic prepared by in-situ sol-gel method. *Journal of Sol-Gel Science and Technology* **112**:444-455. doi: https://doi.org/10.1007/s10971-024-06539-x

8. KMS Dawngliana, Lalruat Puia, A.L. Fanai, S. Rai (2024) Spectroscopic properties of Pr^{3+}- doped Titania-Silicate glass ceramic for photonic applications. *Optical Materials* **155**:115841. doi: https://doi.org/10.1016/j.optmat.2024.115841

List of Papers Presented in Conferences/ Seminars attended

1. Participated in a two-day International Webinar on Recent Advances in Sciences: Mankind and Change, 6^{th} -7^{th} July, 2020 organized by Govt. Serchhip College, Mizoram.

2. Spectroscopic Studies of RhB Dye in Silica Matrix, XII Biennial National Conference of Physics Academy of North East (PANE 2021), 15^{th} – 17^{th} December, 2021 organized by Deparment of Physics, Tripura University.

3. Study of Optical Properties of Different Concentrations of Rhodamine 6G dye in Silica Matrix, International Conference on Current Trends in Advanced Materials and their Applications for Societal Development (ICTAMASD-2022), 8^{th} – 10^{th} February, 2022 organized by Department of Physics, Dr. Harisingh Gour Vishwavidyalaya Sagar [MP].

4. Energy Transfer Studies of Rhodamine Laser Dyes in Solid Matrix, Mizoram Science Congress (A National Conference), 24^{th} -25^{th} November, 2022 organized by Mizoram Science, Technology, and Innovation Council (MISTIC) in collaboration with Mizo Academy of Sciences (MAS), Mizoram Science Society (MSS), Science Teachers' Association, Mizoram (STAM), Geological Society of Mizoram (GSM), Mizoram Mathematics Society (MMS), Biodiversity and Nature Conservation Network (BIOCONE) and Mizoram Information & Technology Society (MITS).

5. Participated in Two-Day International Symposium on the History of Astronomy of the Mizo People, 18^{th} -19^{th} May, 2023 organized by Department of Physics, Mizoram University and Mizoram Science Centre.

6. Structural and Spectroscopic studies of Eu^{3+} ions doped ZnS nanoparticles in silica glass, International Conference on Recent Advances in Energy Materials and its Applications (ICRAEMA- 23), 30^{th} – 31^{st} May, 2023 organized by Department of Physics, Pachhunga University College, Mizoram University.

7. Luminescent Properties of Pr^{3+} ions Doped ZnS Nanoparticle in Silica Glass Matrix Prepared by Sol-Gel Method, International Conference on Recent Advances in Mathematical, Physical and Chemical Sciences (ICRAMPC-24), 21^{st} – 23^{rd} February, 2024 organized by School of Physical Sciences, Mizoram University.

PARTICULARS OF THE CANDIDATE

Name of candidate	: LALRUATPUIA
Degree	: Doctor of Philosophy (Ph.D.)
Department	: Physics
Title of the Thesis	: Structural and Optical Studies of Some Rare Earth Ions (Eu^{3+}, Tb^{3+}, Sm^{3+}, Pr^{3+}) Doped Nanoparticles for Device Applications
Date of admission	: 23rd July 2019
Approval of Research Proposal	
1. DRC	: 27th May 2020
2. BOS	: 5th June 2020
3. School Board	: 12th June 2020
MZU Registration No.	: 2080 of 2012
Ph.D Registration No. & Date	: MZU/Ph.D./1374 of 23.07.2019
Extension if any	: NIL

(Prof. ZAITHANZAUVA PACHUAU)
Head of Department
Department of Physics
Mizoram University

ABSTRACT

STRUCTURAL AND OPTICAL STUDIES OF SOME RARE EARTH IONS (Eu^{3+}, Tb^{3+}, Sm^{3+}, Pr^{3+}) DOPED NANOPARTICLES FOR DEVICE APPLICATIONS

AN ABSTRACT SUBMITTED IN PARTIAL FULFILLMENT OF THE REQUIREMENTS FOR THEDEGREE OF DOCTOR OF PHILOSOPHY

LALRUATPUIA

MZU REGISTRATION NO. : 2080 of 2012

Ph.D. REGISTRATION NO. : MZU/Ph.D./ 1374 of 23.07.2019

DEPARTMENT OF PHYSICS

SCHOOL OF PHYSICAL SCIENCES

JULY, 2024

Thesis title: Structural and Optical Studies of Some Rare Earth Ions (Eu^{3+}, Tb^{3+}, Sm^{3+}, Pr^{3+}) doped Nanoparticles for Device Applications.

Objectives:

- The synthesis of some rare-earth (Eu^{3+}, Tb^{3+}, Sm^{3+}, Pr^{3+}) co-doped with nanoparticles in silica glass.
- Study of structural and optical properties of prepared samples for photonic applications.
- Study of effect on Optical properties of Laser Dye doped with nanoparticles.

Introduction

Rare earth (RE) elements are a set of seventeen chemical elements. They include the fifteen lanthanides plus scandium and yttrium. Lanthanides comprise of the series of the element from Lanthanum (Z=57) to Lutetium (Z=71). All lanthanide elements form trivalent cation (+3), whose chemistry is largely determined by the ionic radius, which decreases steadily across a period i.e., from lanthanum to lutetium, a phenomenon known as Lanthanide Contraction. Lanthanide ions have important characteristics that distinguish them from other optically active ions. Their emission and absorption ranges are narrow and the transitions (emission and absorption) are relatively insensitive to host materials. The lifetimes of their metastable states are long and quantum efficiency tends to be high. Due to these properties, rare earth doped glasses have found many optical applications such as glass fiber laser, optical amplifier, solid state display devices, sensors etc. Recent studies (Hayakawa *et al.*, 2000) have shown that co-doping with certain nanoparticles can enhance the luminescence properties of RE ions and how varying the concentrations can have effects on the spectra. Therefore, the RE ions Tb^{3+}, Eu^{3+}, Sm^{3+} and Pr^{3+} ions were singly doped with ZnS nanoparticle to study their structural and spectroscopic properties for photonic applications. In addition to, the effect of high energy γ-irradiation effect on the structural and optical properties of Sm^{3+} doped glass was studied in detail. We know that the energy transfer between RE ions improves the emission intensity, lifetimes, quantum efficiencies. Energy transfer

process has gained much technological importance in the fields of optoelectronics and photonics owing to its technological application point of view. On account of that, the energy transfer between Tb^{3+} and Eu^{3+} ions and energy transfer study between laser dyes Rh6G and RhB were also included in the present study.

Experimental Methods

Synthesis

The sol-gel process has been utilized successfully for synthesizing the RE ions doped with ZnS nanoparticle in silicate glass. The sol-gel process for the preparation of samples relies on the hydrolysis and condensation of tetraorthosilicate (TEOS) in the presence of H_2O to form the SiO_2 network. For the preparation of sample, required amounts of dopants were first dissolved in methanol, distilled water and HNO_3 using magnetic stirrer. TEOS was then added and stirred for 2 hrs. For the preparation of ZnS nanoparticle, ZnS powder was first dissolved in ethanol, distilled water and HNO_3 and stirred for 2 hrs. The sol formed were then poured in a sealed plastic containers and left for few days to form stiff gel. Then, a few pinholes are made on the seals to allow slow evaporation of water and methanol. After adequate drying at room temperature, each batch was transferred to muffle furnace and heated slowly up to 1000^0C and maintained for one hour.

Characterization of Sample

The glass sample under study was coated with 1-bromonaphthalene ($C_{10}H_7Br$) as an adhesive coating and its refractive index was determined using an Abbe refractometer. Using xylene (C_8H_{10}) as an immersion liquid, the density of the solid glass sample under study was calculated using the Archimedes principle. FTIR spectra were recorded by IRAffinity-1S (SHI-MADZU). The crystal structure was analysed using X-ray Diffractometer (XRD) equipped with a Cu-Kα radiation source. Additionally, using high-resolution transmission electron microscopy (HR-TEM) with a 300 kV acceleration voltage, the particulate nanostructure patterns of the nano-composites were investigated. Diffuse reflectance spectra were created with a UV- Visible Spectrophotometer (Model: Evolution 220, Thermo Scientific, USA).

The absorption and PL spectra were recorded using iHR320 imaging spectrometer from Horiba Scientific, in conjunction with the Syner JYTM software. The excitation spectra were recorded by F-4700 Fluorescence Spectrometer.

Results

The Tb^{3+} ions doped with ZnS nanoparticles and ZnS doped silica glass-ceramic were synthesized by sol-gel method. The density and refractive index increase with increase in host concentration. XRD and selected area electron diffraction (SAED) studies confirm the formation of hexagonal polycrystalline structure. TEM analyses revealed that variation in size of the particles lies between 10 to 50 nm. FTIR spectra show the removal of OH group with annealing. The band gap energy of the as-synthesized nanocomposite glass was 3.18 eV with a green light emission. The PL emission intensity increased with the concentrations of ZnS. The CIE chromaticity revealed that the tunability of color changes from blue-green to yellowish green region as ZnS concentration increases.

The density of the glass samples increases with as ZnS NPs is added in the silica glass because of the substitution of higher molecular weight of ZnS (Mw. = 97.07 g/mol) into SiO_2 (Mw. = 60.08 g/mol) is founded for ZnS nanoparticle doped with Eu^{3+} ions. The formation of the blende structure and a hexagonal polycrystalline phase of ZnS is confirmed by studies using SAED and XRD. Analysis using TEM showed that the particles' sizes vary from 10 to 50 nm. The structural properties of prepared glass samples were examined using FTIR at various annealing temperatures. As-synthesised doped ZnS glass-ceramic's band gap energy was 3.49 eV, while the bulk value was 3.60 eV with a pure green emission which may be due to inverse doping effect. The examined glass can produce white light for use in commercial lighting, according to the CIE color chromaticity and CCT measurements.

After annealing at 300 °C for the Sm^{3+} doped ZnS sol-gel silica glass matrix, the XRD investigations verified the formation of a glassy amorphous nature and the TEM studies verified that the investigated nanoparticles are polycrystalline in nature

with a particle size ranging between 10-50 nm. The PL spectra show three emission bands at 565 nm, 603 nm and 650 nm corresponding to $^4G_{5/2} \rightarrow {}^6H_{5/2}$, $^4G_{5/2} \rightarrow {}^6H_{7/2}$ and $^4G_{5/2} \rightarrow {}^6H_{9/2}$ transitions respectively with the most noticeable bands are in the orange-red region. Thus, when activated with an UV light source at 370 nm, the doped glass can be used to produce almost pure white hue.

The reduced value of the molar volume for lower concentration of Pr^{3+} ions for doped with ZnS NP's which can be explained by an increase in the force constant and a shorter bond length of the bonds inside the network is shown for different concentration of Pr^{3+} ions doped with a fixed amount of ZNS NPs in silica glass matrix. The glassy amorphous nature was verified by XRD spectra. After annealing at 300 °C, TEM spectra showed that the particle size ranges from 10 to 50 nm and SAED images verified that the glass under study is polycrystalline. The Judd-Ofelt parameters followed the trend $\Omega_6 > \Omega_4 > \Omega_2$. The stimulated emission properties for laser active medium which are determined by the spectroscopic quality factor Ω_4/Ω_6 was calculated as 0.45, which is lowest as compared to other doped glass. The values of the Figure of Merit (FOM) suggest that it could be utilized as an optical amplifier device. Strong stark splitting of $^3H_4$ levels was observed in the VIS-NIR region during photoluminescence emission. This glass can emit green light and be useful for laser applications in the visible spectrum.

In order to understand the effect of gamma irradiation on the composition and optical properties of the glass, Sm^{3+} doped SiO_2 glass were irradiated with ^{60}Co isotope radiation source. When the sample is kept in a dark room at room temperature, PL spectra show that the valency of Sm^{3+} was reduced to Sm^{2+} due to the transfer of energy takes place from Sm^{3+} to Sm^{2+} by cross relaxation between $^4G_{5/2} \rightarrow {}^6H_{5/2}$ and $^5D_0 \rightarrow {}^7F_0$, that Sm^{3+} character was regained after 148 hours (1 week) of irradiation and that Sm^{2+} existence was highest after 72 hours of gamma irradiation. FTIR spectra show that the composition of the glass matrix did not significantly change after gamma irradiation.

A number of singly doped ZnS:Eu, ZnS:Tb, and co-doped ZnS:Tb:Eu have been synthesized to study energy transfer between Tb^{3+} and Eu^{3+} ions in detailed.

Change in concentration does not have significant effect on IR spectra and removal of hydroxyl group with annealing was confirmed by IR spectra. Because of the distinctive 4f-4f transitions of the Tb^{3+} and Eu^{3+} ions the single doped ZnS:Eu and ZnS:Tb emit red and green light, respectively. The color tunability falls within blueish to purplish region for ZnS:Tb:Eu doped glass. Strong overlap between the Eu^{3+} excitation and Tb^{3+} emission peaks under excited with Eu^{3+} emission wavelengths indicates that there may have been a transfer of energy from Tb^{3+} to Eu^{3+} in ZnS doped silicate glass. The average lifetime (τ) for ZnS:Tb was equal to 1.39 ms and ZnS:Tb:Eu to 0.21 ms, this reduce values of τ clearly manifest the transfer of energy from Tb^{3+} to Eu^{3+} ions. The transfer efficiency is calculated as 84.9%. Dipole-dipole interaction can be asserted as the dominant mechanism for the energy transfer from Tb^{3+} to Eu^{3+} ions, as anticipated by two distinct energy transfer formula: (i) Dexter's energy transfer formula combined with the Reisfeld's approximation (ii) Van Uitert's.

Similarly, the energy transfer between laser dyes Rh6G and RhB were also studied in detailed. The absorption and emission intensity for Rh6G in liquid and solid phase were compared. The absorption spectra for Rh6G increase with increase in concentration for solid and liquid phase while emission spectra first increase and then decreases with further increasing the concentration. The FWHM falls with increasing concentrations for solid sample while for liquid sample FWHM increases with increasing concentration, therefore red shift occurred. It is observed that there is a significant increase in the PL intensities of RhB due to addition of Rh6G. These reveals that there is an efficient energy transfer from Rh6G to RhB. FWHM also increases as the Rh6G concentration rises up to 1.5% which suggesting that the tunability increases with energy transfer.

Conclusion

With the help of sol-gel technique, we have successfully synthesized four RE ions singly doped and co-doped with ZnS NPs, gamma irradiation effects and Laser dyes that may be employed in a variety of future photonic applications. Further synthesized of their physical, structural and optical properties with different host are necessary to improve the luminescent efficiency and overall performance.